

RESISTIVITY AND AC SUSCEPTIBILITY OF  
CURRENT-CARRYING WHISKERS

by

Lee, Jae-Gwang

B.A., Yonsei University, Seoul, 1981

M.S., Simon Fraser University, 1988

THESIS SUBMITTED IN PARTIAL FULFILLMENT OF  
THE REQUIREMENTS FOR THE DEGREE OF  
DOCTOR OF PHILOSOPHY

in the Department  
of  
Physics

© Jae-Gwang Lee

SIMON FRASER UNIVERSITY

June 1994

All rights reserved. This work may not be  
reproduced in whole or in part, by photocopy  
or other means, without permission of the author.

# Approval

Name: Jae-Gwang Lee

Degree: Ph.D.

Title of thesis: Resistivity and AC susceptibility of current-carrying whiskers.

Examining Committee:

Chair: Dr. J.R. Dahn

---

Dr. A.S. Arrott  
Senior Supervisor

---

Dr. B. Heinrich

---

Dr. V.F. Cochran

---

Dr. S. Gygax  
University Examiner

---

Dr. Dan S. Bloomberg  
External Examiner  
Xerox Palo Alto Research Center

Date approved:

PARTIAL COPYRIGHT LICENSE

I hereby grant to Simon Fraser University the right to lend my thesis, project or extended essay (the title of which is shown below) to users of the Simon Fraser University Library, and to make partial or single copies only for such users or in response to a request from the library of any other university, or other educational institution, on its own behalf or for one of its users. I further agree that permission for multiple copying of this work for scholarly purposes may be granted by me or the Dean of Graduate Studies. It is understood that copying or publication of this work for financial gain shall not be allowed without my written permission.

Title of Thesis/Project/Extended Essay

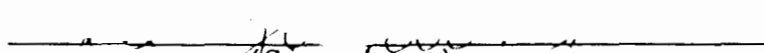
---

Resistivity and AC Susceptibility of Current Carrying Whiskers

---

---

Author:

  
(Signature)

Jae-Gwang Lee

---

(Name)

29, July, 1994

---

(Date)

# Abstract

The effects of currents and/or external fields on  $\langle 100 \rangle$  iron whiskers are investigated experimentally and theoretically. Electrical dc resistance and ac susceptibility measurements are used to understand the magnetic configurations corresponding to external fields and/or currents. When a sufficient current is applied along the principal axis of the whisker without external field, experimental results at room temperature show that the resistance is decreased about 0.17% and that ac susceptibility signals disappear. These results are explained if the configuration has four transversely magnetized domains inside of which the magnetization is along an easy axis, while at the corners and at the center it is directed along the principal axis of the whisker. This is called the collapsed configuration. It has a finite central core which is too small to affect the magnetoresistance or the ac susceptibility. When an external field is increased in the presence of the applied current, a sequence of domain structures can be deduced from the susceptibility results. A central domain grows easily from the central core when a small external field is applied along the direction of the magnetization. On the other hand, if the direction of the field is opposite to the magnetization of the core nothing happens until a larger external field nucleates a new central domain.

A model is suggested to explain the experimental results by considering the competition among exchange, anisotropy, and demagnetizing energies, and energies from currents and fields. Most of the susceptibility results are explicable on this model. The behavior for low fields is harder to understand based on estimates of the wall energy.

The sign of the derivative of wall energy with respect to core size is important. To obtain a better theoretical value for the wall energy, a micromagnetic calculation is carried out using a vector potential to generate magnetization patterns. The sign is negative as expected from simpler arguments, but this does not explain the low field behavior. An explanation of the low field behavior could be obtained if there is a residual demagnetizing field from some source other than the residual magnetization of the central cross section. This indicates the need for a full three dimensional calculation, but that is beyond the scope of this thesis.

## Acknowledgments

I would like to thank my supervisor, Professor A.S. Arrott for his assistance and patience with this work. I would also like to appreciate Drs. Bret Heinrich, John Cochran, S. Gygax, and the external examiner, Dan S. Bloomberg for their valuable discussions and helpful suggestions.

Thanks also to Dr. Terry Templeton and Victor Finberg for editing this manuscript and also to M. Kowaleski, D. Atlan, Z. Celinski, and Y. Yoshida for their assistance. I acknowledge the financial support of the department and the university as teaching assistantships and a scholarship.

Finally, I would like to thank my parent and wife for their help and patience.

# Table of Contents

Approval.....	ii
Abstract .....	iii
Acknowledgments.....	v
Table of Contents .....	vi
List of Tables .....	ix
List of Figures.....	ix
List of Symbols .....	xi
1. Introduction.....	1
1.1 Structure of the Thesis .....	9
2. Reviews of Micromagnetism, AC Susceptibility, and Magnetoresistance.....	11
2.1. Micromagnetism.....	11
2.1.1. Exchange Energy .....	12
2.1.2. Magnetostatic Self-Energy.....	13
2.1.3. Magnetocrystalline Anisotropy Energy .....	14
2.1.4. External Field Energy.....	14
2.2. Characteristic AC Responses for a <100> Whisker.....	15
2.3. Interpretation of the AC Susceptibility Measurement .....	23
2.4. Magnetoresistance of an Iron Whisker .....	28
2.5. Magnetic Field from the Applied Current .....	32
3. Experimental Methods.....	37
3.1. Growth of Iron Whiskers.....	37
3.2. DC Resistance Measurements.....	39
3.3. AC Susceptibility Measurements.....	42
3.4. Combined Susceptibility and Resistance Measurements .....	44

4. Experimental Results and Their Interpretations .....	46
4.1. Results of Resistance Measurements.....	46
4.1.1. Damaged Samples.....	47
4.1.2. <100> Whiskers with Landau Structures.....	50
4.2. Results of AC Susceptibility Measurements .....	52
4.2.1. Critical Current Measurements.....	53
4.2.2. Effect of Currents on AC Susceptibility.....	55
4.3. Models for the Stable Structures.....	63
4.3.1. Model for a Fixed Structure .....	63
4.3.2. Model for a Variable Structure .....	65
4.4. Model for the AC Susceptibility .....	75
4.4.1. AC Susceptibility with zero frequency.....	76
4.4.2. In-Phase and Out-of-Phase Components of AC Susceptibilities.....	82
4.5. Domain Structures deduced from AC Susceptibility and Resistance Measurements.....	89
4.5.1. Structures deduced from AC Susceptibility.....	89
4.5.2. Discussions of the Resistance Measurements.....	94
4.5.3. Conclusions .....	96
5. Micromagnetic Calculations using Vector Potentials with Ritz Parameters .....	98
5.1. Vector Potential for a Domain Structure.....	99
5.2. Modification of the Vector Potential.....	106
5.3. Magnetization Processes .....	118
6. Conclusion .....	124
Appendix: Grid System.....	126
References.....	134



## List of Tables

Table 1. Energy densities of 90° and 180° walls with different planes.....	6
Table 2. Magnetoresistance coefficients for iron and nickel.....	32
Table 3. Parameters used in the calculations for a <100> iron whisker at room temperature.....	105

## List of Figures

Figure 1. Landau domain structure .....	1
Figure 2. Possible domain structures .....	3
Figure 3. Induced signal versus current.....	4
Figure 4. Coleman domain structure .....	16
Figure 5. Experimental set-up for the ac susceptibility measurement .....	17
Figure 6. Characteristic magnetic out-of-phase and in-phase responses for a $\langle 100 \rangle$ whisker .....	18
Figure 7. Landau and diamond domain structures.....	22
Figure 8. Magnetoresistance of a $\langle 100 \rangle$ whisker versus field.....	29
Figure 9. Schematic diagram for calculation of the magnetic field from a current.....	33
Figure 10. Magnetic field distribution in a current carrying whisker.....	35
Figure 11. Contour plots for the magnetic field of Fig. 10 .....	36
Figure 12. Diagram for resistance measurements.....	40
Figure 13. Diagram for ac susceptibility measurements .....	42
Figure 14. Magnetoresistance of a damaged $\langle 100 \rangle$ whisker .....	48
Figures 15(a) and (b). Magnetoresistance for a $\langle 100 \rangle$ whisker .....	50, 52
Figures 16(a) and (b). Magnetic response versus current with no field.....	54, 55
Figure 17. AC susceptibility measurements at several currents .....	56
Figure 18. Damaged sample ac susceptibility.....	58
Figure 19. Schematic for out-of-phase signal versus field.....	60
Figures 20(a) and (b). Out-of-phase and in-phase signals of two whiskers with different currents .....	62
Figures 21(a) and (b). Diagrams for the energy calculation.....	67

Figure 22. Magnetization versus external field for three currents.....	72
Figure 23. Comparison between the experimental results and the calculated ones.....	74
Figure 24. DC susceptibility versus external field for two currents.....	75
Figure 25. Schematic diagram for an eddy current calculation.....	77
Figures 26(a) and (b). Calculated in-phase response and magnetization with a large residual magnetization and with different signs of wall energy .....	80, 81
Figures 27(a) and (b). Calculated out-of-phase and in-phase responses.....	88
Figure 28. Deduced domain structures.....	90
Figure 29. Diagram for curved domains .....	91
Figure 30. Diagram for model calculations .....	103
Figure 31. Magnetization at the cross section .....	103
Figure 32. Result of minimizing the total energy .....	106
Figure 33. Behavior of the <i>coth</i> -function .....	107
Figures 34(a), (b), (c), and (d). Contour plots for magnetization .....	110-114
Figures 35(a) and (b). Diagram for a new grid system .....	115
Figures 36(a) and (b). Results of the minimization with different currents.....	116
Figure 37. External field and the size of the central domain.....	120
Figure 38. Contour plot for calculated magnetization.....	122

## List of Symbols

$A_{ex} (= \frac{C}{2})$	exchange constant
$A(a_w) \frac{q}{d} M_s, s \frac{q}{d} M_s$	average magnetization from domain walls
$A_p, A_s$	cross sectional areas for pick-up coil and whisker
$a_0$	length of the edge of the unit cell
$2a_w$	wall thickness of a 90° wall lying in a (110) plane
$a, h, k$	Ritz parameters
$\vec{A}(\vec{r})$	vector magnetic potential
$A_y, A_\phi$	components of vector potential
$c$	speed of light
$\lambda (= 4\pi D), D$	demagnetizing factor
$E_{tot}, E_{ex}, E_D, E_K, E_H, E_w, E_I$	total, exchange, demagnetizing, anisotropy, external field, and wall energies and energy from current
$\bar{E}_{tot}, \bar{E}_{ex}, \bar{E}_D, \bar{E}_K, \bar{E}_H, \bar{E}_w, \bar{E}_I$	energy densities (per unit length)
$\bar{H}_w, \bar{H}_D, \bar{H}_K, \bar{H}_o$	wall, demagnetizing, anisotropy, and external fields
$\bar{H}_{eff}, H'_{eff}$	total and dc effective fields
$H_d, H_c, H_r, H_n$	departure, collapse, renucleation, and nucleation fields
$H_I, H_{I,x}, H_{I,y}$	total, and x- and y-components of the magnetic fields from a current
$h_o, h_e, h_D$	amplitudes of ac external, ac eddy current, and ac demagnetizing fields
$h'_o, h_i$	ac effective and ac internal fields.
$I$	current

$I_c$	critical current
$J$	current density
$J_{ex}$	exchange constant for nearest neighbors
$J_{i,j}$	exchange constant for near neighbors
$K_1, K_2$	anisotropy constants
$\bar{M}, M_s$	magnetization and saturation magnetization
$M_x, M_y, M_z$	x-, y-, and z-components of magnetization
$M_1, M_2, M_3$	averaged magnetization for specific areas
$m_0 M_s, C(a_w) M_s$	residual magnetization
$m(= \langle m \rangle)$	averaged change in the magnetization by vibrating domain walls
$\langle M \rangle$	averaged magnetization
$M_{y,s}(x), M_{y,c}, M_{y,c}(x)$	average y-components of magnetization
$M_{y,c_0}$	time-independent y-component of magnetization
$N$	total number of atoms in the material
$n$	number of nearest neighbor atoms
$\hat{n}$	unit vector normal to the surface
$\hat{n}_c$	unit vector for a direction of current
$\hat{n}_M$	unit vector for a direction of magnetization
$2q, 2d$	widths of the saturated domain and the whisker
$\Delta R (\approx -\Delta R'), \Delta R_{max}$	changes in resistances
$R_{p.s.s}, R_{rot.[100]}, R_{sat.[100]}$	resistances for different domain configurations
$R'$	resistance of a whisker
$r_o, R$	radius to an inner domain and for a cylindrical whisker
$r_1$	amplitude of the vibrating wall

$S_s$	Spin angular momentum
$d\tau, dS$	volume and surface elements
$V$	volume of a magnetic material
$w(= \frac{2d}{L})$	ratio of the width to the length of a whisker
$W_{ij}$	exchange energy between spins
$x(= \frac{r}{R}, \text{ or } \frac{2q}{2d})$	wall parameter
$\hat{x}, \hat{y}, \hat{z}, \hat{\phi}$	unit vectors
$\alpha_m, \beta_m, \gamma_m$	direction cosines of magnetization with respect to cubic axes
$\alpha_c, \beta_c, \gamma_c$	direction cosines of current with respect to cubic axes
$\rho_m, \sigma_m$	volume and surface magnetic charge densities
$\alpha(\omega), \alpha(0), \beta(\omega), \beta(0)$	magnetic stiffness and viscosity
$\alpha_i(\omega), \beta_i(\omega)$	intrinsic magnetic stiffness and viscosity
$\beta_{II}$	constant depending on the dimension of a whisker
$\rho_o, \rho_{sat.}$	resistivity of an iron whisker with a demagnetized domain structure and with the saturated domain
$\Delta\rho(\approx -\Delta\rho')$	change in resistivity
$\Delta\rho_{rot.[100]}, \Delta\rho_{sat.[100]}$	resistivity changes for a rotated state and a saturated state
$\Delta\rho_{100}, \Delta\rho_{111}$	magnetoresistance constants for a cubic crystal
$\Delta\rho_{max}$	maximum resistivity change due to the magnetoresistance effect
$\sigma_a$	90° wall energy density with a (110) plane
$ \sigma_o  (= \frac{ \sigma_i }{4\sqrt{\pi}})$	wall energy coefficients
$\sigma_c$	electric conductivity

$\phi_{ij}$	angle between two near neighbor spins
$\phi, \phi_d, \phi_q$	magnetic fluxes in a pick-up coil, in the central cross section, and for a saturated whisker, respectively
$\phi_M$	magnetic flux for a cylindrical whisker
$\omega$	driving field frequency
$\chi_o$	zero-frequency susceptibility
$\chi_i, \chi_{ex}, \chi', \chi''$	intrinsic, effective (measured), in-phase, and out-of-phase susceptibilities

# Chapter 1

## Introduction

It is known that a well-grown  $\langle 100 \rangle$  iron whisker bounded by  $\{100\}$  faces generally exhibits the simple Landau domain structure in the absence of an applied field.<sup>1,2</sup> A typical  $\langle 100 \rangle$  whisker has a square cross section of width  $20 \mu\text{m}$  to  $1000 \mu\text{m}$  and a length of  $3 \text{ mm}$  to  $4 \text{ cm}$ . The Landau structure has two long and two short domains as shown in Fig. 1. The closure domains at the ends of the whisker are necessary to avoid a large magnetostatic energy due to free poles.

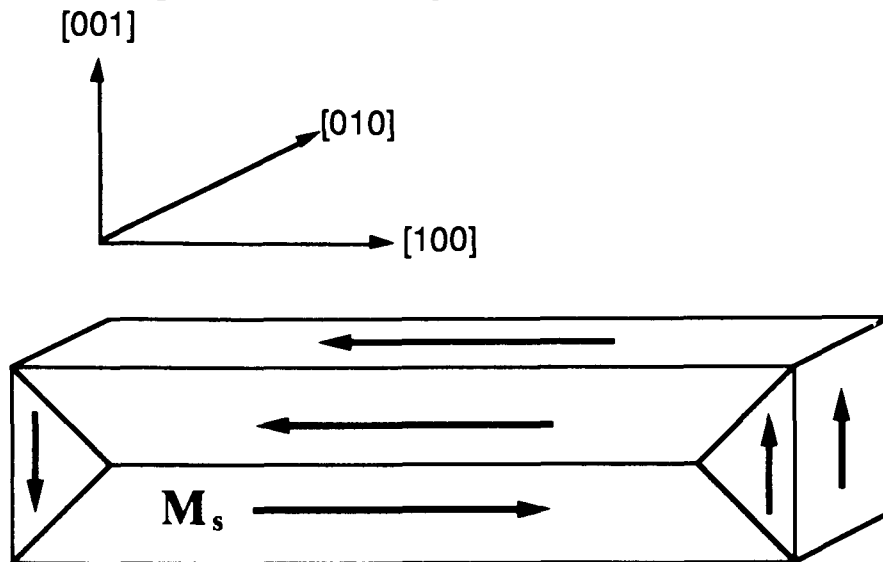


Fig. 1. Landau domain structure in a  $\langle 100 \rangle$  whisker with no external field. The sides of the whisker are all  $\{100\}$  planes. The closure domains are at the ends of the whisker.

When current flows through a  $\langle 100 \rangle$  iron whisker, it produces a magnetic field that acts on the magnetic moments. If the field is



sufficiently strong, one stable domain structure can be transformed to another. Shumate, Coleman, and Fivaz<sup>3</sup> observed changes in domain structures with the Bitter powder method while passing current through a  $\langle 100 \rangle$  whisker. One possible domain configuration of a  $\langle 100 \rangle$  iron whisker in the presence of a strong current was suggested by Shumate *et al.* as shown in Fig. 2(a). This was based on the absence of domain walls at the surface of the whisker while a current of approximately 1~2 Amp was applied.

More recently, Berthe, Birkner, and Hartmann<sup>4</sup> observed domain structure changes using an electron microscope with type II magnetic contrast while varying the current that passed through a  $\langle 100 \rangle$  iron whisker. They observed the movements of domain walls when the applied current was larger than 16 mA. They also performed an inductive measurement on another whisker to follow the effect of the applied current. When a slowly varying current passed through the whisker, a coil wrapped tightly around the whisker could pick up information on changes in magnetization. Two major jumps in the induced signals were observed for each direction of changing current. The results, in the absence of an external magnetic field, are shown in Fig. 3. The major jumps correspond to transformations of one stable domain structure to a different one and back again. Their inductive measurement and observation technique made it clear that the domain walls moved as the applied current was varied. However, their experiments did not give them enough information to identify the domain configuration inside the whisker when a low current was passed along the whisker. Nevertheless, they concluded that a sufficiently large current transformed the Landau domain structure

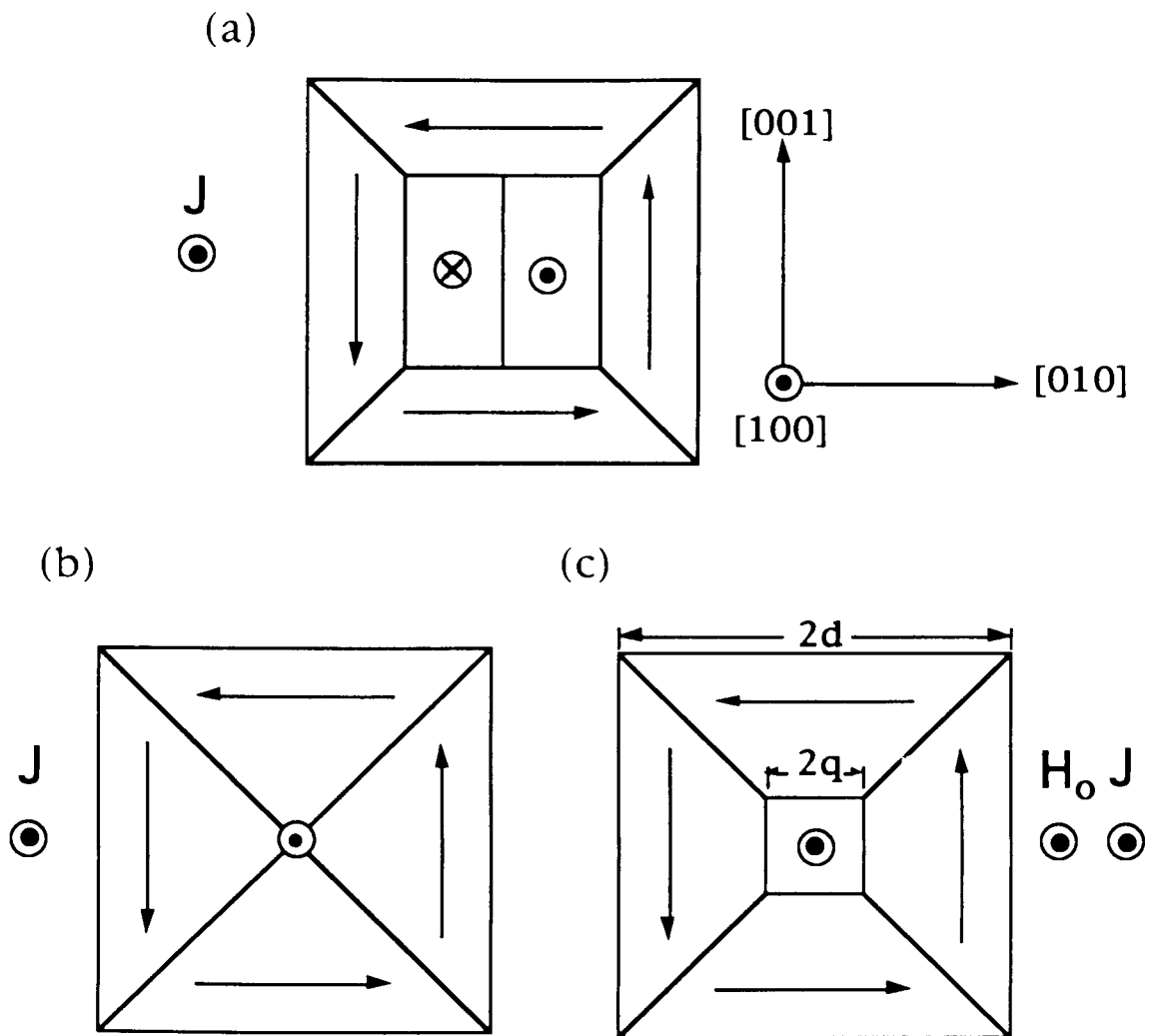


Fig. 2. Domain structures in the cross section of a  $\langle 100 \rangle$  iron whisker while applying a larger than critical current

(a) suggested by Shumate *et al.*,

(b) possible structure without external field;

(c) possible structure with external field.

into the one suggested by Shumate *et al.*<sup>3</sup>

The structure suggested by Shumate *et al.* was designed to accommodate both the field from the current and the need to decrease the demagnetizing energy. In the outer region, the magnetization

would lie in the plane of the cross section more or less in the direction of the field from the current at each point except in the regions of  $90^\circ$  walls lying in  $\{110\}$  planes. In the inner region, a Landau type structure having a  $180^\circ$  wall lying in a  $(100)$  plane would satisfy the condition that the demagnetizing field be minimized. In this model, the size of the inner region is determined by the strength of the current and the position of the  $180^\circ$  wall responds to external fields applied along the axis. In zero field, the wall divides the inner region into equal areas. This model cannot be tested by observations of the surface magnetization,<sup>4,5</sup> but resistivity can be used to probe the relative areas of the inner and outer regions.

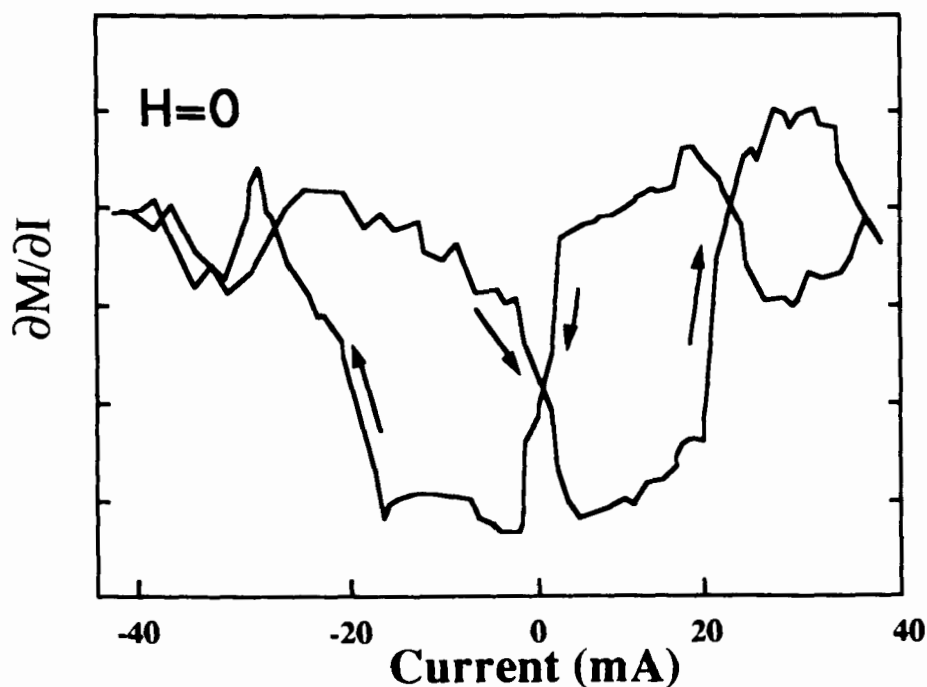


Fig. 3. Induced signal  $V \sim \partial M / \partial I$  as a function of current as observed by Berthe *et al.*<sup>4</sup> There was no external field. (No scale was given for the ordinate.)

From the magnetoresistance effect,<sup>6,7</sup> the resistivity is slightly smaller when the magnetization is perpendicular to a current along the principal axis compared to when both are along the principal axis. For small external fields the magnetic response was presumed to be by motion of the 180° wall and therefore no changes in the resistance were to be expected. For larger external fields the inner region could expand as the external field competed with the field from the current. This would increase the resistance. Our preliminary measurements of the magnetoresistance over a wide range of currents were consistent with this interpretation, but our ac susceptibility measurements were not. On the basis of the Shumate model we would have expected that the ac susceptibility with small external fields would have been large because of the motion of the 180° domain wall. Our measurements did not show any significant ac signal at zero field while current was applied. This led to a reexamination of the assumptions behind the suggestion of Shumate *et al.*

Lilley<sup>8</sup> made numerical calculations of energy densities for various kinds of walls. These are shown in Table 1 and enable us to estimate the total energy of possible domain structures without detailed micromagnetic calculations. The energy density of a 90° domain wall lying in a (110) plane is  $\sqrt{3}$  larger than the one lying in a (100) plane. The energy density of a 180° domain wall is twice as large as that of a 90° domain wall lying in a (100) plane, if one neglects the small effects of magnetostriction. A simple estimate of domain wall energies shows there is less wall energy density for the domain structure shown in Fig. 2(b) than the Shumate domain structure of Fig. 2(a). This makes the validity of the Shumate model doubtful. Shumate *et al.* introduced

Table 1. Energy densities of 90° and 180° walls for iron.

Kind of Wall	Plane of Wall	Wall Energy(erg/cm <sup>2</sup> )
90°	(100)	0.8
90°	(110)	1.3
90°	(111)	0.9
180°	(100)	1.5
180°	(110)	2.3

the 180° wall in the central region in order to reduce the magnetostatic self-energy. But if the central region did not exist, there would be no net magnetization and no magnetostatic self-energy. There would be no need for the 180° wall that increases the wall energy.

The absence of any inner core of magnetization parallel to the principal axis of a whisker in Fig. 2(b) satisfies the condition that the demagnetizing energy be minimized. This raises the question of what happens when a field is applied along the axis in the presence of a current sufficiently large to destroy the Landau structure. Here one can invoke a picture of an outer region that is magnetized in the plane of the cross section by the field from the current and an inner region which is magnetized along the direction of the field, but without the Shumate 180° domain wall. Such a configuration is shown in Fig. 2(c). The size of the inner region is determined by competition between the dc field applied along the whisker and the field from the current, but in doing this the demagnetizing field must be taken into account as well as

the difference in wall energy between the configurations of Figs. 2(b) and (c).

The model for Figs. 2(b) and (c) leads to the prediction that it should make a big difference whether the field is applied in one direction or the other, depending on the previous fields. Where the four walls meet in the center along the whisker, the magnetization points in one direction or the other along the whisker axis. A field applied parallel to the direction of the central intersection should lead to a growth of the inner region as shown in Fig. 2(c). A field in the opposite direction should not. And the structure should remain as Fig. 2(b) until some nucleation process, presumably from some region away from the central cross section, leads to a reversal of the direction of the inner core without affecting the magnetization in the outer region.

To determine the structure corresponding to sufficiently large current, we looked in more detail into the information that can be extracted from the combination of magnetoresistance and ac susceptibility as functions of both external field and current along the axis of the whisker. The resistance is different if the magnetization is parallel or perpendicular to the current.<sup>6,7</sup> The in-phase component of the ac susceptibility signal<sup>9</sup> measures the restoring force from the competing terms in the energy. The out-of-phase component is sensitive to domain wall configurations as they generate eddy currents by their motion.

The effect of currents and magnetic fields should have been seen in the early resistivity measurements to be described here, but was not because of two factors. One was the low precision of these early measurements and the other was a lack of appreciation of the effects of

stress on the magnetic response. Stress arises in the process of attaching leads to the whisker for the resistance measurements. By refinement of techniques it has been possible to show that the behavior produced by applying the principles of micromagnetics to the configuration of Fig. 2(c) is consistent with the later experimental results for the resistivity and the ac susceptibility. In achieving this consistent behavior of these two experiments it was necessary to pay careful attention to the effects of stress coming from the handling of the whiskers.

The perfection of the whisker and the freedom from stress effects could be tested by measuring the field dependence of the ac susceptibility in the absence of current. There is a substantial body of results to be expected in this case from the work of Heinrich and Arrott<sup>9</sup> which is reproduced for the present samples. Maintaining the same field dependence of the ac susceptibility while attaching the leads for the resistivity measurement was not easily achieved. Ideally one should have been able to measure both the resistance and the ac susceptibility at the same time, but geometrical constraints made this too difficult. Yet a series of experimental procedures were adopted that indicate strongly that the same result could be obtained with sequential measurements of the ac susceptibility with the current leads attached and the resistance with both current and potential leads in place.

The principal concerns in this thesis are the preparation and handling of the whiskers for ac susceptibility and dc resistance measurements and the determination of how the results of the measurements depend on both the current and the applied dc field along the principal axis of the  $\langle 100 \rangle$  whisker. The interpretation of the

data relies on Maxwell's equations and the modeling of magnetization configurations which provide detailed insights into the observed behavior.

## 1.1 Structure of the Thesis

In Chapter 2, micromagnetism is reviewed briefly. The four energy terms involved in the total energy are explained. The characteristic magnetic responses for a  $\langle 100 \rangle$  iron whisker are reviewed. The measured signal is explained in terms of eddy currents and the magnetic stiffness arising from demagnetizing effects along the whisker. The change in resistance is explained and the field from a current is derived in that chapter. In Chapter 3, Brenner's crystal growth technique, used to grow the whiskers, is described. The dc resistance and ac susceptibility measurements are described in detail. In Chapter 4, the experimental results are presented. The domain structures corresponding to applied currents and/or external fields are deduced from these results. Most of the experimental results are explicable with these domain structures. The effects of applied currents and/or external fields are explained quantitatively by a simple square model. The loss component of the ac susceptibility measurements is explained by solving a similar problem based on a cylindrical shape. The measured out-of-phase and in-phase components of ac susceptibility are explained for the most part with the calculation based on the model. The behavior in low fields is not explicable on the basis of the model. In Chapter 5, a theoretical magnetic configuration is generated using a vector potential suggested by the domain structures



deduced from the experimental results. By minimizing the total energy with respect to Ritz parameters defining the vector potential, a quantitative description of the domain configurations corresponding to currents and/or external fields is obtained. This micromagnetic approach justifies the simpler domain treatment used in Chapter 4. A brief summary and conclusions follow in Chapter 6.

# Chapter 2

## Reviews of Micromagnetism, AC Susceptibility, and Magnetoresistance

Brown's monographs<sup>10,11</sup> "Magnetostatic Principles in Ferromagnetism" and "Micromagnetics" provide the fundamentals of micromagnetics. The aim of static applications of micromagnetics is to determine the vector fields describing magnetization patterns.<sup>12-16</sup> The equations of micromagnetics are an integro-differential set known as Brown's equations.<sup>17</sup> Solutions of these equations are very difficult to obtain even for simple geometries.<sup>18,19</sup> For other cases, it is impossible to obtain rigorous solutions. In this chapter, a brief review of micromagnetics is given and the energy terms involved in the total energy are introduced. The characteristic magnetic response of a <100> iron whisker<sup>9,20</sup> and the interpretation of its ac susceptibility<sup>21,22</sup> are described. The dependence of resistance upon domain orientation and direction of applied current is discussed.<sup>6,23</sup> The magnetic field from an applied current is derived. The Gaussian system of units is used in this thesis.

### 2.1 Micromagnetism

Micromagnetism has been proven to be an effective tool for studies of static magnetic states<sup>24,25</sup> and magnetization processes.<sup>26,27</sup> In micromagnetics, the magnetization in a ferromagnetic material is

described by a vector field  $\vec{M} = M_s(\alpha_m \hat{x} + \beta_m \hat{y} + \gamma_m \hat{z})$ . The magnetization is of constant magnitude  $M_s$ , and its direction is given by  $\hat{n}_M = \alpha_m \hat{x} + \beta_m \hat{y} + \gamma_m \hat{z}$ , where  $\alpha_m$ ,  $\beta_m$ , and  $\gamma_m$  are the directions cosines of the magnetic moment vector and  $\hat{x}$ ,  $\hat{y}$ , and  $\hat{z}$  are unit vectors in rectangular coordinates. The existence of domains and domain walls can be derived using the calculus of variations rather than by postulating their existence as is done in domain theory.<sup>28</sup> The four major contributions to the total energy are (a) the exchange energy, (b) the magnetostatic self-energy, (c) the magnetocrystalline anisotropy energy, and (d) the energy of interaction with the external field. In general, there also may be the contribution of the magnetoelastic energy.<sup>23</sup> To simplify the situation the magnetoelastic energy will not be considered except to the extent that it contributes slightly to the anisotropy energy. If the whisker were treated as a rigid body there would be no magnetoelastic effect, but then the two 90° sections of a 180° wall would not be held together.

### 2.1.1 Exchange Energy

In the Heisenberg model of ferromagnetism the exchange energy originates from the interaction between spins on two atoms. The exchange energy between spins  $i$  and  $j$  is expressed in the form  $W_{ij} = -2J_{i,j}S_i^2 \cos \varphi_{ij}$  where  $J_{i,j}$  is an exchange constant,  $S_i$  is the spin angular momentum, and  $\varphi_{ij}$  is the angle between the two spins. For nearest neighbors only, the exchange energy is

$$E_\alpha = \frac{1}{2} \sum_{i=1}^N \sum_{j=1}^N W_{ij} = -J_\alpha S_s^2 \sum_{i=1}^N \sum_{j=1}^N \cos \varphi_{ij} \quad \text{Eq. 2.1.1}$$

where the summation  $j$  is over the number of nearest neighbors  $n$  for each atom and the summation  $i$  is for all atoms  $N$ .  $J_{ex}$  is the nearest neighbor exchange constant. If the angles between spins are small on the scale of atomic distances, the exchange energy can be expressed using the leading term in a series expansion. The sum can be replaced by an integral over the volume  $V$  of a magnetic material where the integrand is the sum of the squares of the spatial derivatives. For a cubic crystal,<sup>12</sup>

$$E_{\alpha} = A_{\alpha} \int_V ((\nabla\alpha_m)^2 + (\nabla\beta_m)^2 + (\nabla\gamma_m)^2) d\tau + E_{\alpha,0} \quad \text{Eq. 2.1.2}$$

where  $A_{\alpha}$  is the exchange constant and  $d\tau$  is the volume element. For a body-centered cubic crystal,  $A_{\alpha} = \frac{2J_{\alpha}S^2}{a_0}$  where  $a_0$  is the length of the edge of the cubic unit cell. The exchange energy is a minimum when all the spins are parallel to each other.

## 2.1.2 Magnetostatic Self-Energy

In electrostatics, volume and surface charges are used to calculate potentials and electric fields in a medium. In micromagnetics, the sources of the demagnetizing field,  $\vec{H}_D$ , are  $\rho_m \equiv -\nabla \cdot \vec{M}$  and  $\sigma_m \equiv \hat{n} \cdot \vec{M}$  where  $\hat{n}$  is a unit vector normal to the surface.  $\rho_m$  and  $\sigma_m$  are treated as magnetic volume charge density and magnetic surface charge density, respectively.  $\vec{H}_D$  is calculated at each point  $\vec{r}$  using

$$\begin{aligned} \vec{H}_D(\vec{r}) &= \int_V \frac{\rho_m(\vec{r}')(\vec{r} - \vec{r}')}{|\vec{r} - \vec{r}'|^3} d\tau' + \int_S \frac{\sigma_m(\vec{r}')(\vec{r} - \vec{r}')}{|\vec{r} - \vec{r}'|^3} dS' \\ &= \int_V \frac{-\nabla' \cdot \vec{M}(\vec{r}')(\vec{r} - \vec{r}')}{|\vec{r} - \vec{r}'|^3} d\tau' + \int_S \frac{\vec{M}(\vec{r}') \cdot \hat{n}(\vec{r} - \vec{r}')}{|\vec{r} - \vec{r}'|^3} dS', \quad \text{Eq. 2.1.3} \end{aligned}$$

where  $|\bar{r} - \bar{r}'|$  is the distance between the field point and the source point.

The magnetostatic self-energy, called the demagnetizing energy, is

$$E_D = -\frac{1}{2} \int_V \bar{M} \cdot \bar{H}_D d\tau. \quad \text{Eq. 2.1.4}$$

This energy is always positive.<sup>11</sup> When there are neither charges inside nor on the surface of the material, the demagnetizing energy vanishes.

### 2.1.3 Magnetocrystalline Anisotropy Energy

The spontaneous magnetization prefers to lie along certain crystallographic directions, called easy axes, to lower the energy in a magnetic material. If the magnetization is rotated away from an easy axis, e.g., by applying an external field, the field does work which is stored as an increase in the magnetocrystalline anisotropy energy. For a cubic crystal, the leading terms in the anisotropy energy are

$$E_K = \int_V \{K_1(\alpha_m^2\beta_m^2 + \alpha_m^2\gamma_m^2 + \beta_m^2\gamma_m^2) + K_2\alpha_m^2\beta_m^2\gamma_m^2\} d\tau \quad \text{Eq. 2.1.5}$$

where  $K_1$  and  $K_2$  are the anisotropy constants,<sup>23</sup> and the directions are taken with respect to the cubic axes.

### 2.1.4 External Field Energy

The energy of a magnetic material with magnetization  $\bar{M}$  has a contribution from an external field,  $\bar{H}_o$ , given by

$$E_H = -\int_V \bar{H}_o \cdot \bar{M} d\tau. \quad \text{Eq. 2.1.6}$$

## 2.2 Characteristic AC Responses of a <100> Whisker

Domain structures and magnetic behaviors of <100> whiskers have been studied with several domain observation techniques. Coleman and Scott,<sup>1</sup> and DeBlois and Graham<sup>29</sup> extensively studied domain structures and domain movements for whiskers using the Bitter method. Recently, surface magnetization was investigated with high-resolution Kerr microscopy<sup>4,30,31</sup> and scanning electron microscopy with polarization analysis (SEMPA).<sup>5,32</sup> With these observation techniques, several stable domain structures and domain movements under the influence of fields have been identified. For example, in zero field in a well-grown <100> iron whisker the simple Landau structure can be observed as shown in Fig. 1. When an external field is applied along the principal axis of the whisker, the long domain wall is observed to be bowed parabolically.

Another example is the domain structure called the "Coleman" structure. When a high applied field is decreased, a structure which has a small spike-like domain is observed at a nucleation field.<sup>1</sup> The Coleman structure, different from the Landau structure, has one or two long 180° walls lying in a (011) plane running along the whisker. Fig. 4 shows the Coleman structure with two walls nucleated at edges of the whisker. As the external field is decreased toward zero field, the area of the reversed domains increases. The structure is metastable and eventually changes to the Landau structure as the external field is further decreased through zero and increased in the opposite direction.<sup>9,20</sup>

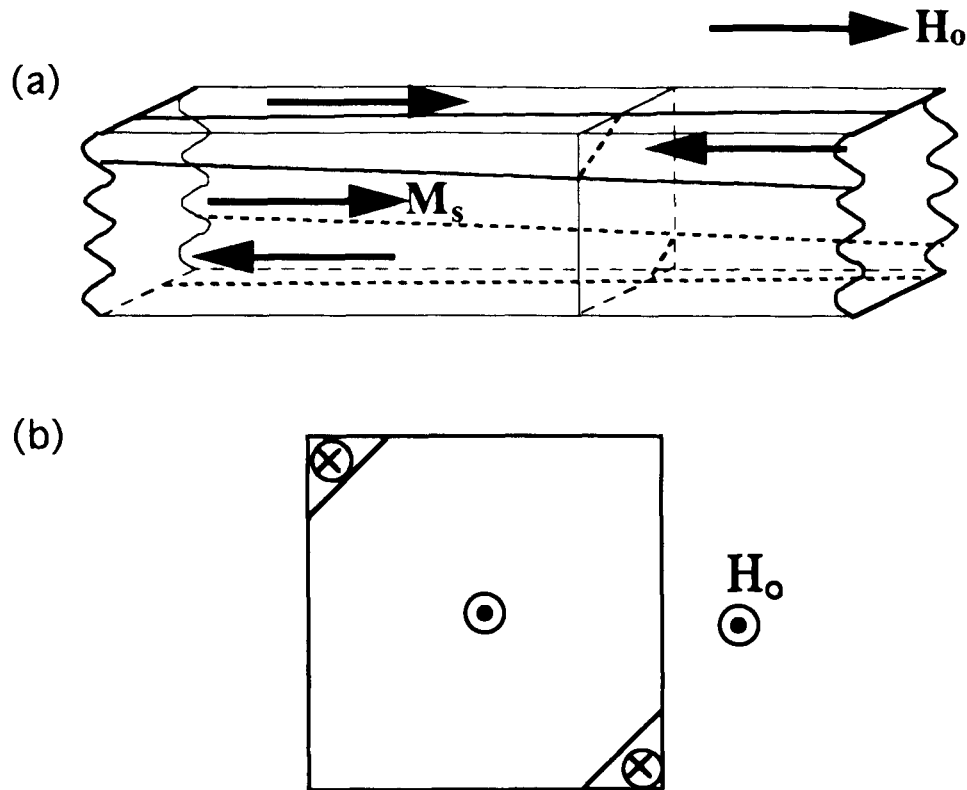


Fig. 4. Coleman structure nucleated with two domain walls.  
 a) 3D for a  $\langle 100 \rangle$  whisker,  
 b) for its cross section.

The techniques which first identified various structures were based on surface observations and did not give enough information about the internal structures of the whiskers. Domain configurations inside the whiskers can only be guessed at from those observations. But the ac susceptibility measurement,<sup>9</sup> using an iron whisker as the core of a transformer, can be used to distinguish among several possible internal structures.

When an ac driving field is applied along the whisker, domain walls are vibrated. The changes in magnetic flux, which have the information about the domain structure, can be observed with a coil

wound around the whisker. Heinrich and Arrott<sup>9</sup> observed the characteristic ac magnetic response of a well-grown  $\langle 100 \rangle$  iron whisker in various dc external fields. A schematic diagram of the experimental arrangement is shown in Fig. 5. The in-phase component and the out-of-phase component of the ac signal were detected with the two-turn pick-up coil at the center of the whisker as shown in Fig. 5. The in-phase component is related to the demagnetizing field and the out-of-phase component to eddy current losses. These relations are discussed in detail in Section 2.3. During the measurements, the dc magnetic field was changed slowly while the ac driving field was fixed at 700 Hz. The experimental method will be discussed further in Section 3.3.

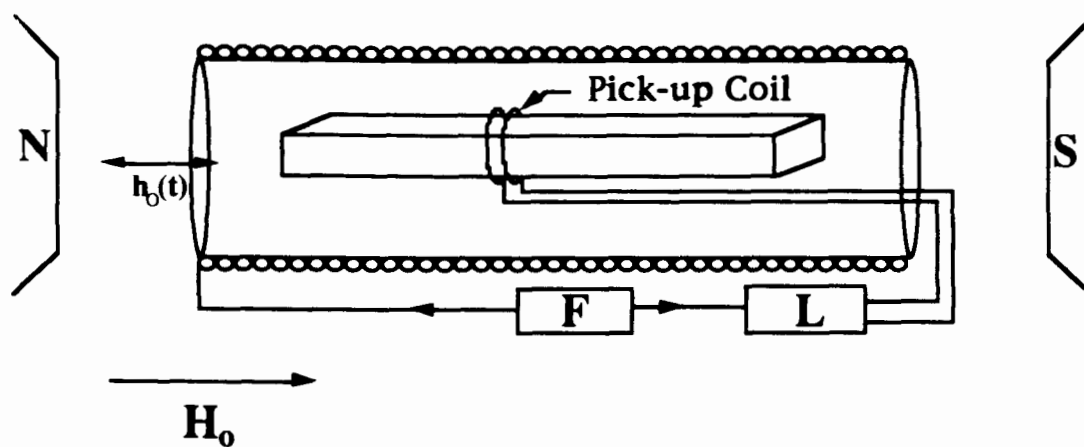


Fig. 5. Experimental set-up for the ac susceptibility measurement. where  $H_0$  is the dc external field,  $h_0(t)$  is the ac external field. F is a function generator, and L is a lock-in amplifier

Typical ac response curves for a  $\langle 100 \rangle$  whisker are shown in Figs. 6(a) and (b). As the dc external field varies, the out-of-phase component of the induced ac signal changes drastically. Fig. 6(a)



shows the out-of-phase component of the ac susceptibility,  $\chi''$ , for a  $\langle 100 \rangle$  whisker. Fig. 6(b) is the in-phase signal  $\chi'$ . Domain structures corresponding to various external fields can be deduced from Figs. 6(a) and (b). The detailed relations between the possible

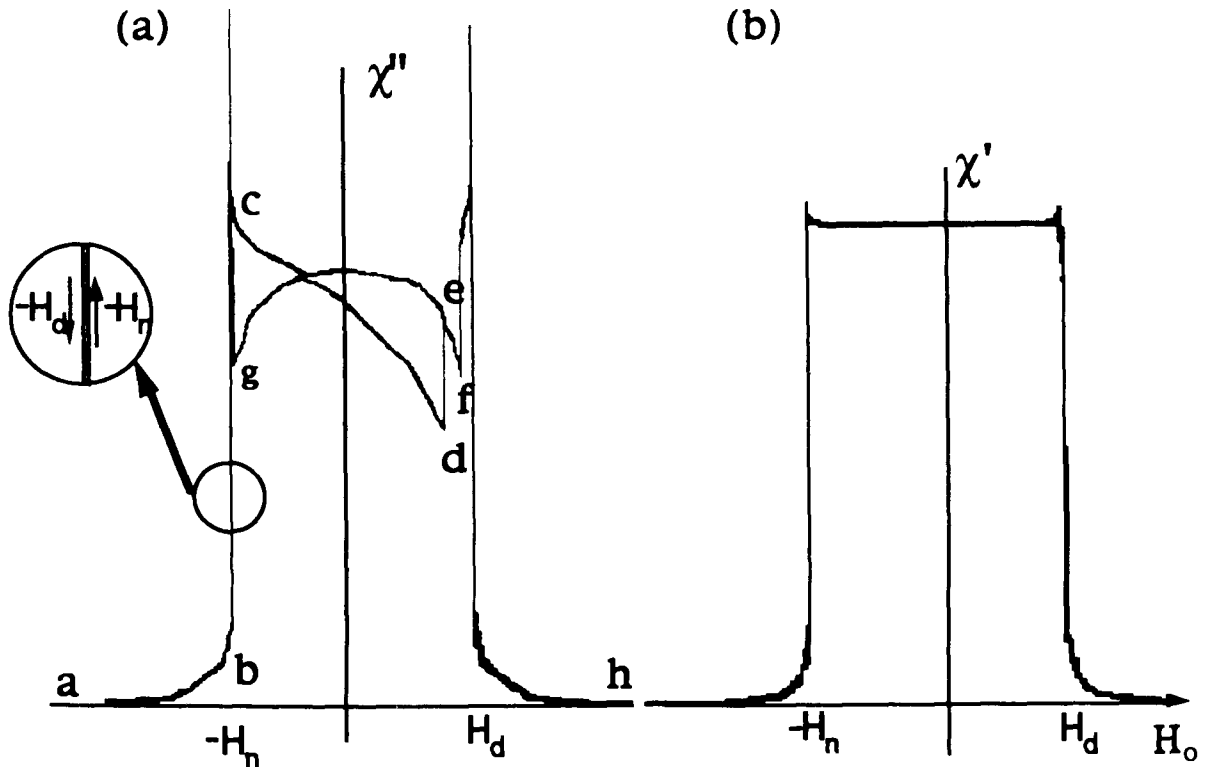


Fig. 6. Characteristic differential susceptibility for a  $\langle 100 \rangle$  iron whisker measured with driving frequency 700 Hz.  
a) out-of-phase and b) in-phase components.  
Points (a) to (h) are discussed in the text.

domain structures and the out-of-phase signal are well described by Heinrich and Arrott.<sup>9</sup> Fast movement of the domain wall induces a large out-of-phase signal. The out-of-phase signal depends on the number of walls, sizes, and positions. As a wall becomes larger, it

moves more slowly in compensating for changing external field. The slower movement of the wall induces a smaller eddy current. In general, eddy current damping is reduced when the walls are large in area and/or near the surfaces.<sup>33,34</sup>

The magnetization processes can be understood by following the out-of-phase component of the ac signal. The points (a) to (h) refer to Fig. 6(a). Start at point (a) where the whisker is saturated at the center by a strong external field in a negative direction. The external field is strong enough to saturate the central cross section but not necessarily the whole whisker. Initially there is no out-of-phase signal under the strong field. As the magnitude of the field is decreased towards the nucleation field,  $H_n$ , a small signal is observed. The small signal is due to magnetization changes elsewhere in the whisker, not near the pick-up coil in the plane of the central cross section. The Coleman structure with one or two domain walls with  $\{110\}$  planes is nucleated at field  $H_n$ , (b) in Fig. 6(a). On nucleation of the Coleman structure the in-phase and out-of-phase signals increase sharply from points (b) to (c). If the field were now slightly changed from point (c) towards point (b), the ac signal would first increase until reaching the departure field,  $H_d$ , at which the signal decreases dramatically. The departure field,  $H_d$ , is defined as the field necessary to just saturate the center of the whisker, not the whole whisker. At higher negative fields than  $H_d$ , the Coleman structure disappears from the center of the whisker. When the field changes in the positive direction from  $H_n$ , point (c), crossing zero field to point (d), the out-of-phase signal decreases almost linearly with the external field. The decreasing out-of-phase

signal can be interpreted as an increase in the size of the reversed domains of the Coleman structure with changing external field. Since the Coleman walls initially are small near  $H_n$ , they must move quickly to expel the external field resulting in a large out-of-phase signal. As they grow larger, they move more slowly resulting in a smaller out-of-phase signal. Between points (c) and (d), the magnetic process is reversible. At point (d), the structure is changed into the stable Landau domain structure.

The external magnetic field,  $H_o$ , necessary to transform the Coleman structure to the Landau structure is not consistent; it depends on the field history of the whisker. In the case of two Coleman walls, an external field larger than that for a single Coleman wall is necessary to change the domain structure into the Landau structure. For most good  $\langle 100 \rangle$  whiskers, the transformation from the Coleman structure to the Landau structure occurs at two thirds of  $H_d$ . After the Coleman to Landau transition, the Landau domain structure is stable over a wide range of external fields, between points (g) and (f). For these fields, except for  $H_o = 0$ , the  $180^\circ$  domain wall in the Landau structure is bowed parabolically. When the external field increases from points (e) to (f), the  $180^\circ$  wall becomes bowed further. As the field passes through point (f), the simple domain structure changes to a complicated domain structure before saturation. The out-of-phase signal for a good  $\langle 100 \rangle$  whisker at point (f) is decreased to about half of the intensity at zero field. Hartmann observed that before the  $180^\circ$  wall touches the edge of the whisker, points (g) or (f), the wall collapses, leading to the nucleation of  $90^\circ$  closure domains.<sup>35</sup> The nucleation makes the out-of-phase signal

increase discontinuously. The induced out-of-phase signal on nucleation of this domain structure is similar to the one obtained with the Coleman structure. As the external field increases to point (h), the walls are removed from the center of the whisker. When the external field reaches point (h), the whisker is saturated at its center and its out-of-phase signal is greatly diminished.

Fig. 6(b) shows that the in-phase component of the induced signal is constant for all but the regions of the departure fields. This means that the in-phase signal is fairly independent of the static positions of the walls. The transition from the Coleman structure to the Landau structure, observed with the out-of-phase signal, is not seen with the in-phase signal for low driving field frequency. Large changes in the in-phase signal at the departure and nucleation fields are observed. When the applied field is larger than the departure field, the whisker is already saturated at the center. The residual in-phase signal decreases slowly when an external field larger than the departure field is applied along the whisker. The slow decrease of the in-phase signal is due to magnetization rotations in regions away from the center of the whisker, which change the demagnetizing field in the pick-up coil. The characteristic ac response curve is strongly dependent on the driving frequency. Heinrich and Arrott<sup>9</sup> fully discuss these processes from dc to 200 kHz.

Although we have assumed a Landau domain structure between points (g) and (f), we may have a diamond domain structure. The behavior of the diamond domain structure, shown in Fig. 7, is similar to that of the Landau structure. This behavior can

not be distinguished from that of the Landau structure by ac susceptibility measurements.<sup>35,36</sup> If a whisker shows the typical ac magnetic response curve, as in Fig. 6(a), the whisker is treated here as having a Landau domain structure.

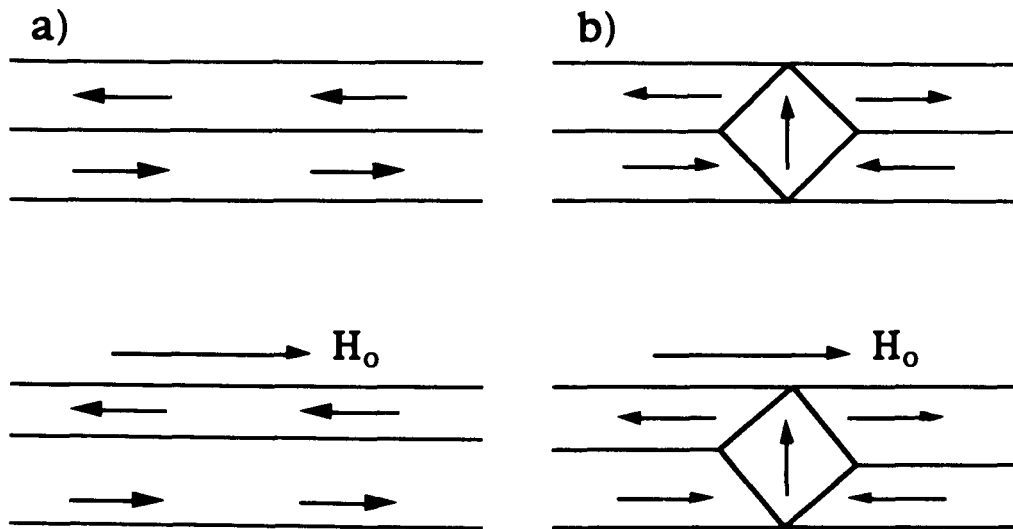


Fig. 7. Two similar states a) a Landau structure and b) a diamond structure without field (upper panels) and with field (lower panels).

The following features of the ac susceptibility have been used to judge the quality of whiskers throughout this thesis. At first, large discontinuous increases in the out-of-phase signal have to be observed at the departure field,  $H_d$ , and the nucleation field,  $H_n$ . When the field goes from  $H_n$  in one direction towards  $H_d$  in the opposite directions, the transformation from the Coleman structure to the Landau structure must occur somewhere near or beyond zero field. After this transformation, the out-of-phase signal must change

smoothly over the field range where the Landau structure is stable. For a good  $\langle 100 \rangle$  whisker, the Landau structure is not transformed to another structure until the field is close to the departure field. For damaged or strained samples, these features are not observed. Samples without Landau structures show the following typical responses. The nucleation of the Coleman structure is not observed clearly. Especially for a strained sample, the transformation from the Landau structure to a complicated structure occurs far below  $H_d$ . The magnetic responses for damaged whiskers are quite different from those of good  $\langle 100 \rangle$  iron whiskers. Such a response for a damaged whisker will be shown in Fig. 18 in Chapter 4.

### 2.3 Interpretation of the AC Susceptibility Measurement

As explained in the previous section, a strong dc external field displaces the domain walls of an iron whisker and an ac driving field vibrates the domain walls. The vibration accompanies the change in magnetic flux inside the specimen at the vibration frequency. A coil wrapped around the whisker picks up the change in the magnetic flux, which carries information about the domain wall displacement. If a magnetic material is magnetized by the ac driving field, the local field will have contributions from the applied field,  $h_0 e^{i\omega t}$ , the ac demagnetizing field,  $-h_d e^{i\omega t}$ , and the ac eddy current field,  $h_e e^{i\omega t}$ . The last two terms are related to magnetic fields produced by the motions of walls. These fields along the principal axis are complex numbers which have in-phase and out-of-phase components. The

changing magnetic flux through a pick-up coil<sup>37</sup> due to the driving field is  $\phi e^{i\omega t}$  where

$$\phi = h_o A_p + 4\pi \langle m \rangle A_s - h_D A_s + \int_{A_s} h_s(\vec{r}) da - \int_{A_p - A_s} h_D(\vec{r}) da \quad \text{Eq. 2.3.1}$$

where  $\langle m \rangle e^{i\omega t}$  is the changing magnetization, due to the motion of walls, averaged over the cross section.  $A_s$  is the cross-section of the whisker and  $A_p$  is the cross-section of the pick-up coil. The demagnetizing field is constant over the central cross section but then decreases rapidly with distance outside the whisker. The voltage induced in the pick-up coil can be calculated from the rate of change of magnetic flux, i.e.,  $i\omega\phi e^{i\omega t}$ .

The internal field is defined as

$$\vec{H}_i \equiv \vec{H}_o(t) + \vec{H}_D(t) + \vec{h}_s e^{i\omega t} \quad \text{Eq. 2.3.2}$$

where the notation  $\vec{H}_o(t)$  is to distinguish the time dependent applied field from the dc applied field,  $\vec{H}_o$ , which it includes. In a whisker with the Landau structure, the wall moves to maintain  $H_i = 0$  at the wall. As an external field is applied to a magnetic material, a demagnetizing field is generated and tends to exclude the external field. The ballistic demagnetizing field is defined as

$$H_D = -4\pi D \langle M \rangle \quad \text{Eq. 2.3.3}$$

where  $D$  is the demagnetizing factor and  $\langle M \rangle$  is the magnetization averaged over the central cross section at the pick-up coil of the magnetic material. The demagnetizing factor has been calculated by Bloomberg in his thesis.<sup>35</sup> In case of a bar of a square cross section, an approximation yields an analytic expression

$$D = \frac{4}{\pi} w^2 \left[ \ln \frac{1}{w} - 1.099 \right] \quad \text{Eq. 2.3.4}$$

where  $w$  is the ratio of the width to the length of the sample. The demagnetizing factor is dependent on the relative dimensions of the whisker. The external field is opposed by the demagnetizing field. For a  $\langle 100 \rangle$  whisker with the Landau structure, the dc external field is canceled by the dc demagnetizing field. The demagnetizing field arises from surface charges that are produced by normal components of the magnetization at each surface and by volume charges on the walls which in these configurations are almost negligible. The demagnetizing field is uniform throughout the whisker. The induced surface charge density increases linearly with the distance along the whisker from the middle of the whisker. As the applied field increases, more magnetic charges are induced on the surfaces to oppose the external field until the external field reaches the departure field. At the departure field,  $H_d$ ,

$$\langle M \rangle = M_s$$

in the central cross-section and the departure field is equal to the demagnetizing field and corresponds to saturation of the central cross section

$$|H_d| = |H_D| = |4\pi D M_s|. \quad \text{Eq. 2.3.5}$$

An apparent intrinsic dc susceptibility for the central cross section can be defined as

$$\chi_i \equiv \partial \langle M \rangle / \partial H_i. \quad \text{Eq. 2.3.6}$$

For paramagnetic materials this apparent susceptibility is the actual susceptibility, an intrinsic material property. For the iron whisker it



is not an intrinsic property, but depends on the details of the domain configurations. An effective external dc susceptibility can be defined as

$$\chi_{\alpha} \equiv \partial \langle M \rangle / \partial H_o. \quad \text{Eq. 2.3.7}$$

Using Eqs. 2.3.2 and 2.3.3, these dc susceptibilities ( $h, e^{i\omega} = 0$ ) are related by

$$1/\chi_{\alpha} = 1/\chi_i + 4\pi D. \quad \text{Eq. 2.3.8}$$

For a very high apparent intrinsic susceptibility, the internal field approaches zero and the measured effective susceptibility ( $\chi_{\alpha} \approx 1/4\pi D$ ) is determined by the shape of the sample. As the ratio of the width to the length of a rectangular sample becomes smaller, the effective susceptibility increases.<sup>9,38</sup>

For a material in the shape of a whisker with low intrinsic susceptibility, the magnetization remains almost constant until close to the end. The magnetic charges near the end of the sample generate a demagnetizing field which is weakest at the central cross section and becomes stronger near the ends. The effective susceptibility is close to the intrinsic one for a low intrinsic susceptibility.

If an instability exists in a magnetic material, the apparent intrinsic susceptibility becomes negative. The effective susceptibility then becomes larger than  $1/4\pi D$ . At nucleation and departure, a negative susceptibility is observed; see Fig. 6.

The ac magnetic response of an iron whisker to an ac driving field can be described using a model of a spring with damping but

negligible mass. The ac magnetic response,  $me^{i\omega t}$ , can be described in terms of the magnitude of the internal ac magnetic field  $h_i$  by<sup>9,37,39</sup>

$$m = \langle m \rangle = \chi_i h_i = \frac{1}{\alpha_i(\omega) + i\omega\beta_i(\omega)} h_i \quad \text{Eq. 2.3.9}$$

where  $\alpha_i(\omega)$  is the intrinsic magnetic stiffness and  $\beta_i(\omega)$  is the magnetic viscosity. From Eqs. 2.3.8 and 2.3.9, the effective susceptibility is given by

$$\frac{1}{\chi_{\text{eff}}} = 4\pi D + \alpha_i(\omega) + i\omega\beta_i(\omega) \quad \text{Eq. 2.3.10}$$

and can be rewritten as

$$\chi_{\text{eff}} \equiv \chi' - i\chi'' = \frac{4\pi D + \alpha_i(\omega) - i\omega\beta_i(\omega)}{(4\pi D + \alpha_i(\omega))^2 + (\omega\beta_i(\omega))^2} \quad \text{Eq. 2.3.10a}$$

where  $\chi'$  is the in-phase component of the ac susceptibility and  $\chi''$  is the out-of-phase component. It is assumed that the demagnetizing factor for the ac response is the same as for the dc response if the frequency is low. This neglects the effect of eddy currents on the redistribution of magnetization required to create the surface charges. For the low frequencies considered in this thesis, this should be a good approximation

When highly conductive materials are magnetized, the most important source of magnetic viscosity is from eddy currents. The eddy currents are determined by the position and velocity of the domain wall.<sup>40</sup> The demagnetizing and eddy current fields oppose the applied magnetic field. At low frequencies the in-phase component of the induced signal is primarily determined by the demagnetizing field. The out-of-phase signal is a direct measure of the losses in the system. In the low frequency limit, the measured

in-phase component of the ac susceptibility is proportional to the inverse of the effective stiffness and the out-of-phase component is directly proportional to the damping.<sup>9</sup> In the high frequency limit, the in-phase signal vanishes as  $1/\omega^2$  and the out-of-phase component decreases in proportion to  $1/\omega$ .

## 2.4 Magnetoresistance of an Iron Whisker

Magnetoresistances of iron whiskers with [100] and [111] axes have been studied over wide ranges of temperature, magnetic field and stress.<sup>3,6</sup> The magnetoresistance strongly depends not only on the temperature but also on the crystal orientation in both low and high magnetic field regions.<sup>41,42</sup> It was observed that the longitudinal resistance increased rapidly by about 0.1 % of the total resistance when low external fields were applied along the principal axis of a <100> whisker at room temperature.<sup>42</sup> This increase in the resistance is due to the changing directions of the magnetization in the various domains relative to current and crystal axes. The response shifts to a negative slope in high fields as shown in Fig. 8. This decrease is an intrinsic change in the resistance with high applied field. In this thesis, only the effects of domain orientations will be considered.

Magnetoresistance refers to the change in electrical resistance while applying an external field. The change in resistance depends on the direction of the magnetization and the direction of the measuring current with respect to the crystal axes. The relations among direction of current, domain orientations and resistance are

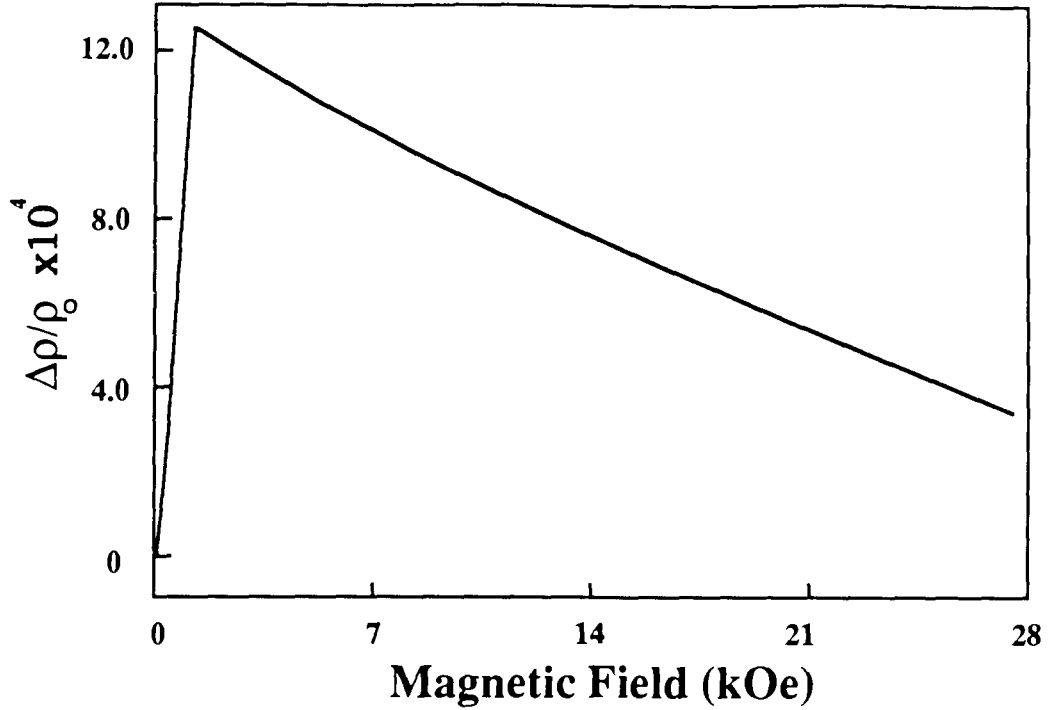


Fig. 8. Magneto-resistance of a <100> whisker at room temperature as observed by Coleman and Scott.<sup>1</sup>

experimentally well-established.<sup>6,7</sup> When a domain is magnetized in a direction  $\hat{n}_m = \alpha_m \hat{x} + \beta_m \hat{y} + \gamma_m \hat{z}$  while current is applied along a direction  $\hat{n}_c = \alpha_c \hat{x} + \beta_c \hat{y} + \gamma_c \hat{z}$ , the resistivity of a ferromagnetic cubic crystal can be expressed relative to a reference state as;<sup>43</sup>

$$\frac{\Delta\rho}{\rho_o} = \frac{\rho - \rho_o}{\rho_o} = \frac{3}{2} \frac{\Delta\rho_{100}}{\rho_o} (\alpha_m^2 \alpha_c^2 + \beta_m^2 \beta_c^2 + \gamma_m^2 \gamma_c^2 - \frac{1}{3}) + 3 \frac{\Delta\rho_{111}}{\rho_o} (\alpha_m \beta_m \alpha_c \beta_c + \alpha_m \gamma_m \alpha_c \gamma_c + \beta_m \gamma_m \beta_c \gamma_c) + \dots$$

Eq. 2.4.1

where  $\rho_o$  corresponds to the resistivity of polycrystalline iron with demagnetized (random) domain structure and  $\rho$  is the resistivity of the crystal with specified direction cosines. The reference state can also be achieved by appropriate choices of direction cosines, e.g.,

$\alpha_c = 1$ ,  $\alpha_m = \beta_m = \gamma_m = \frac{1}{\sqrt{3}}$ .  $\Delta\rho_{100}$  and  $\Delta\rho_{111}$  are the magnetoresistance constants which depend on the temperature and are determined experimentally.  $\alpha_m$ ,  $\beta_m$ , and  $\gamma_m$  are direction cosines of the magnetic moment vector, and  $\alpha_c$ ,  $\beta_c$ , and  $\gamma_c$  are those of the applied current vectors, both with respect to a set of the cubic axes. When the current is along a cubic axis and the magnetization is along a perpendicular cubic axis,  $\alpha_c = 1$  and  $\beta_m = 1$  or  $\gamma_m = 1$ , this is called the rotated state and the change in the resistivity is

$$\Delta\rho_{rot.[100]} = -\frac{\Delta\rho_{100}}{2}. \quad \text{Eq. 2.4.2}$$

In the case when the magnetization and current are directed along a cubic axis, called the saturated state,  $\alpha_c = 1$  and  $\alpha_m = 1$ , the change in the resistivity is

$$\Delta\rho_{sat.[100]} = \Delta\rho_{100}. \quad \text{Eq. 2.4.3}$$

The difference in the resistivity between the two states is

$$\Delta\rho_{max} = \Delta\rho_{sat.[100]} - \Delta\rho_{rot.[100]} = \frac{3}{2}\Delta\rho_{100}. \quad \text{Eq. 2.4.4}$$

We now turn to the specific case of a  $\langle 100 \rangle$  whisker. The whisker is partially saturated as shown in Fig. 2(c). In order to calculate the change in resistance with degree of saturation we will assume that the field and the current are parallel along the whisker axis and uniform in all cross sections. The resistivity of the central domain is different from that of surrounding domains. The two regions are treated as if they are conducting in parallel. When the domain structure is changed from the saturated state to the partially saturated state, the change in the resistance,  $\Delta R$ , for a length  $L$  is given as

$$\begin{aligned}
\Delta R &= R_{\text{rot.}[100]} - R_{\text{p.s.s}} \\
&= \frac{(\rho_o + \Delta\rho_{100})L}{(2d)^2} - \left( \frac{1}{\frac{(\rho_o + \Delta\rho_{100})L}{(2q)^2}} + \frac{1}{\frac{(\rho_o - \Delta\rho_{100}/2)L}{((2d)^2 - (2q)^2)}} \right)^{-1} \\
&= \frac{(\rho_o + \Delta\rho_{100})L}{(2d)^2} - \frac{(\rho_o + \Delta\rho_{100})\left(\rho_o - \frac{\Delta\rho_{100}}{2}\right)L}{(2q)^2\left(\rho_o - \frac{\Delta\rho_{100}}{2}\right) + ((2d)^2 - (2q)^2)(\rho_o + \Delta\rho_{100})} \\
&\approx \frac{\frac{3}{2}\Delta\rho_{100}(\rho_o + \Delta\rho_{100})((2d)^2 - (2q)^2)L}{(2d)^2(\rho_o(2d)^2 + \Delta\rho_{100}((2d)^2 - \frac{3}{2}(2q)^2))} \approx \frac{\frac{3}{2}\Delta\rho_{100}(1 - (\frac{q}{d})^2)L}{(2d)^2}
\end{aligned}$$

Eq. 2.4.5a

where  $R_{\text{p.s.s}}$  and  $R_{\text{rot.}[100]}$  are resistances for partially and fully saturated states, respectively. The width of the saturated domain is  $2q$  and  $2d$  is the width of the whisker, as shown in Fig. 2(c).

Measurement of  $\Delta R$  gives us information about the magnetic domain structure inside the iron whisker. Eq. 2.4.5a is rewritten in terms of the change in the magnetic flux as

$$\Delta R \approx \frac{\frac{3}{2}\Delta\rho_{100}(1 - (\frac{q}{d})^2)L}{(2d)^2} = \Delta R_{\text{max}} \frac{\phi_d - \phi_q}{\phi_d}, \quad \text{Eq. 2.4.5b}$$

where

$$\Delta R_{\text{max}} = R_{\text{rot.}[100]} - R_{\text{rot.}[100]} = \frac{\Delta\rho_{\text{max}}L}{4d^2}, \quad \text{Eq. 2.4.6}$$

$\phi_q = M_s(2q)^2$  and  $\phi_d = M_s(2d)^2$  are the magnetic flux for the partially and fully saturated whiskers, respectively, and  $R_{\text{rot.}[100]}$  is the resistance for the rotated state.

The coefficients  $\Delta\rho_{100} / \rho_o$  and  $\Delta\rho_{111} / \rho_o$  at room temperature (RT) and 20 °K were experimentally obtained for an iron plate by Tatsumoto.<sup>6</sup> From older experimental data, values at room temperature are given by Chikazumi.<sup>43</sup> Both sets are shown in

Table 2. In this thesis, our experimental data will be compared with Tatsumoto's coefficients.

Table 2. Magnetoresistance coefficients for iron and nickel.

	$\Delta\rho_{100} / \rho_o$	$\Delta\rho_{111} / \rho_o$	source
Fe(20°K)	$-5.3 \times 10^{-3}$	$1.1 \times 10^{-3}$	Tatsumoto <sup>6</sup>
Fe(RT)	$1.2 \times 10^{-3}$	$2.3 \times 10^{-3}$	"
Fe(RT)	$1.02 \times 10^{-3}$	$3.95 \times 10^{-3}$	Chikazumi <sup>43</sup>
Ni(RT)	$4.3 \times 10^{-3}$	$1.9 \times 10^{-2}$	"

## 2.5 Magnetic Field from the Applied Current

A magnetic field is produced when current flows through a conductor. The Biot-Savart law enables us to calculate the magnetic field generated by an electric current. This law gives the field contribution of a current  $I$  in an elemental length  $\delta\vec{l}$  of a conductor,

$$\delta\vec{H}_l = \frac{4\pi}{c} \frac{1}{4\pi r^2} I \delta\vec{l} \times \hat{n}, \quad \text{Eq. 2.5.1}$$

where  $r$  is the distance between the elemental length and the point of interest,  $\hat{n}$  is a unit vector along the radial direction,  $c$  is the speed of a light, and  $\delta\vec{H}_l$  is the contribution to the magnetic field at the point. Using the Biot-Savart law the  $x$ - and  $y$ -components of the magnetic field vector  $\vec{H}_l$  at the field point P for a non-magnetic infinitely long bar of rectangular cross section, as shown in Fig. 9, are

$$H_{l,x} = -\frac{2}{c} J \int_s \frac{\sin \alpha}{r} dS \quad \text{Eq. 2.5.2}$$

$$H_{l,y} = \frac{2}{c} J \int_s \frac{\cos \alpha}{r} dS \quad \text{Eq. 2.5.3}$$

where  $J = \frac{I}{ab}$  is the uniform current density passing through the bar of cross section  $S=ab$ . Substituting for  $\alpha$  and  $r$  as shown in Fig. 9, the x-component of the magnetic field becomes

$$H_{1,x} = -\frac{2I}{cab} \int_{-\frac{b}{2}}^{+\frac{b}{2}} dX \int_{-\frac{a}{2}}^{+\frac{a}{2}} \frac{y-Y}{(y-Y)^2 + (x-X)^2} dY. \quad \text{Eq. 2.5.2a}$$

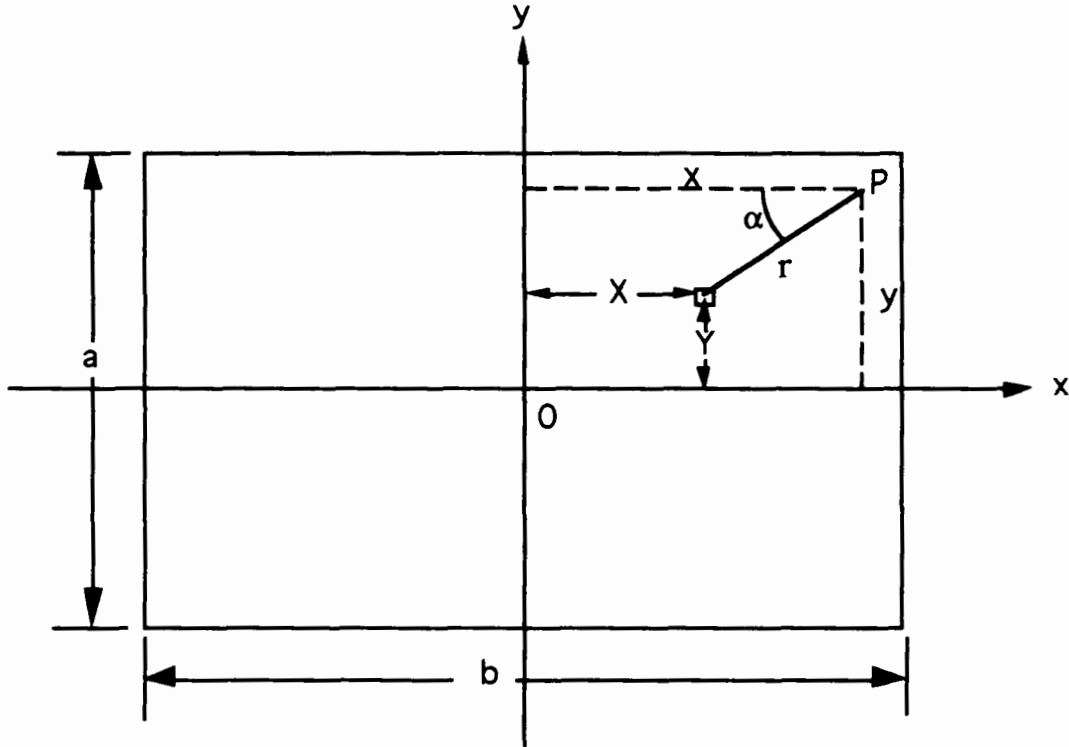


Fig. 9. Schematic diagram for calculating the magnetic field in a rectangular bar with a cross section  $ab$ . The source point is  $(X, Y)$  and the field point  $P$  is  $(x, y)$

As shown previously by Küpfmüller,<sup>44</sup> Eq. 2.5.2a becomes

$$H_{1,x} = -\frac{2I}{cab} \left\{ \frac{1}{2} \left( x + \frac{b}{2} \right) \ln \left[ \frac{\left( y + \frac{a}{2} \right)^2 + \left( x + \frac{b}{2} \right)^2}{\left( y - \frac{a}{2} \right)^2 + \left( x + \frac{b}{2} \right)^2} \right] - \frac{1}{2} \left( x - \frac{b}{2} \right) \ln \left[ \frac{\left( y + \frac{a}{2} \right)^2 + \left( x - \frac{b}{2} \right)^2}{\left( y - \frac{a}{2} \right)^2 + \left( x - \frac{b}{2} \right)^2} \right] \right. \\ \left. + \left( y + \frac{a}{2} \right) \left[ \tan^{-1} \left( \frac{x + \frac{b}{2}}{y + \frac{a}{2}} \right) - \tan^{-1} \left( \frac{x - \frac{b}{2}}{y + \frac{a}{2}} \right) \right] - \left( y - \frac{a}{2} \right) \left[ \tan^{-1} \left( \frac{x + \frac{b}{2}}{y - \frac{a}{2}} \right) - \tan^{-1} \left( \frac{x - \frac{b}{2}}{y - \frac{a}{2}} \right) \right] \right\}$$

$$\text{Eq. 2.5.4}$$



The  $y$ -component of the induced field  $H_{l,y}$  is found from Eq. 2.5.4 by replacing  $x$  with  $y$ , and  $a$  with  $b$ , and also by changing the sign of the magnetic field. The magnitude of the field from the current is given by  $H_l = \left( |H_{l,x}|^2 + |H_{l,y}|^2 \right)^{\frac{1}{2}}$ . Fig. 10 shows the distribution of the magnitude of the magnetic field in a 3D representation. Contour plots of the magnitude of the field from the current are shown in Figs. 11(a) and (b). As shown in Fig. 11(b), the largest magnetic field from the applied current is not at the corners of central cross section of a whisker but at the center of the surfaces on the whisker where the field direction lies in the surface plane.

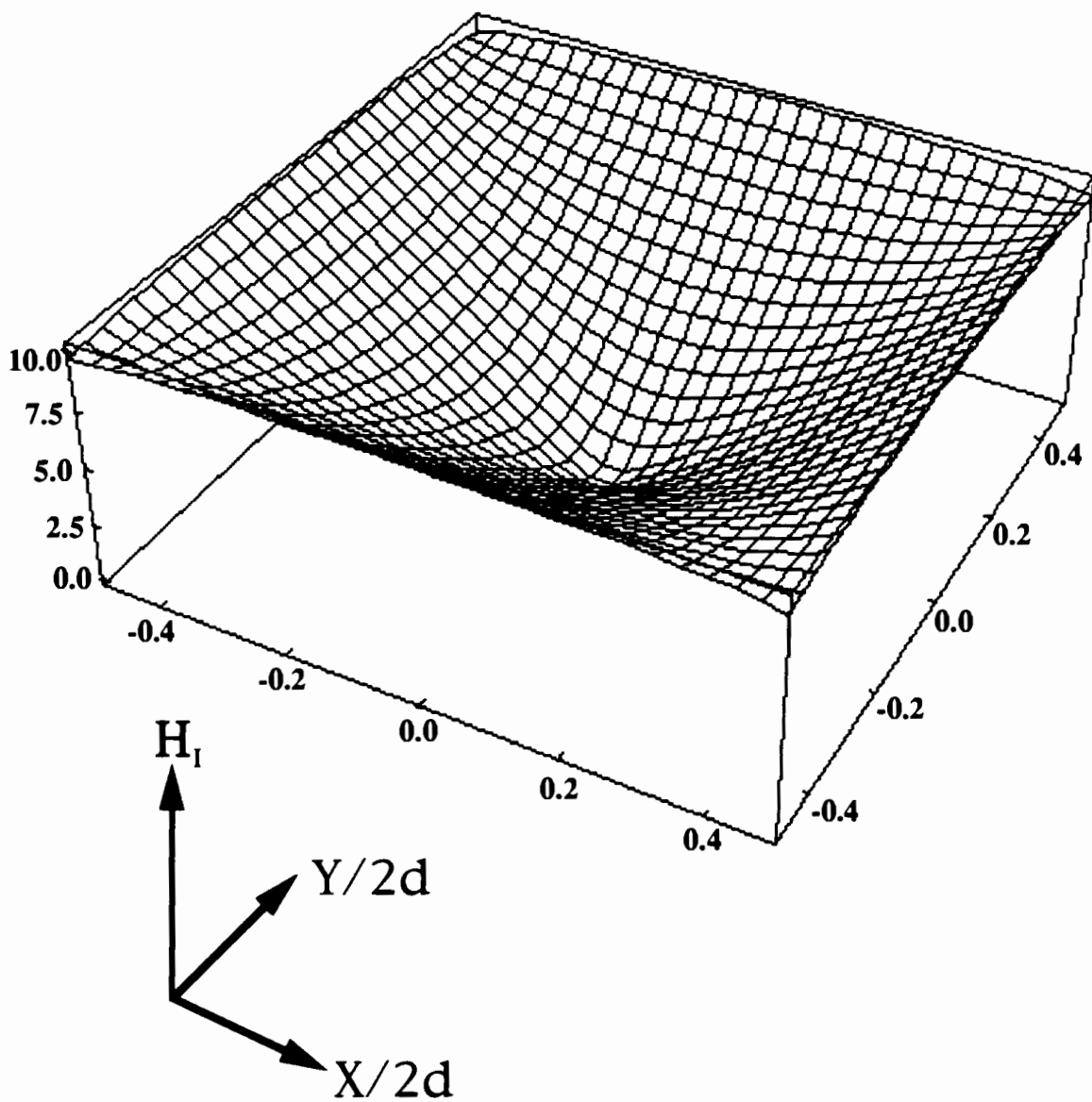


Fig. 10. The distribution of the magnitude of the magnetic field for a whisker passing a current of 300 mA. The whisker has a square central cross section with sides  $2d=a=b=100\ \mu\text{m}$ . ( $H_I$  is in units of Oe.)

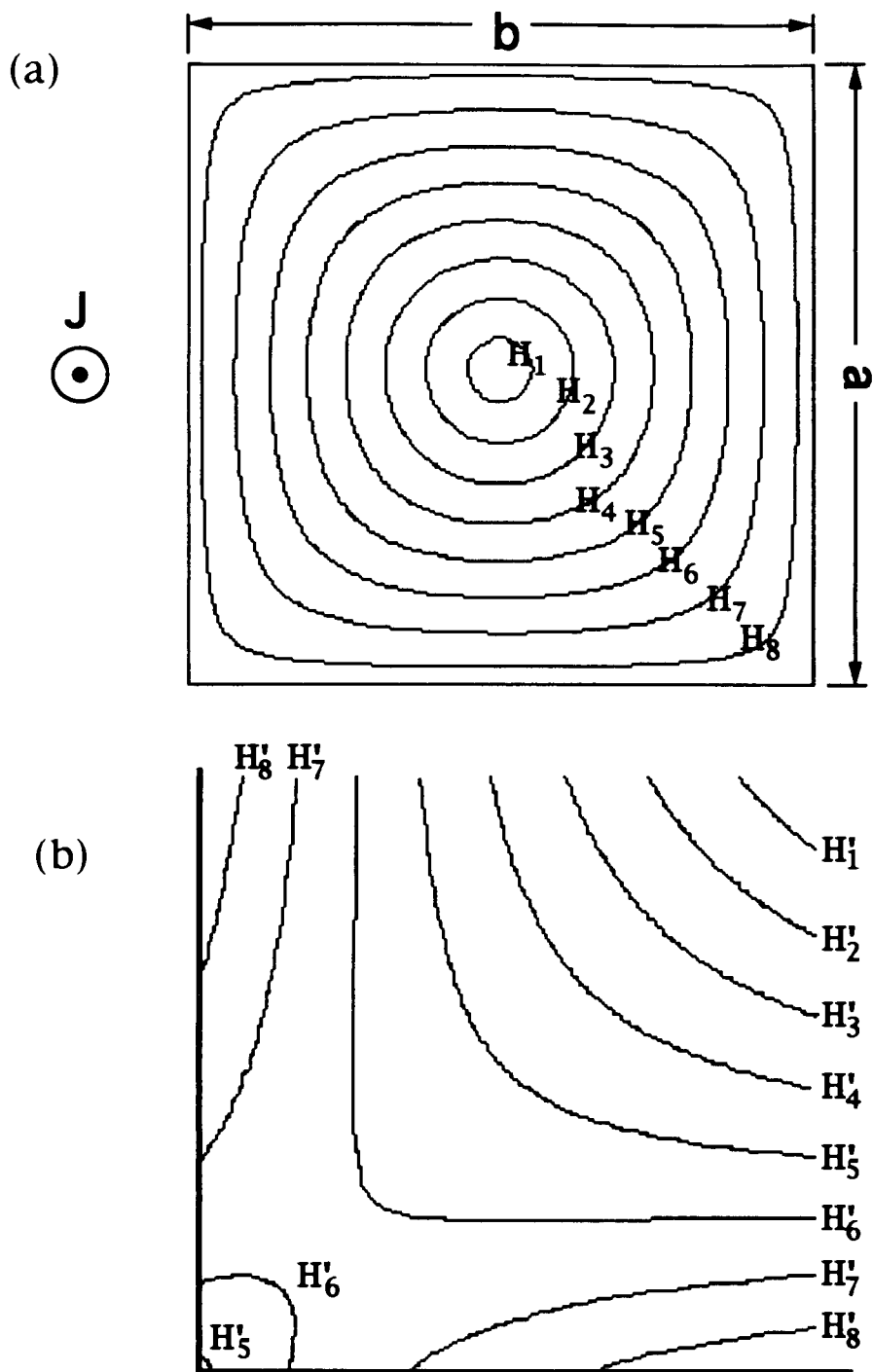


Fig. 11. Equally spaced contour plots for the situation of Fig. 10 for  
a) the central cross section and b) blow-up of a) at a corner.  
Plot of constant field magnitude

a)  $H_1=1.2$  Oe,  $H_2=2.4$  Oe ...  $H_8=9.6$  Oe,

b)  $H'_1=9.60$  Oe,  $H'_2=9.66$  Oe ...  $H'_8=10.1$  Oe.

# Chapter 3

## Experimental Methods

To learn about the domain structure inside a  $\langle 100 \rangle$  whisker we turn to two methods that will give information about the effect of applied currents and/or external fields. One is the dc resistance measurement. The resistance is slightly different if the magnetization of a domain is parallel or perpendicular to the applied current. The other is the ac susceptibility. The in-phase component of the ac susceptibility is determined by the restoring force from the competing terms in the energy. The out-of-phase component is sensitive to the growth of the  $90^\circ$  domain walls lying in  $\{100\}$  planes which generate eddy currents by the motion.

Brenner's techniques,<sup>45</sup> which were used to grow iron single crystals, are summarized in this chapter.

Resistance and ac susceptibility measurements were used to investigate the effects of applied currents and/or external fields on the domain structure inside a  $\langle 100 \rangle$  whisker. The experimental methods are presented in detail and a discussion on how to avoid stress on the whisker is given.

### 3.1 Growth of Iron Whiskers

Iron whiskers were grown by hydrogen reduction of ferrous chloride at approximately  $710^\circ\text{C}$ . The technique was developed by

Brenner.<sup>45</sup> Our growth system has been explained in detail by Hanham in his thesis.<sup>46</sup> Anhydrous ferrous chloride and 99.5% pure iron plates were used as starting materials.

A small iron plate (5 cm x 20 cm x 0.2 mm) was scraped and cleaned with acetone and distilled water. It was baked in a wet hydrogen flow for about 1.5 hours and then in a dry hydrogen flow for about one hour in a quartz tube to remove carbon from the surface of the plate. The wet hydrogen was obtained by passing hydrogen through a cylinder filled with water. The dry hydrogen was obtained by passing hydrogen through a cylinder cooled by liquid nitrogen. The baking temperature was about 735 °C. After the initial 2.5 hour baking in wet, then dry hydrogen, the plate was slowly cooled down for 1.5 hours in the dry hydrogen flow. The plate was shaped into a sample boat after cooling down. The sides were not bent more than 45°. Most of the whiskers subsequently grew on the sides of the boat.

All whiskers were grown in a two-zone furnace. Growth temperatures of 704 °C and 725 °C were used to grow whiskers in a slow dry hydrogen flow. About 62 g of the chemical anhydrous ferrous chloride was placed in the boat and baked in the furnace. The chemical emitted moisture and other gases for the first half hour during the approach to the growth temperature. Dry hydrogen was passed rapidly through the quartz tube to remove these gases. The flow rate was slowed down as soon as the growth temperatures were reached; the flow rate of dry hydrogen was then about 2 cm<sup>2</sup> per second with our set-up. Most of the whiskers nucleated during the first few hours. Controlling the temperature and the flow rate was important for making good whiskers. It took about 18-20 hours to complete the

whisker growth. For shorter growing periods, chemicals were left on the surfaces of whiskers. The quality of the whiskers depended on the chemical used (manufacturer, batch number and purity) and the growing conditions. Still, it is not certain what are the best conditions to make good single crystal whiskers.

Typically, well-grown  $\langle 100 \rangle$  whiskers have nearly square cross sections of  $20 \mu\text{m}$  to  $1000 \mu\text{m}$  on a side and lengths ranging from 3 mm to 40 mm. A well-grown  $\langle 100 \rangle$  whisker usually displays the Landau domain structure as shown in Fig. 1. Some  $\langle 111 \rangle$  whiskers are grown with six (110)-type side surfaces and a hexagonal cross section. Very rarely,  $\langle 110 \rangle$  whiskers are observed.

### 3.2 DC Resistance Measurements

For magnetoresistance measurements, a  $\langle 100 \rangle$  iron single crystal with typical dimensions  $\sim 200 \mu\text{m} \times \sim 200 \mu\text{m} \times \sim 20 \text{mm}$  was picked from a sample boat. The schematic diagram for the four-point probe measurement is shown in Fig 12. A fine glass capillary was used to protect the whisker. All wires for the measurement were glued onto the capillary. Originally, a silver paint was used to bond all of the fine copper wires to the whisker. As the silver paint solidified, stress built up in the whisker and the resulting magnetostriction caused the Landau domain structure to disappear. This was detected with ac susceptibility measurements. After determining the problem caused by stress, GaIn solder, which is a liquid at room temperature, was used as an adhesive to connect copper wires to the sides of the whisker. For connecting wires at ends of whiskers, silver paint was used

throughout.

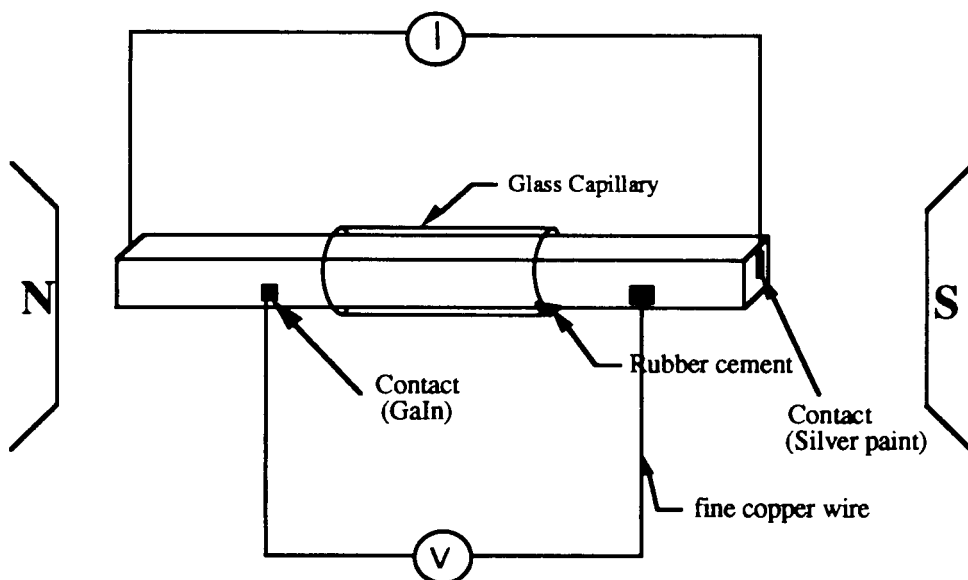


Fig. 12. Schematic diagram for the four-probe resistance measurement on a  $\langle 100 \rangle$  whisker.

A power supply was used for a constant current source. A nanovoltmeter with a 6-digit resolution was used to measure the voltage across the two probes attached to the sides of the whisker. To measure the current, a standard resistance,  $1\Omega \pm 0.005\%$ , and a voltmeter with six and half digit resolution were used. A gauss meter using the Hall effect was used to measure the external magnetic field. The whisker was put into a large oil bath to minimize the effect of temperature variations. Also, a bundle of a copper wire was used as a resistance thermometer to correct the data for temperature drifts. The length of wire was about 5 m. It was formed into a shape and size approximately equal to that of a typical whisker. The measurement was started after passing current through the whisker for about one half hour. Heat generated by the current was, by then, distributed

evenly throughout the oil bath.

Current was applied along the principal axis of the whisker to measure the longitudinal resistance and to create the domain pattern of Fig. 2(b) in the absence of an external dc magnetic field. A sufficiently large applied field will change the structure to one with the magnetization along the axis of the whisker. For measuring the resistance with an applied current and the desired field, the following methods were used. First, an external field high enough to saturate the central cross section was applied. The field necessary to saturate the magnetic moment in the central cross section depended on the dimensions of the whisker. The external field was chosen to be twice as large as the departure field. The resistance of the copper wire bundle and the voltages across the whisker and across the standard resistance were measured sequentially. The voltage across the standard resistance determined the current passing through the whisker. The resistance of the copper bundle which was sensitive to temperature changes was used to correct the whisker resistance derived from the voltages measured across the standard resistance and the whisker. Second, the magnetic field was adjusted to the desired field and the measurements of the voltages and the resistance were repeated. Third, again the measurements were repeated with the high external field. The repeated high field measurements further reduced the effect of temperature drift. The resulting high field resistances were averaged. This sequence was repeated for different desired fields. The range of the desired fields varied from the departure field to zero. After each sequence of measurements as just described, the applied current was changed and then the sequence of measurements



was repeated. Applied currents were between 30 mA and 600 mA. All of these currents were sufficient to produce the maximum magnetoresistance effect.

### 3.3 AC Susceptibility Measurements

A schematic diagram for the ac susceptibility measurements is shown in Fig. 13. An iron whisker with a  $\langle 100 \rangle$  orientation was chosen from a sample boat. The contacts on the sides of the whisker

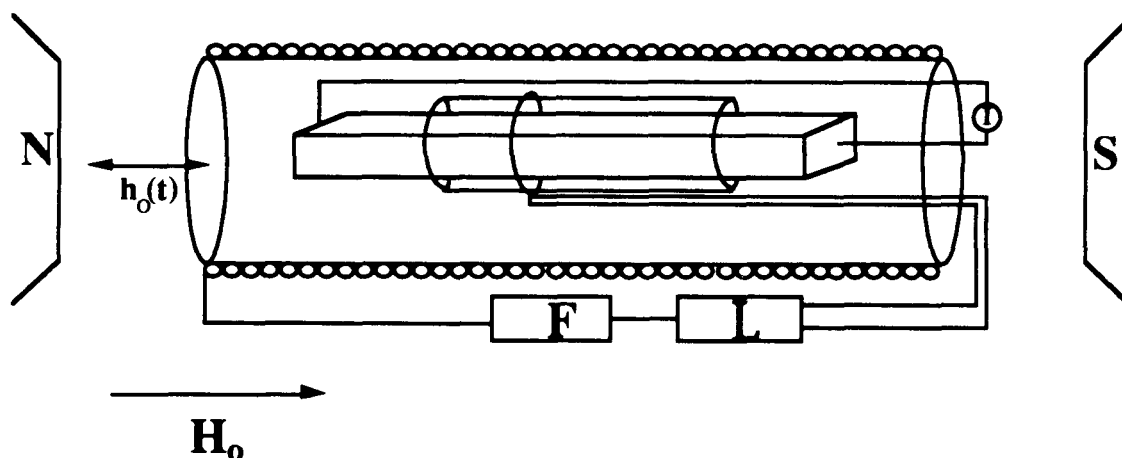


Fig. 13. Schematic diagram for the ac susceptibility measurements with current applied. F is a function generator, and L is a lock-in amplifier.

between copper leads and the whisker were made with GaIn solder to reduce stress. Silver paint was used for strength at the end contacts where stresses were not important. The sample was held in a glass capillary tube by rubber cement. The rubber cement remained flexible even after it was completely dry. The ac driving field was obtained by tightly winding a primary coil on a second concentric capillary tube. The primary coil had about 40 windings per cm and its length was

longer than the whisker. It was driven by a 0.1 to 25 kHz sine wave generator to produce ac fields in the range 10 to 100 mOe.

The secondary coil was tightly wound at the center of the whisker with as little as one or two turns on the first capillary tube. The induced signal from the pick-up coil went into a lock-in amplifier. It was necessary to adjust the phase angle to separate the out-of-phase and in-phase components of the induced signal. The phase angle was adjusted using the following standard procedure.<sup>9,46</sup> A longitudinal magnetic bias field was applied strong enough to saturate the iron whisker over much of its length. The whisker then no longer contributed to the signal in the pick-up coil and the phase angle of the lock-in amplifier was adjusted for a zero out-of-phase signal.

For each whisker the ac susceptibility measurement first was made with zero current in order to determine whether or not the sample had the Landau structure. When the sample had the Landau domain structure, the induced signals showed the characteristic magnetic responses as in Fig. 6. If the sample did not show this typical behavior, it was not used. After being satisfied that a whisker exhibited the Landau structure, the ac susceptibility measurement for the out-of-phase component was made while varying the applied current without an external magnetic field. This determined the critical currents which transformed the Landau structure to a complicated one and vice versa. A current, up to 750 mA, was applied along the principal axis of the whisker. Critical currents were typically less than 100 mA. No further changes were observed for currents above the critical current up to 750 mA, which was as high as was convenient. After finding the critical currents, the magnetic response

was studied for at least one current less than critical while the dc external field was changed. Then this sequence was repeated with higher applied currents; typically, 20, 25, 75, 150, 200, 400, and 600 mA. Most measurements were of out-of-phase signals which were sensitive to internal domain structures. Also, a few measurements were done for in-phase signals. Throughout the ac susceptibility measurements, the ac driving field was fixed, typically with a frequency of 700 Hz. Because the temperature variation did not affect the ac susceptibility, it was not necessary to use the oil bath as was done for resistance measurements.

### **3.4 Combined Susceptibility and Resistance Measurements**

Many <100> samples were tested to identify the existence of the Landau structure before adding copper leads for doing the dc resistance measurements. The typical magnetic response of the Landau structure frequently disappeared after silver paint adhesive was used to bond copper leads on the side of the iron whisker. The reason was that the contacts caused stresses strong enough to change the structure as the adhesive solidified. After this problem was recognized, GaIn was used to solder fine copper wires on the sides of the whiskers. The disadvantage of using the GaIn solder was that the contact was easily broken. Even though stress was caused by silver paint on the ends, it was not big enough to change the Landau structure of a whisker with typical dimensions, 200  $\mu\text{m}$  x 200  $\mu\text{m}$  x 2 cm.

Both the ac susceptibility and the resistance measurements were affected by the domain structure inside a whisker so that we tried to measure them at the same time. But the sample was inevitably damaged in handling. The limited space made it too difficult so we decided to measure them sequentially. First, the ac susceptibility measurement with zero current was done to identify the existence of the Landau domain structure. Samples with Landau structures were chosen for the dc resistance measurements. After the resistance measurements were complete, the ac susceptibility experiment at zero current was repeated to check whether the whisker was damaged or not. Then the ac susceptibility measurements were done while applying a sequence of currents and varying the external field. After the ac susceptibility experiments with applied currents were complete, the ac susceptibility measurements were again repeated with zero current to check the domain structure. All experiments were done at room temperature, using an oil bath for the resistance measurements, but not for the ac susceptibility measurements.

# Chapter 4

## Experimental Results and Their Interpretations

The purposes of the dc resistance and the ac susceptibility experiments are to understand the domain structure and the magnetization processes inside a <100> iron whisker while currents and/or external fields are applied along the principal axis. The results of the measurements are presented in this chapter. Likely domain configurations can be deduced from the measurements corresponding to applied currents and/or external fields. Simple models are suggested to explain magnetic responses and the domain configurations which were deduced from experimental data. A model for eddy current loss, suggested to explain the ac susceptibility results, is presented in this chapter. Most of the effects of currents and/or external fields are explicable in terms of the sequence of deduced domain configurations and the model discussed here. An exception is the response in low fields which remains to be explained.

### 4.1 Results of Resistance Measurements

The relative change in the resistivity is calculated as

$$\frac{\Delta\rho'}{\rho_{sat.}} = \frac{\Delta R'}{R_{sat.[100]}} = \frac{(R' - R_{sat.[100]})}{R_{sat.[100]}} \quad \text{Eq. 4.1.1}$$

where  $\rho_{sat.}$  and  $R_{sat.[100]}$  are the average resistivity and resistance with a strong external field, respectively, and  $R'$  is the resistance of the whisker when a desired measuring field is applied. For the convenience, the sign of the resistance change,  $\Delta R'$ , is chosen opposite to the sign of Eq. 2.4.5a. The temperature coefficient of pure iron wire<sup>47</sup> at 20 °C is 0.00651 °C<sup>-1</sup>. If the temperature varies by 0.1 °C during the measurement, the effect of the temperature variation can not be distinguished from that of domain movements. The temperature drifts were monitored using a copper wire as a resistance thermometer. All whisker resistances were corrected for temperature drifts. The resistance of the whisker was measured in a strong external field before and after measurement of  $R'$  in the desired dc field. This also helped to reduce the effect of temperature drift. The average resistance,  $R_{sat.[100]}$ , in Eq. 4.1.1 is the average of the two measured resistances in the strong field.

#### 4.1.1 Damaged Samples

In the early stages of the experiments, no attention was paid to whether or not the Landau structures were obtainable in samples used for resistance measurements, that is, the samples having square cross sections, presumably  $\langle 100 \rangle$  whiskers, were used for the resistance measurements without checking their domain structures by ac susceptibility measurements, as was done later. Even though they probably had Landau structures initially, the process of handling the whiskers gave rise to strains which, due to the magnetostriction, produced undesirable domain structures. The

resistance measurements done with damaged and undamaged samples showed different behaviors. Also, in the early stages a three and half digit nanovoltmeter was used to measure the voltage across a whisker; this was insufficient precision for our purposes. The results in Fig. 14 show that the resistance depends on applied currents and external fields. The resistance decreased when the applied current was increased. The lowest resistivity of the damaged whisker at zero field was at the highest current.

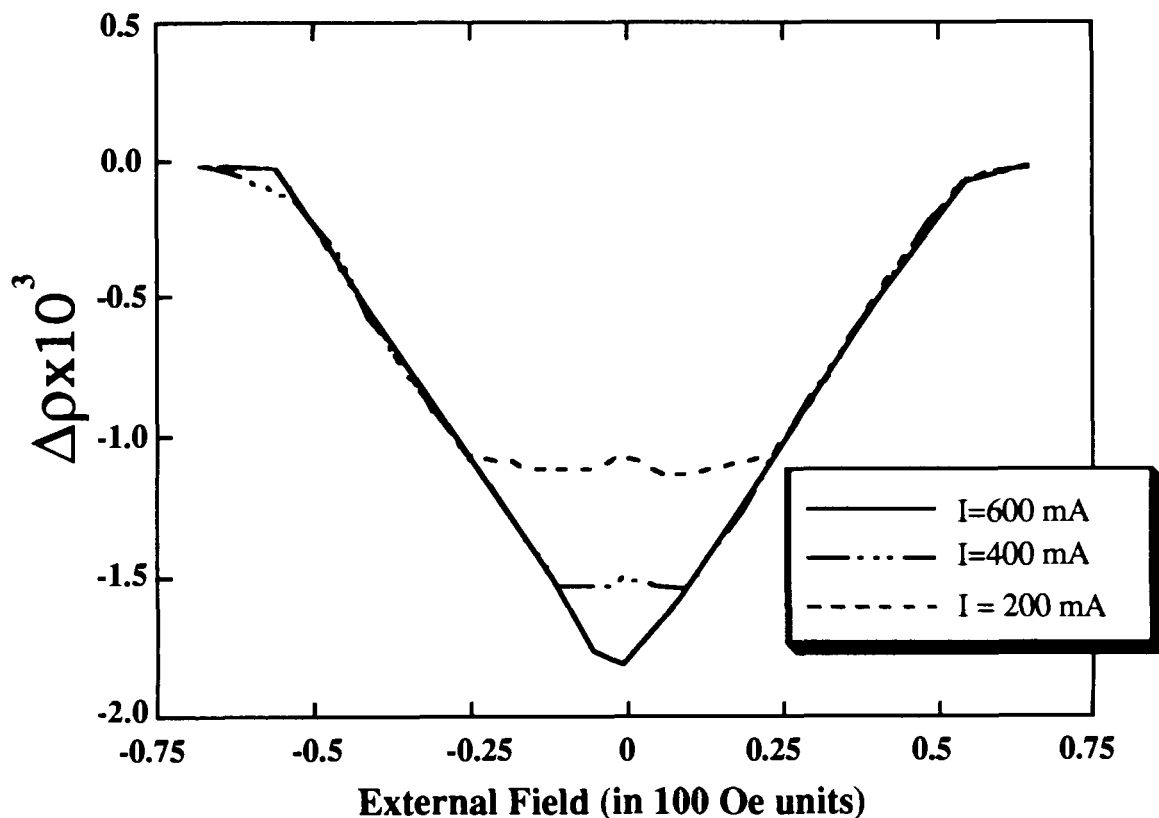


Fig. 14. Magnetoresistance of a damaged  $\langle 100 \rangle$  iron whisker, measured with a voltmeter with insufficient resolution.

The changes in the resistance with current and field could be explained with the relation among the resistance, domain

orientations, and the direction of an applied current. As the lowest resistivity is obtained when the direction of magnetization in all of the domains is perpendicular to the direction of the applied current, the domain structure suggested by Shumate *et al.*, Fig 2(a), is consistent with the resistance changes seen in the early measurements. When insufficient current is passed through the whisker, the resistance is not decreased to the minimum. This is explained if the Landau structure is transformed to the one suggested by Shumate *et al.* If the applied current is sufficiently large, domains perpendicular to the current nucleate and propagate in towards the center of the whisker. These domains make the resistance decrease. If the applied current were not large enough to fully collapse the central core, an external field would first displace the 180° wall to one side at the center and then expand the central domain at the expense of those perpendicular to the current. The displacement of the 180° wall would not change the resistance. The flat regions near zero field for lower currents and the change in the relative resistivity in Fig. 14 can be explained with the above interpretation. But these results are not consistent with later results obtained with samples that are sufficiently strain free to show Landau structures. The reasons for the inconsistency are the lack of measuring accuracy in the early experiments and the damaged domain structures in whiskers used to obtain the early results. Furthermore, the above model of the Shumate structure will be shown to be inconsistent with ac susceptibility results on unstrained samples.



### 4.1.2 <100> Whiskers with Landau Structures

In later experiments, GaIn solder was used to connect the copper lead wires to the sides of a whisker. This technique usually preserved the Landau domain structure, as confirmed by ac susceptibility measurements. Precise resistance measurements on whiskers with Landau domain structures presented in Fig. 15(a) show the changes in the relative resistivity of a <100> whisker as functions of external field and current. At all currents the sequence of resistance measurements was from high field to zero field. When

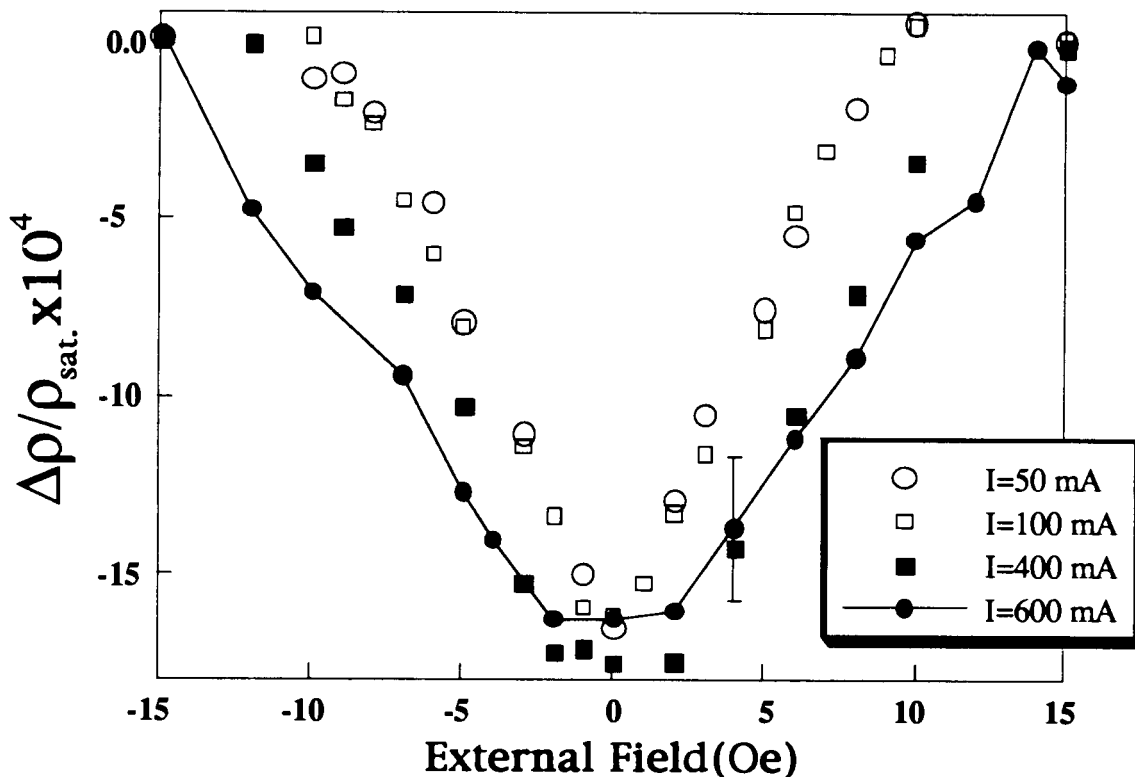


Fig. 15(a). Change in relative resistivity for a <100> whisker with different currents.

a current larger than critical was passed along the axis of the whisker, the resistance decreased to the minimum in zero external

field. All currents in Fig. 15(a) were greater than critical. The critical current which makes a  $\langle 100 \rangle$  whisker transform from its Landau structure to the one shown in Fig. 2(b) can be found more sensitively by using ac susceptibility measurements as explained in the next section. The difference of the longitudinal resistivity between zero field and high fields was a decrease of  $\sim 0.17\%$ . According to Tatsumoto,<sup>6</sup> when an iron crystal has the domain configuration as in Fig. 2(b), the change in the relative resistivity is  $0.18\%$ . This behavior was observed with several different whiskers having Landau structures in the absence of current.

The results for another whisker are shown in Fig. 15(b) where all applied currents are larger than critical. For all currents, the minimum resistance is again obtained with zero field. A stronger external field was required to change the resistance of a  $\langle 100 \rangle$  whisker in the presence of a larger current. For currents greater than about 50 mA there is a range of low fields for which the resistance change is slight. However, there appear to be inconsistencies in Fig. 15(b); in particular, some points look strange unless the large uncertainty in the measurement is considered. Estimates of the uncertainties in the data show that it would be difficult to extract the dependence of  $\Delta\rho'$  on the external field for various currents with sufficient accuracy to compare with the simple theoretical prediction that will be discussed in Section 4.5. The data in Figs. 15(a) and (b) are sufficient to show that larger external fields are needed to saturate the whisker when larger currents are applied. More detailed comparison of experiment and theory relies on the ac susceptibility measurements.

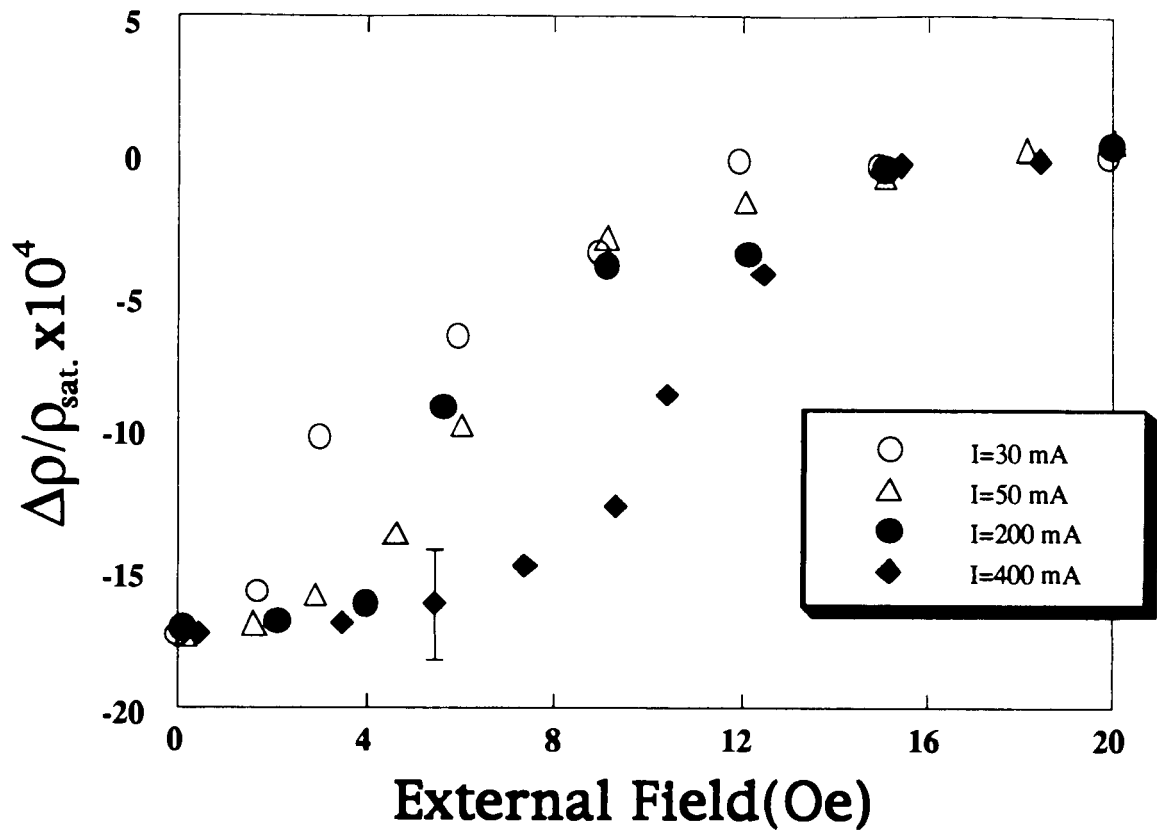


Fig. 15(b). Same as Fig. 15(a) for another  $\langle 100 \rangle$  whisker.

## 4.2 Results of AC Susceptibility Measurements

The ac susceptibility measurements were used to test all later samples for the Landau domain structure before and after the measurements with applied currents, as mentioned in Sections 3.3 and 3.4. All the ac susceptibility measurements were done at a frequency of 700 Hz for the driving field, unless specifically noted. The in-phase and out-of-phase responses while passing current through a  $\langle 100 \rangle$  whisker are presented in this section. It is difficult to explain the ac susceptibility with lower applied current. The ac

susceptibility results with higher current are explained in detail to deduce domain structures corresponding to external fields and currents.

### 4.2.1 Critical Current Measurements

The results of ac susceptibility measurements on two whiskers with zero applied dc field and with varying current are shown in Fig. 16. In the sense that the effect of current on magnetization is being investigated in zero field, this experiment is similar to the one by Berthe *et al.*<sup>4</sup>

In Fig. 16(a) the ac susceptibility is symmetrical in current. When the current was changed from a negative high current to an opposite high current, two major jumps of the ac signal across the pick-up coil were observed at applied currents of -9.8 mA and 48 mA. When the direction of current change was reversed the jumps occurred at 9 mA and -43 mA. As discussed by Berthe *et al.*, these currents transform one stable domain structure to another. The discontinuous changes at 48 mA and -43 mA correspond to the transformation from the Landau structure to the one responding to the field from the current. The transformed structure is likely to be as shown in Fig. 2(b). These currents are called "critical currents." The critical current is defined as the current that transforms the Landau structure into the rotated structure as shown in Fig. 2(b). The jumps at -9.8 mA and 9 mA, can be explained by the opposite transformation. The out-of-phase signal is high for the Landau structure and zero for the structure produced by the current. Even

though larger currents were applied, up to 750 mA, no other sudden change in the ac signal was observed. The results of Fig. 16(a) indicate that the high susceptibility is achieved in two stages. The first stage of slightly lower loss would correspond to an intermediate structure (likely the Coleman structure) and the second stage of higher loss to the Landau structure. The critical currents did not always have the same values for a given whisker; i.e., they depended on the history of the field cycles. These currents were also dependent on the thicknesses of the various  $\langle 100 \rangle$  whiskers.

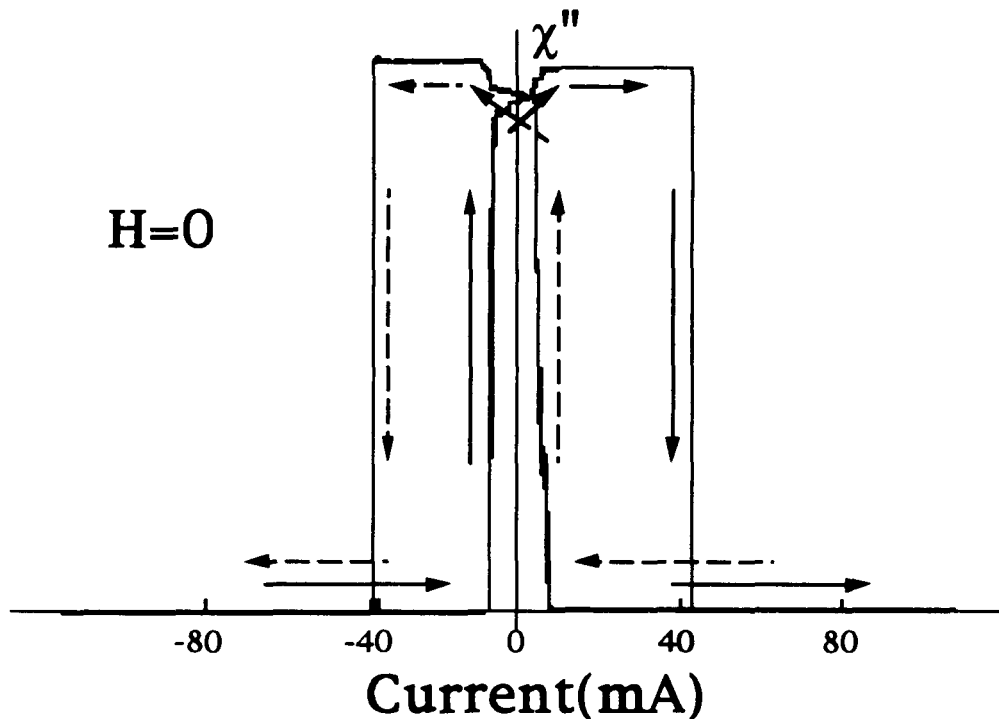


Fig. 16(a). Magnetic susceptibility while varying current without external field. This whisker shows symmetric behavior.

The results in Fig. 16(a) show a symmetrical behavior but this was not always the case. One of the unsymmetrical results is shown in Fig. 16(b). Such unbalanced behavior might be due to surface

defects which make the nucleation of magnetic domains easier in one direction than in the other.

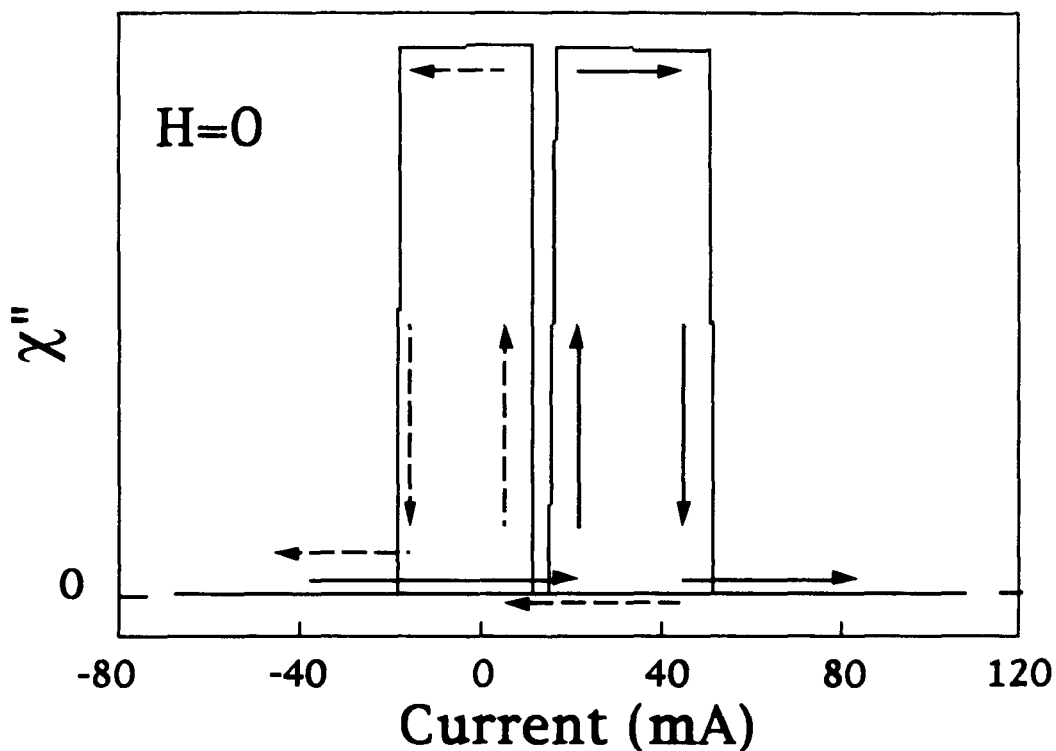


Fig. 16(b). Same as Fig. 16(a) for a whisker that shows asymmetric behavior.

#### 4.2.2. Effect of Currents on AC Susceptibility

The out-of-phase components of the ac susceptibility are presented in Fig. 17 as a function of dc external field for a sequence of fixed currents. For currents from zero to the critical current the susceptibility displays the behavior shown in Fig. 17(a); the current has no evident effect on the shape of the response. As the applied current increases above the critical current, Figs. 17(b) to (f), the

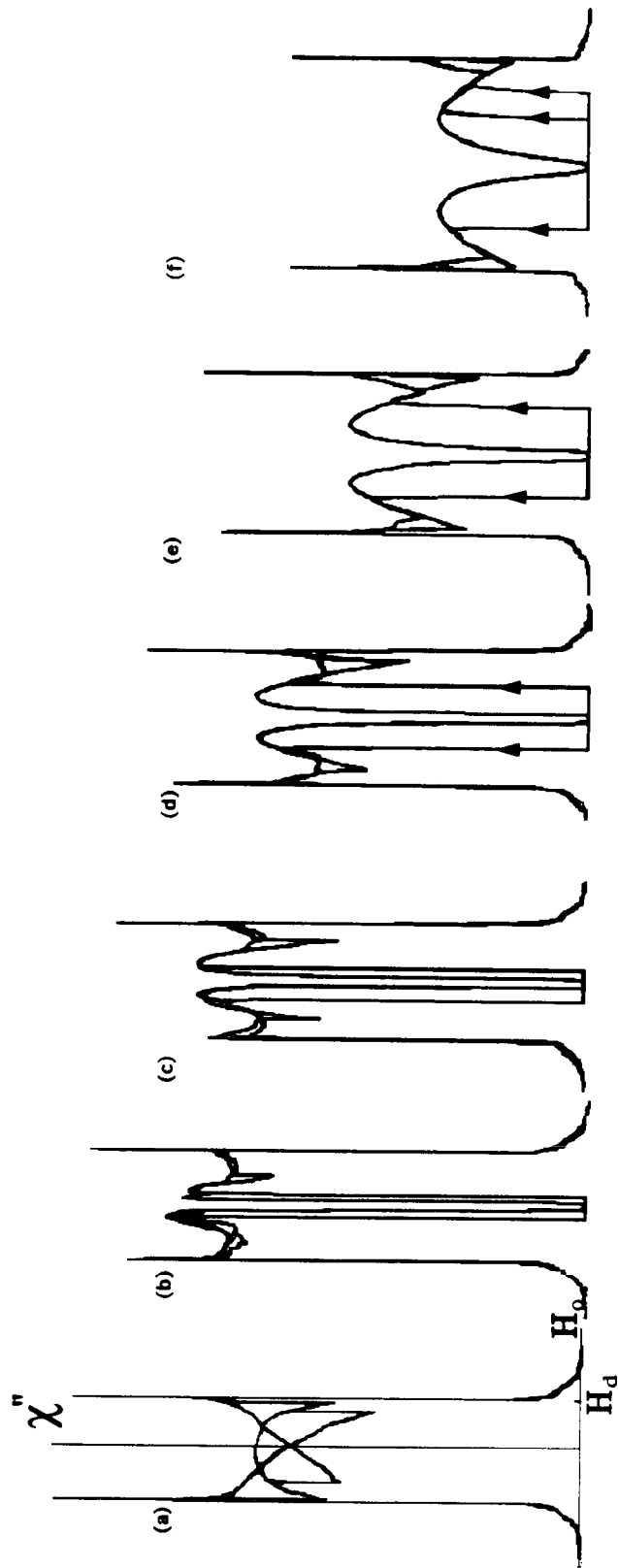


Fig. 17. AC out-of-phase susceptibility for a  $\langle 100 \rangle$  whisker as a function of external dc field for different currents, a)  $I=20$  mA, b)  $I=75$  mA, c)  $I=150$  mA, d)  $I=200$  mA, e)  $I=400$  mA, and f)  $I=600$  mA.  
 $H_d (I=20 \text{ mA}) = \pm 150\text{e}$ .

out-of-phase signals respond differently from that with zero current; the whisker does not respond to the ac driving field near a zero external field when the applied current is larger than critical. At the critical current, the Landau structure transforms to the one shown in Fig. 2(b). As the field, starting from high field, approaches zero from either direction, the out-of-phase signal disappears at a field that does not depend strongly on the applied current; that is, when the field magnitude is decreased toward zero, the response goes to zero before the field has reached zero. As the field continues to change through zero, the ac response remains zero to a larger magnitude field than that at which it originally collapsed. The difference in the magnitude of these fields bounding the zero response region increases with increasing applied current. In the zero response field region, the ac susceptibility is reversible on returning towards the original field direction. As the current increases, the magnitude of the out-of-phase signal in the non-zero response field region decreases and the departure field becomes larger.

Fig. 18 shows the ac magnetic responses for whiskers sufficiently strained that the Landau domain structure was suppressed. The ac magnetic responses are different from the ones measured with a  $\langle 100 \rangle$  whisker having the Landau domain structure. For the whisker having the proper domain structure, the out-of-phase susceptibility disappears when the applied current is larger than critical. But the ac response of the whisker without Landau structure vanishes only for the largest current.

The ac magnetic responses with low currents in Fig. 17 can not be understood easily. Only the ac susceptibility with  $I=600$  mA,



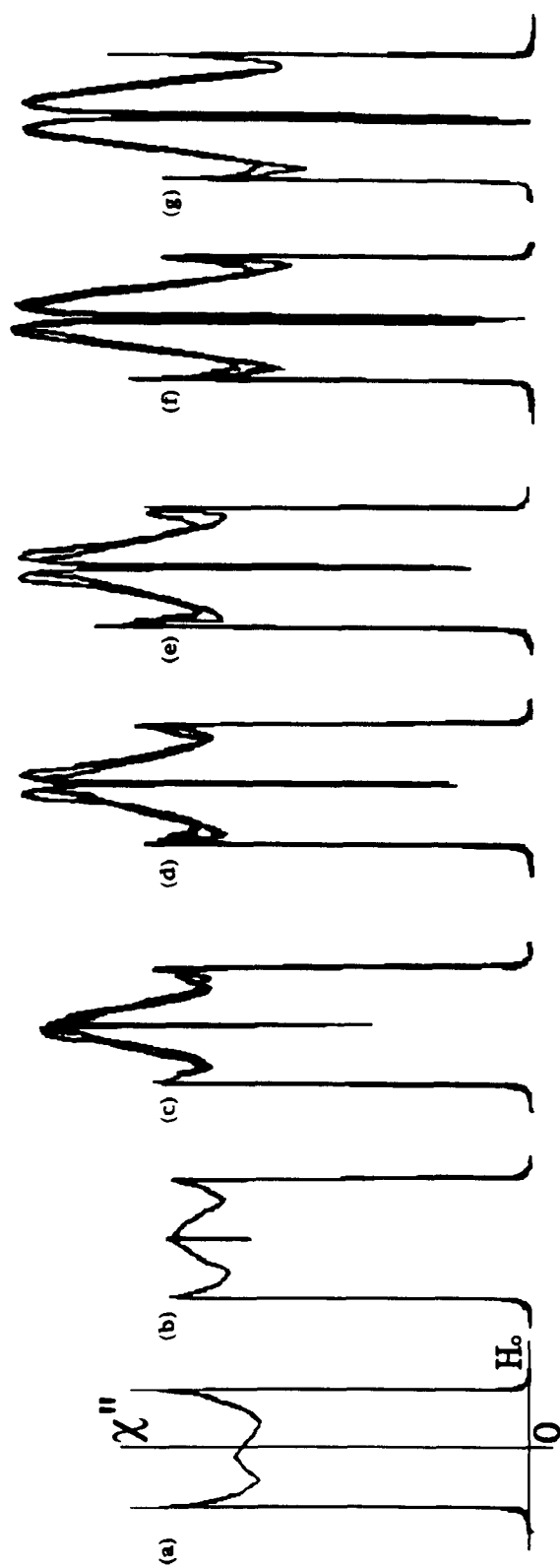


Fig. 18. Ac out-of-phase responses for a damaged  $\langle 100 \rangle$  whisker while applying different currents, a)  $I=0$  mA, b)  $I=50$  mA, c)  $I=150$  mA, d)  $I=200$  mA, e)  $I=300$  mA, f)  $I=400$  mA, and g)  $I=600$  mA.

Fig. 17(f), is explained in this thesis. To understand this magnetic response, it is necessary to explain the out-of-phase component of the ac signal in detail. Four fields are introduced here to make it easier to discuss the magnetic response; the nucleation field,  $H_n$ , and the departure field,  $H_d$ , above which the center of the whisker is saturated; the collapse field,  $H_c$ , below which the susceptibility is minimal because the transverse domain structure dominates; and the renucleation field,  $H_r$ , above which a reversed magnetization pattern in the center of the central cross section is formed because of nucleation elsewhere in the whisker.

The magnetic response of Fig. 17(f) is shown schematically in Fig. 19. The points described as (a) to (l) refer to Fig. 19. For  $|H_o| > H_d$ , the response in the central cross section is negligible because the magnetization is saturated, but the changing magnetization elsewhere changes the demagnetizing field which is picked up by the detection coil. This accounts for the tails for fields with magnitudes greater than  $H_d$ . As the amplitude of the magnetic field decreases from point (a) to point (c), the out-of-phase signal shows a large discontinuous increase at the nucleation field,  $H_n$ , close to the departure field,  $H_d$ . At fields closer to zero than  $H_d$  and up to point (c), the signal decreases rapidly as the nucleated domain wall length in the central cross section increases. Until the external field passes through point (c), the magnetic response is reversible from points (b) to (c). On passing through point (c) there is an irreversible change in which the slope of the ac response is discontinuous even though its value changes little. The section labeled from points (c) to (f) is reversible, and the range of reversibility extends back to point (d).

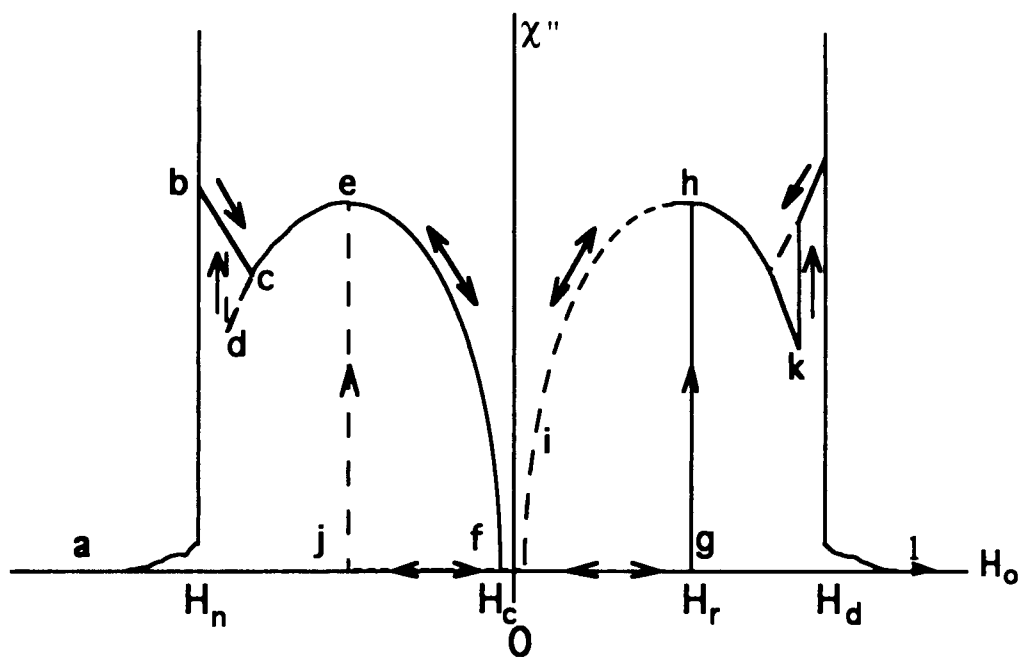


Fig. 19. Schematic diagram for out-of-phase ac susceptibility with a large current. The solid line is for changing the field from saturation to departure in the one direction. The dashed line is for the opposite direction. Double headed arrows indicate regions of reversible behavior.

If the field decreases through point (d), there is an irreversible jump at point (d) back into the reversible section from points (b) to (c). As the external field approaches zero, (e) to (f), the out-of-phase signal becomes negligible at the collapse field,  $H_c$ . As the external field increases in the positive direction toward point (g), the magnetic response remains negligible. If the external field does not exceed point (g) and it is now reversed, the magnetic response follows from (g), to (f), to (e), to (c), to (d) reversibly. When the field exceeds point (g), the response shows a large jump at point (h). The external field at point (g), defined as the renucleation field,  $H_r$ , depends on the applied current and the history of the field cycles. On further

increase in external field above  $H_r$ , the response traces out the reversible section (h) to (k). Again there is a larger reversible region from (k) to (h) to (i) to (f) to (j), where point (j) is the renucleation field in the case of fields being changed from positive to negative. For fields greater than at point (k) a section equivalent to points (b) to (c) is obtained until the departure field,  $H_d$ , is reached at which the center of the whisker is saturated.

The above description applies to the experiment shown in Fig. 17(f). In the Fig. 17 experiment, the driving field was the standard 700 Hz. This same experiment was repeated with a 200 Hz driving field. No big differences in response were observed except for the smaller intensities of the response signals.

Fig. 20 shows the in-phase and out-of-phase components of the ac signals for two different whiskers. Typically, the intensity of the in-phase signal was about 7 times larger than that of the out-of-phase signal. The out-of-phase responses here are similar to the schematic diagram of Fig. 19 except for the region near zero field. In Fig. 20(a) the in-phase signal is constant over a range of applied fields where the susceptibility is sufficiently high that the response is completely determined by demagnetizing fields; see region (a) in Fig. 20(a), 2). At sufficiently low fields the in-phase susceptibility decreases sufficiently that it determines the response rather than the demagnetizing fields; see region (b) in Fig. 20(a), 2). There is a range of fields in which the susceptibility is larger than that corresponding to infinite internal susceptibility; see region (c) in Fig. 20(a), 2). This is a range where the interior structure would be unstable if it were not for the stabilizing effect of the demagnetizing field. The in-phase

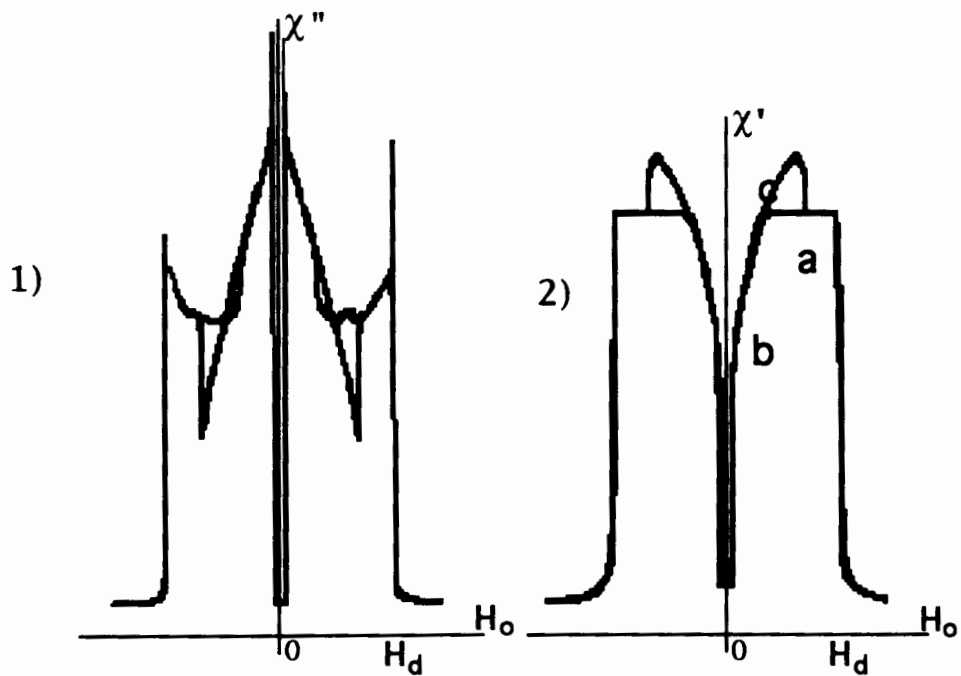


Fig. 20(a). 1) Out-of-phase and 2) in-phase signals measured with a current ( $I=150$  mA) and driving field of frequency 700 Hz.  $H_d = 15$  Oe. The lower current enhances the instabilities at low fields.

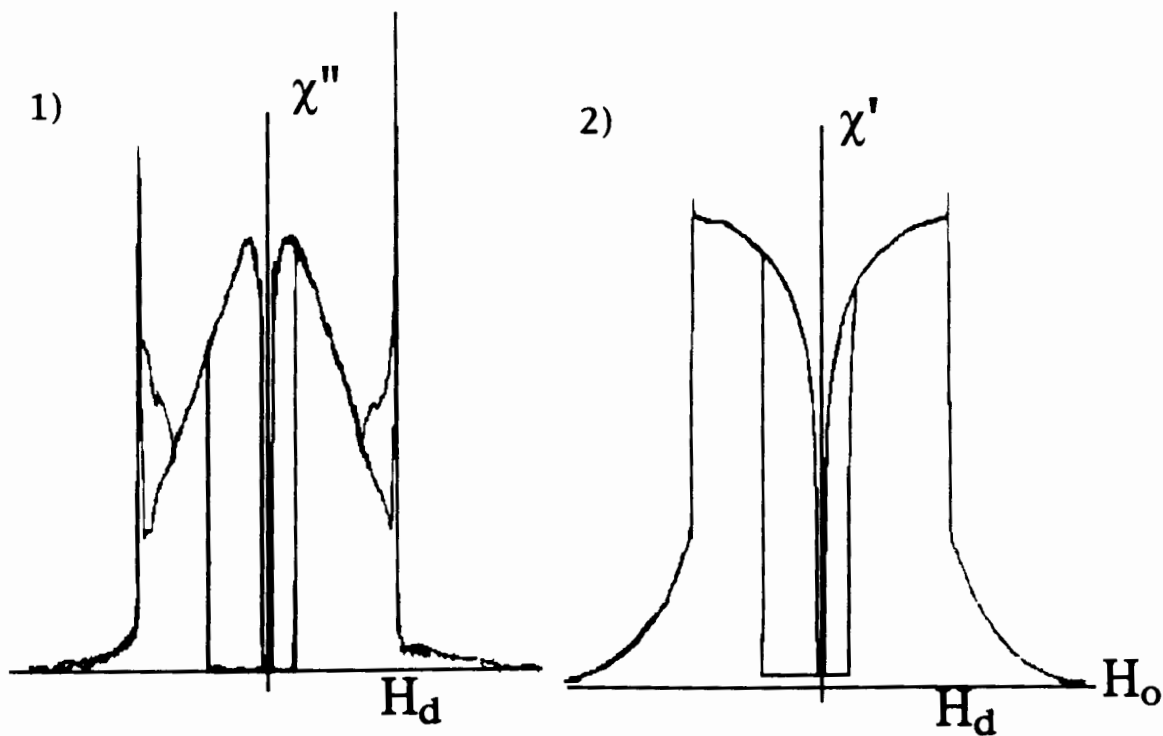


Fig. 20(b). 1) Out-of-phase and 2) in-phase signal with current 300 mA and driving field frequency 500 Hz.

signal does not completely disappear at near zero fields. The discontinuous changes in in-phase and out-of-phase signals occur at the same external fields.

Fig. 20(b) shows the out-of-phase and in-phase components of the ac signal with a current of 300 mA for a different  $\langle 100 \rangle$  whisker. The driving-field frequency was 500 Hz. The difference between Figs. 20(a) and (b) are most likely due to the larger current in Fig. 20(b) suppressing the instabilities seen in region (c) of Fig. 20(a).

### **4.3 Models for the Stable Structures**

A simple domain structure can be deduced from ac susceptibility measurements with varying current. When an external field is applied along the principal axis of a  $\langle 100 \rangle$  whisker, the change in the domain configuration can be deduced from dc resistance and ac susceptibility measurements. During the magnetic processes, five energy terms compete with each other to determine a stable domain structure corresponding to each current and external field. In this section, the roles of these energies are explained with simplified models. The ac susceptibility at zero frequency is explained in this section.

#### **4.3.1 Model for a Fixed Structure**

Simple domain structures are suggested here as possible explanations for the experimental results of the dc resistance and the ac susceptibility measurements. The contribution of each energy

term to the total energy is discussed. One of the suggested domain structures is shown in Fig. 2(b). It has only  $90^\circ$  domain walls lying in  $\{110\}$  planes. Most of the magnetization, except in the walls, lies in the plane of the cross section and is directed along easy axes of the whisker. The magnetization at the center must be perpendicular to the plane to avoid a singularity in the exchange energy. The magnetization at each corner of the cross section also must be normal to the plane. This is shown later in Fig. 31 in Chapter 5. The out of plane  $y$ -component of the magnetization will produce a net magnetization flux through the central cross section. By Gauss's theorem, this means that there must be magnetic charges toward the ends of the whisker. These charges will go to the surfaces away from the central cross section, where it is zero by symmetry. The domain configuration is built up without volume charge as this lowers the contribution of the volume charges to the magnetostatic energy. The completely volume charge free structure is only an approximation, nevertheless an adequate one.

The total energy of the system consists of the wall energy,  $E_w$ , which includes the exchange energy,  $E_{ex}$ , and the anisotropy energy,  $E_K$ , the field energy due to the applied current,  $E_I$ , the magnetostatic self-energy,  $E_D$ , and the energy from an applied field,  $E_H$ . Thicknesses of domain walls are determined by the competition among these energies. The anisotropy and the magnetostatic energies, and the energy from the applied current, favor thinner domain walls. On the other hand, the exchange energy favors thicker walls. The effect of an applied field depends on its direction with respect to the direction of the magnetization in the central domain.

consider only the case where the direction of the net magnetization of the central cross section is the same as the direction of the external field. To find the details of the domain configuration corresponding to an applied current, the total energy of the central cross section per unit length,

$$\bar{E}_{tot} = \bar{E}_w + \bar{E}_D + \bar{E}_I + \bar{E}_H,$$

where  $\bar{E}_w = \bar{E}_{ex} + \bar{E}_K$  must be minimized with respect to parameters of the model. When the total energy is minimized, the thickness of the domain walls is determined for a specific current. The  $E_{ex}$  and  $E_K$  terms dominate for the domain configuration of Fig. 2(b) and thus the configuration will not change significantly with current or external field. All that can happen is that a different domain configuration with a lower energy could be nucleated elsewhere for sufficiently changed current.

### 4.3.2. Model for a Variable Structure

The magnetic response as a function of the external field is difficult to explain with the suggested domain configuration of Fig. 2(b). Another domain structure is suggested to overcome this problem; it is the one shown already in Fig. 2(c). It may have an energy lower than the structure of Fig. 2(b) because of lower wall energy. This is compensated for partly by the increased demagnetizing energy,  $E_D$ , when some of the magnetization lies along the  $y$ -axis that is the principal axis of the whisker. By Gauss Theorem, the  $y$ -component of the magnetization requires magnetic



surface charge densities that increase towards the ends of the whisker as the y-component of the magnetization decreases along the whisker. These charges generate a demagnetizing field. There is also more wall area with the new configuration and competition between the wall energies of the two types of  $90^\circ$  walls, i.e., the  $90^\circ$  walls lying in the (110) plane is called as a (110)  $90^\circ$  wall and the  $90^\circ$  wall lying in the (100) plane is as a (100)  $90^\circ$  wall.

With the configuration of Fig. 2(c), as the external field increases, more surface charges on the whisker are produced which are proportional to the area of the central domain. These surface charges produce a demagnetizing field which opposes the external field inside the whisker. When the external field is larger than the collapse field, we expect that the competition among energies makes the central domain larger if the field is in the same direction as the magnetization of the central domain. The external field should change the width of the central domain, but have little effect on the structure of the (110)  $90^\circ$  walls which are determined by competition between exchange and anisotropy energies.

The total energy can be found after introducing several parameters that describe the new domain configuration. The minimization of the total energy will determine the area of the central domain, and the thicknesses of the (110)  $90^\circ$  wall and the (100)  $90^\circ$  wall.

Figs. 21(a) and (b) show the detailed diagram for the proposed domain structure in the central cross section of the whisker.  $M_1$ ,  $M_2$ , and  $M_3$  are the average y-components of the magnetization for the specific areas, as shown in Fig. 21(b).  $M_1$  is the average y-component

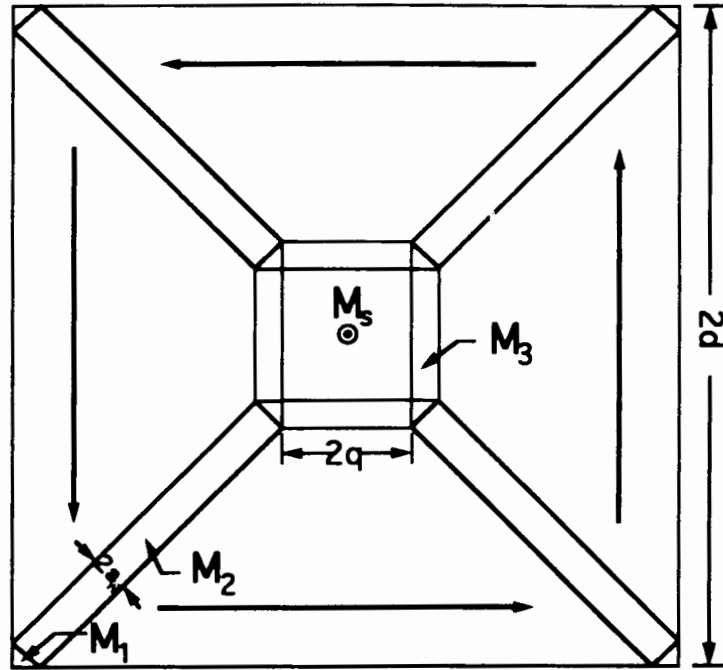


Fig. 21 (a) Schematic diagram for calculating the energy of a  $\langle 100 \rangle$  whisker.

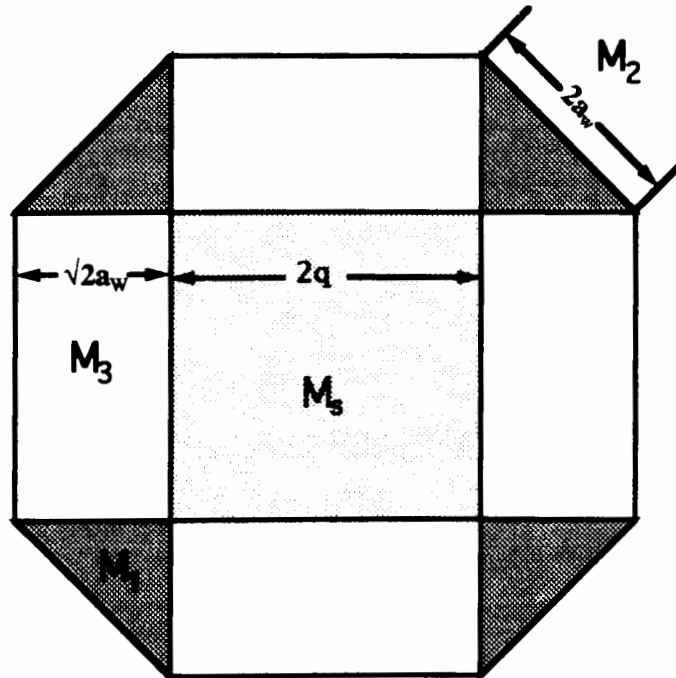


Fig. 21(b) Detailed diagram at the central domain.

of the magnetization at a corner of the cross section,  $M_2$  is that across a (110) 90° wall, and  $M_3$  is that across a (100) 90° wall. When the external field,  $H_o$ , is applied along the  $y$ -direction, the area of the central domain varies. In order to explain the magnetization process at the central cross section, it is convenient to introduce a reduced length,  $x = \frac{q}{d}$ , where the thickness of the whisker is  $2d$  and that of the central domain is  $2q$ . From Fig. 21(a), the average  $y$ -component of the magnetization from the central cross section is written as

$$M_{y,s}(x) \equiv \frac{\int_{A_s} M_y dS}{A_s} = (x^2 + A(a_w)x + C(a_w))M_s \quad \text{Eq. 4.3.1}$$

where  $A(a_w) = \sqrt{2} \frac{a_w}{d} \frac{(2M_3 - M_2)}{M_s}$  and  $C(a_w) = \frac{2(M_1(\frac{a_w}{d})^2 + M_2 \frac{a_w}{d}(\sqrt{2} - 2\frac{a_w}{d}))}{M_s}$ .

$A(a_w)xM_s$  describes the magnetization of domain wall length and  $C(a_w)M_s$  is the residual magnetization of the cross section.  $2a_w$  is a thickness of a (110) 90° domain wall.  $M_{y,s}(x)$  becomes a function of the reduced length,  $x$ .

The magnetization for  $M_1$  is along the  $y$ -direction at the corner of the cross section, and  $M_{y,s}(x) = \frac{1}{\sqrt{2}}M_s$  at the center of the interface between the area for  $M_1$  and a (110) 90° wall and  $M_{y,s}(x) = 0$  at the edges of the interface. The  $y$ -component of the magnetization for  $M_2$  increases from zero to  $1/\sqrt{2}M_s$  and then to zero while the magnetization is across the (110) 90° wall. The magnetization for  $M_3$  increases from zero to  $M_s$  while crossing the (100) 90° wall.  $M_1$ ,  $M_2$ , and  $M_3$  can be calculated with the assumption that the average  $y$ -component of the magnetization in the domain wall behaves like a *sech*-function. The average magnetization is  $M_1 = 0.77M_s$ ,  $M_2 = 0.46M_s$ ,

and  $M_3 = 0.65M_s$ . With our model,  $A(a_w)M_s = 0.302 \text{ emu/cm}^3$ , and  $C(a_w)M_s = 0.652 \text{ emu/cm}^3$  for  $2a_w = 6 \times 10^{-2} \mu\text{m}$  and  $2d = 200 \mu\text{m}$ .

When the external field,  $H_o$ , is applied along the  $y$ -direction, the energy from the external field and the demagnetizing energy per unit length are expressed as

$$\bar{E}_H + \bar{E}_D = -H_o M_{y,s}(x) A_s + \frac{1}{2} 4\pi D M_{y,s}^2(x) A_s \quad \text{Eq. 4.3.2}$$

where  $A_s$  is the cross section of the sample and  $D$  is the demagnetizing factor.

When the whisker has the central domain with the cross section,  $4q^2$ , as shown in Fig. 21(a), the total length of (100)  $90^\circ$  walls is  $8q$  and that of (110)  $90^\circ$  walls is  $4\sqrt{2}(d-q)$ . The total wall energy per unit length is  $4\sqrt{2}(d-q)\sigma_a + 8q\sigma_a/\sqrt{3}$  where  $2d$  is the width of the whisker and  $\sigma_a$  is the energy density of a (110)  $90^\circ$  domain wall. The total wall energy is lowered if the central region expands. But the demagnetizing field and the field from the current oppose the outward motion of the walls. The balance of the wall energy opposed by both the energy from the current and the demagnetizing energy will be shown to result in a small central domain even in the absence of an external field. This occurs because the sign of the changing wall energy is negative.

When the whisker has the above domain structure, the total wall energy per unit length can be expressed as

$$\bar{E}_w = \bar{E}_{w_o} + 8x\left(\frac{-\sigma_a}{\sqrt{2}} + \frac{\sigma_a}{\sqrt{3}}\right)d = \bar{E}_{w_o} - xd|\sigma_1| \quad \text{Eq. 4.3.3}$$

where  $\bar{E}_{w_o} = 4\sqrt{2}d\sigma_a$  is the wall energy per unit length with no central core, and  $|\sigma_1| = 8\left(\frac{1}{\sqrt{2}} - \frac{1}{\sqrt{3}}\right)\sigma_a$ .

The field from an applied current,  $H_I$ , derived in Section 2.5, is approximated as increasing linearly with distance from the center. The energy from the current is expressed as  $E_I = -\int_V \vec{H}_I \cdot \vec{M} d\tau$ ; i.e., when the magnetization lies along the field from the current, the energy is minimum. As the central domain becomes large, the energy increases. The energy from the current is approximated as it is mainly from the growth of the central core, proportional to  $4q^2$ .

When the central domain has the area,  $4q^2 = 4x^2d^2$ , the energy from the current per unit length is approximated as

$$\bar{E}_I = \bar{E}_{I_0} + \frac{4\sqrt{\pi}Id}{15} x^3 M_s \quad \text{Eq. 4.3.4}$$

where  $\bar{E}_{I_0}$  is the energy from the current per unit length with no central domain.

The total energy per unit length is

$$\bar{E}_{tot} = \bar{E}_{tot_0} + \frac{4\sqrt{\pi}Id}{15} x^3 M_s - H_o M_{y,s}(x) A_s + \frac{1}{2} 4\pi D M_{y,s}^2(x) A_s - x |\sigma_1| d \quad \text{Eq. 4.3.5}$$

The energy from the current and the demagnetizing energy tend to keep the central domain small. On the other hand, the energy from the applied field and the wall energy tend to expand the central domain. The size of the central domain, in the case that there is no external field, is determined mainly by the competition between the demagnetizing energy and the wall energy. In this case the central domain is expected to be small, as shown in Fig. 2(b). For zero applied current, the size of the central domain can be found approximately by minimizing the total energy;

$$\frac{\partial \bar{E}_{tot}}{\partial x} \approx \frac{\partial (\bar{E}_w + \bar{E}_D)}{\partial x} = -|\sigma_1|d + 4\pi D M_s A_s M_{y,s}(x)(2x + A(a_w)) = 0.$$

The size of the central domain depends on the thickness of the whisker because the residual magnetization,  $C(a_w)M_s$ , becomes larger as the cross section of the whisker increases. If we use the values  $|\sigma_1| = 1.3 \text{ erg/cm}^2$ ,  $4\pi D = 0.00577$  for  $2d/L = 1/100$ ,  $M_s = 1715 \text{ emu/cm}^3$ , and  $2a_w = 6 \times 10^{-2} \text{ }\mu\text{m}$ , the relation between the thickness of the whisker and the size of the hole is approximately  $2d \propto (2q)^{3/2}$ ; e.g., for  $2d = 200 \text{ }\mu\text{m}$ ,  $2q = 19 \text{ }\mu\text{m}$ . The applied current makes the central domain smaller. The full relation will be followed in this section.

The external field makes the central domain grow or shrink depending on the direction of the field. The full relation among the external field, the current, and the size of the central domain can be found by the minimization of the total energy with respect to the parameter,  $x$ , as

$$\begin{aligned} \frac{\partial E_{tot}(x)}{\partial x} &= \frac{4\sqrt{\pi}Id}{5} x^2 M_s - H_o(2x + A(a_w))M_s A_s - |\sigma_1|d \\ &+ 4\pi D(2x + A(a_w))(x^2 + A(a_w)x + C(a_w))M_s^2 A_s = 0. \end{aligned}$$

The effective external field is

$$H_o = 4\pi D(x^2 + A(a_w)x + C(a_w))M_s + \frac{-d|\sigma_1|}{(2x + A(a_w))A_s M_s} + \frac{4\sqrt{\pi}Id x^2}{5(2x + A(a_w))A_s}.$$

Eq. 4.3.6

Eq. 4.3.6 shows the external field inside a magnetic material is reduced by the demagnetizing field,  $4\pi D(x^2 + A(a_w)x + C(a_w))M_s$ , the effective wall field,  $\frac{-d|\sigma_1|}{(2x + A(a_w))A_s M_s}$ , and the effective field from the current,  $\frac{4\sqrt{\pi}Id x^2}{5(2x + A(a_w))A_s}$ .

To demonstrate the full relation among the external fields, the effective wall field, the applied currents, and the size of the central domain, the parameters previously presented are now used with currents of  $I=0, 0.1,$  and  $0.2$  Amps. Fig. 22 shows the relation between the external field and the average  $y$ -components of the magnetization in the central cross section with these currents. When the external field is small, competition between the wall and the demagnetizing fields dominate. The central domain does not disappear completely even with a strong applied current. This can be seen in Fig. 22. For larger external fields, the field from the current, and the demagnetizing field become important. Fig. 22

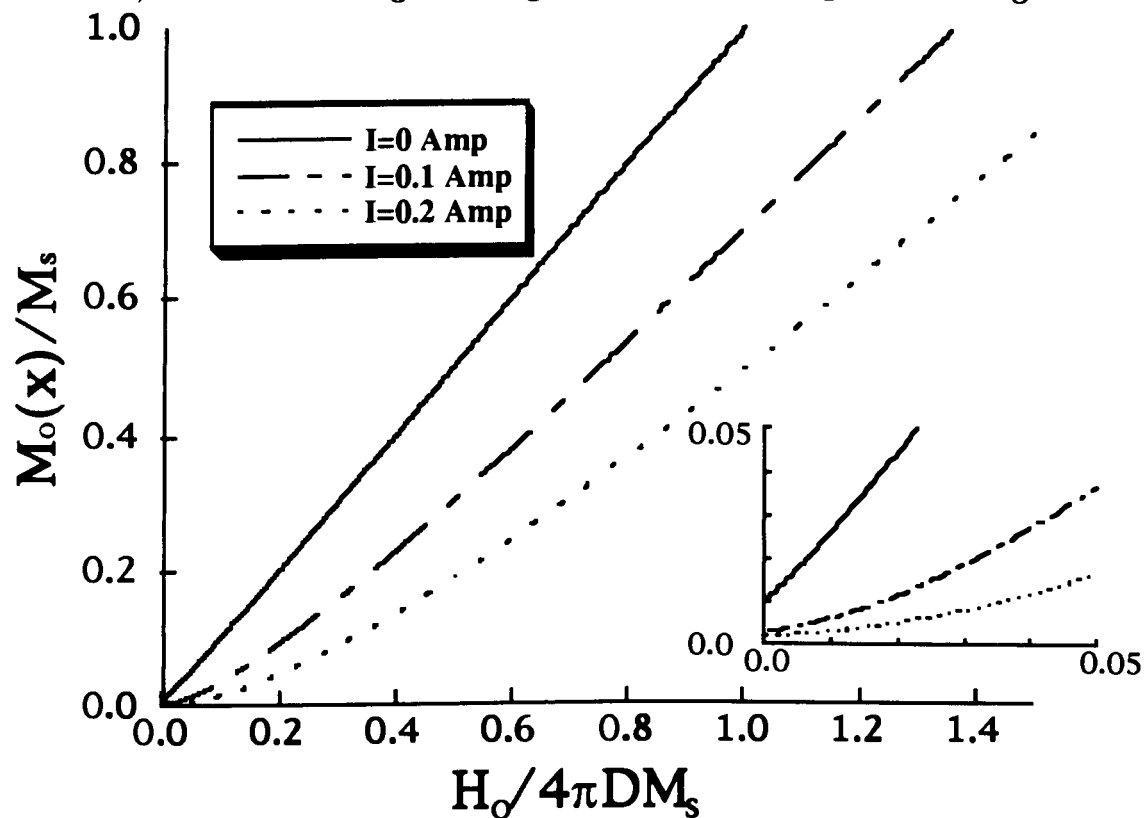


Fig. 22. Calculated relation between magnetization and external field while applying different currents. Detailed diagram at zero field is shown in the blown-up figure.

shows that the magnetization increases rapidly with the external field and zero current but a large applied current makes the magnetization increase much more slowly for small fields.

As the central domain is saturated,  $A(a_w)$  and  $C(a_w)$  become small enough to be ignored. The relation between the saturation field and the applied current is obtained from Eq. 4.3.6 as;

$$H_o = 4\pi DM_s + \frac{2\sqrt{\pi}Id}{5A_s}. \quad \text{Eq. 4.3.7}$$

When a current is applied along the axis of a whisker, the saturation field is linearly related to the applied current. This relation only if the current is sufficient to create the transformed structures. From the experimental result, the ac susceptibility is not changed when the applied current is smaller than critical. The saturation fields from the ac susceptibility and from Eq. 4.3.7 are presented in Fig. 23. Off-set current is considered and  $2d=150 \mu\text{m}$  is used in Fig. 23. The calculated results have some agreement with the results of the measured saturation fields.

From Eq. 4.3.6 and the magnetization,  $M_{y,s}(x)$ , the magnetic stiffness with zero frequency is calculated to be

$$\begin{aligned} \frac{1}{\chi_{\alpha}} = \alpha(0) &= \frac{\partial H_o}{\partial M_{y,s}(x)} = \frac{\frac{\partial H_o}{\partial x}}{\frac{\partial M_{y,s}(x)}{\partial x}} \\ &= 4\pi D + \frac{8\sqrt{\pi}Idx(x + A(a_w))}{5A_s M_s (2x + A(a_w))^3} + \frac{2d|\sigma_1|}{A_s M_s^2 (2x + A(a_w))^3}. \end{aligned} \quad \text{Eq. 4.3.8}$$

The relationship between the zero-frequency susceptibility and the external field, Eq. 4.3.6, with  $I=0.1$  and  $0.2$  Amps is shown in Fig. 24. For all but the smallest fields there is general correspondence



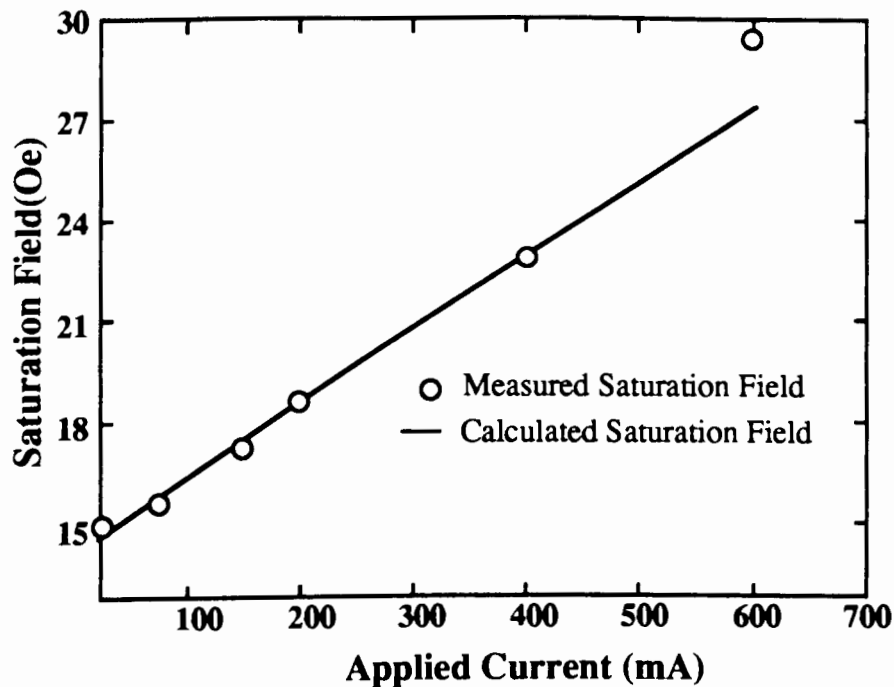


Fig. 23. Comparison between measured saturation fields and calculated fields while applying different currents.

between the model and our measured in-phase signal, e.g., Fig. 20(b), 2). As the external field increases to the saturation field, the susceptibility approaches  $1/4\pi D$ . However, the susceptibility does not vanish before the external field goes to zero; i.e., there is no hole in the dc susceptibility with our model as shown in Fig. 24. This is in conflict with the experimental evidence. The reason for the finite susceptibility at zero field is the wall energy. Because  $x$  appears in the denominator of the second term of Eq. 4.3.6, this field becomes dominant near  $x=0$ . Although the calculated susceptibility with the applied current does not vanish as the external field approaches zero field, the larger current does make the response with zero frequency smaller.

To understand the out-of-phase component of the ac susceptibility, a model based on a cylindrical shape is used to calculate eddy current effects and discussed in the following section.

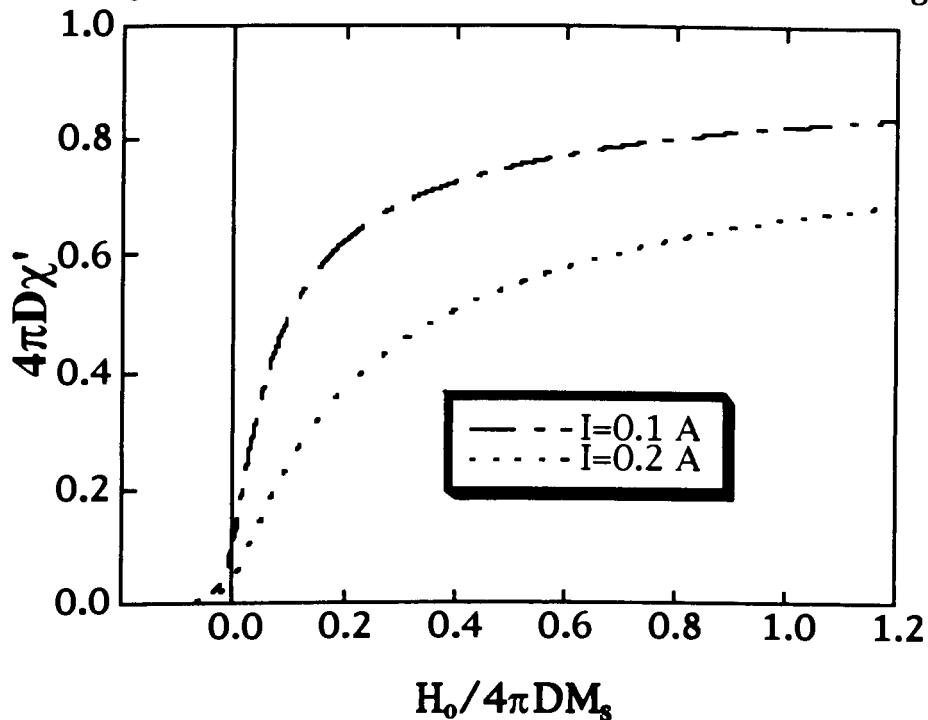


Fig. 24. Calculated dc susceptibility while varying the external field. Parameters are based on the square model and are those used in Figs. 22 and 23.

#### 4.4 Model for the AC Susceptibility

The model suggested in the previous section qualitatively accounts for the magnetization processes in the presence of external fields and applied currents except for fields near zero. In this section, a model based on a cylindrical symmetry is presented and with this model the in-phase and out-of-phase components of ac susceptibility are calculated with a few approximations.

The ac susceptibility is defined<sup>9</sup> from Eq. 2.3.10 as

$$\begin{aligned}\frac{1}{\chi_{xx}} &= 4\pi D + \alpha_i(\omega) + i\omega\beta_i(\omega) \\ &= \alpha(\omega) + i\omega\beta(\omega) \equiv \alpha(0) + i\omega\beta(0).\end{aligned}\tag{Eq. 4.4.1}$$

In the present study, the frequency, 700 Hz, is sufficiently low that  $\alpha(\omega) \equiv \alpha(0)$ , and  $\beta(\omega) \equiv \beta(0)$ . In this section, the magnetic stiffness,  $\alpha(0)$ , will be derived first and then the magnetic viscosity,  $\beta(0)$ , will be calculated.  $\alpha(0)$  is obtained from the relation between the external field and the magnetization and  $\beta(0)$  is determined by eddy current losses. With the square geometry the magnetic viscosity is difficult to calculate so a new model will be introduced to solve it. The results of the ac susceptibility measurements will be explained with the calculated susceptibility for most external fields. But this model will not explain what happens in low fields even with a high current. The low field region remains beyond the scope of this thesis.

#### 4.4.1 AC Susceptibility with Zero Frequency

We assume that when external fields and currents are applied along the principal axis of a cylindrical whisker, the magnetization in the central cross section is also along the principal axis within an inner circle of radius  $r$  and the magnetization outside  $r$  is in the plane, as shown in Fig. 25. The external field and the demagnetizing field are assumed to be uniform over the central cross section.

The dominant energies consist of the demagnetizing energy, the magnetostatic energies from an external field and from an applied current, and the wall energy. The sum of the energy from the

external field per unit length and the demagnetizing energy per unit length is

$$\bar{E}_H + \bar{E}_D = -H_o M_{y,c}(x) A_s + \frac{1}{2} \lambda M_{y,c}^2(x) A_s, \quad \text{Eq. 4.4.2}$$

where  $\lambda (= 4\pi D)$  is the demagnetizing factor,  $x$  is a dimensionless parameter defined as  $\frac{r}{R}$ , and  $A_s = \pi R^2$  is the cross section of the cylinder.

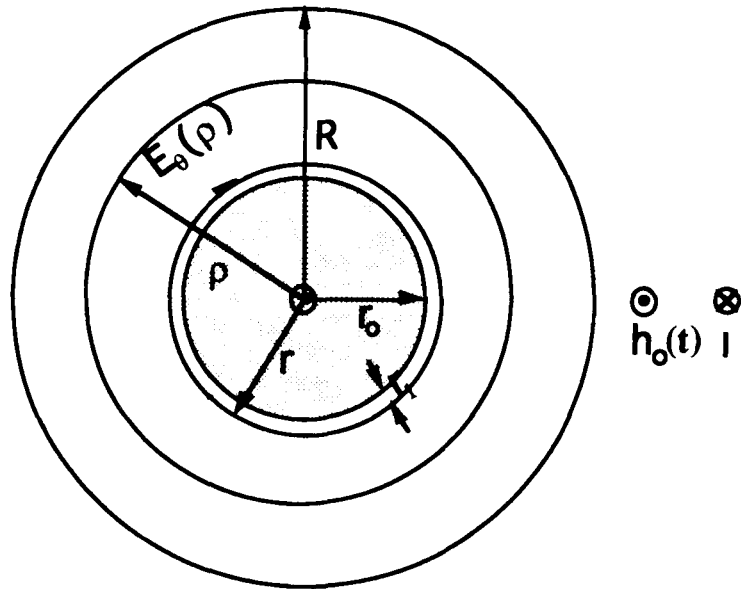


Fig. 25. Schematic diagram for an eddy current calculation.

$r = r_0 + r_1$  where  $r_1$  is the amplitude of the vibrating wall.

The average magnetization along the principal axis for the central cross section is assumed to have the form

$$M_{y,c}(x) = M_s((1 - s - m_o)x^2 + sx + m_o). \quad \text{Eq. 4.4.3}$$

This form mimics Eq. 4.3.1. The first term of Eq. 4.4.3,  $(1 - s - m_o)x^2 M_s$ , increases with the area of the saturated magnetization in the central domain, the second term,  $sxM_s$ , describes the magnetization of changing domain wall, and increases with its length. ( $sxM_s$  is the

average magnetization per unit length of the wall.) The last term,  $m_o M_s$ , is the residual magnetization which is chosen not to disappear for  $x=0$ . The reason of choosing  $(1-s-m_o)$  in the first term is that for  $x=1$ ,  $M_{y,c}(1) = M_s$  and for  $x=0$ ,  $M_{y,c}(0) = m_o M_s$ .

The energy from the current per unit length is approximated as in Section 4.3

$$\bar{E}_I = \bar{E}_{I_o} + \frac{2\pi}{15} \frac{\pi I}{\pi R^2} r^3 M_s = \bar{E}_{I_o} + \frac{2\pi^{\frac{1}{2}} I A_s^{\frac{1}{2}}}{15} x^3 M_s. \quad \text{Eq. 4.4.4}$$

In the cylindrical model there are no (110) 90° walls to make the wall energy decrease with the increase of the central domain. From the square model, the wall energy density per unit length is known as  $|\sigma_1| = 8(\frac{1}{\sqrt{2}} - \frac{1}{\sqrt{3}})\sigma_a$ . For the cylindrical model this is done artificially by letting the wall energy per unit length have a negative sign

$$\bar{E}_w = -2\pi|\sigma_o|xR \quad \text{Eq. 4.4.5}$$

where the wall energy coefficient  $|\sigma_o|$  is chosen as  $\frac{|\sigma_1|}{4\sqrt{\pi}}$ .

The total energy per unit length is written as

$$\begin{aligned} \bar{E}_{tot} &= \bar{E}_H + \bar{E}_D + \bar{E}_I + \bar{E}_w \\ &= \bar{E}_{tot_o} - H_o M_{y,c}(x)A_s + \frac{1}{2}\lambda M_{y,c}^2(x)A_s + \frac{2\pi^{\frac{1}{2}} I A_s^{\frac{1}{2}}}{15} x^3 M_s - 2\pi|\sigma_o|xR \end{aligned} \quad \text{Eq. 4.4.6}$$

Minimizing the total energy with respect to  $x$ , the external field is

$$H_o = 4\pi D M_s ((1-s-m_o)x^2 + sx + m_o) + \frac{-\frac{2\pi|\sigma_o|R}{A_s M_s} + \frac{2Ix^2\pi^{\frac{1}{2}}}{5A_s^{\frac{1}{2}}}}{2x(1-s-m_o) + s}.$$

$$\text{Eq. 4.4.7}$$

The differential susceptibility for zero frequency is

$$\begin{aligned}\chi_o &\equiv \frac{1}{\alpha(0)} = \frac{\partial M_{y,c}(x)}{\partial H_o} = \frac{\frac{\partial M_{y,c}(x)}{\partial x}}{\frac{\partial H_o}{\partial x}} \\ &= \frac{M_s(2x(1-s-m_o)+s)^3}{4\pi D M_s(2x(1-s-m_o)+s)^3 + (1-s-m_o)\left(\frac{4\pi^{\frac{1}{2}} I x^2}{5A_s^{\frac{1}{2}}} + \frac{4\pi|\sigma_o|R}{A_s M_s}\right) + \frac{4\pi^{\frac{1}{2}} I s x}{5A_s^{\frac{1}{2}}}}.\end{aligned}$$

Eq. 4.4.8

The magnetic stiffness is

$$\alpha(0) = 4\pi D + \frac{4\pi(1-s-m_o)|\sigma_o|R}{A_s M_s^2(2x(1-s-m_o)+s)^3} + \frac{4\pi^{\frac{1}{2}} I x((1-s-m_o)x+s)}{5A_s^{\frac{1}{2}} M_s(2x(1-s-m_o)+s)^3}.$$

Eq. 4.4.8a

Again the field dependence of the susceptibility is found using Eqs. 4.4.7 and 4.4.8a for any  $x$  as the parameter. This susceptibility is similar to Eq. 4.3.8 calculated for a square cross section.

$M_{y,c}(x)$  and  $\chi_o$  are functions of applied currents and external fields. Appropriate numbers based on the square model are chosen for calculating the magnetization responses; e.g.,  $s = 0.001$ ,  $A_s = (200 \mu\text{m})^2$ ,  $|\sigma_o| = 0.18 \text{ erg/cm}^2$ ,  $M_s = 1715 \text{ emu/cm}^3$ , and  $\lambda = 4\pi D = 0.00577$ . With  $m_o = 3.8 \times 10^{-4}$ , based on the square model, the calculated susceptibility does not disappear at zero external field. But the experimental results show that the in-phase signal is diminished before the external field reaches zero field.

To see what would be required for this model to predict a zero response region, the parameter  $m_o$  is changed. There is no justification for taking  $m_o = 0.04$ , but if we do it is possible to match the observed behavior in low and high fields at some particular applied currents.

Fig. 26(a) shows the response of the differential susceptibility and the magnetization with  $m_o = 0.04$  while varying the external field for currents of 0.1, 0.2, and 0.25 Amps. An increase in applied currents makes the differential susceptibility and the magnetization decrease. The dependence of susceptibility on currents is consistent with the previous calculation. The effect of  $m_o$  is to produce a larger residual demagnetizing field, which must be overcome before the

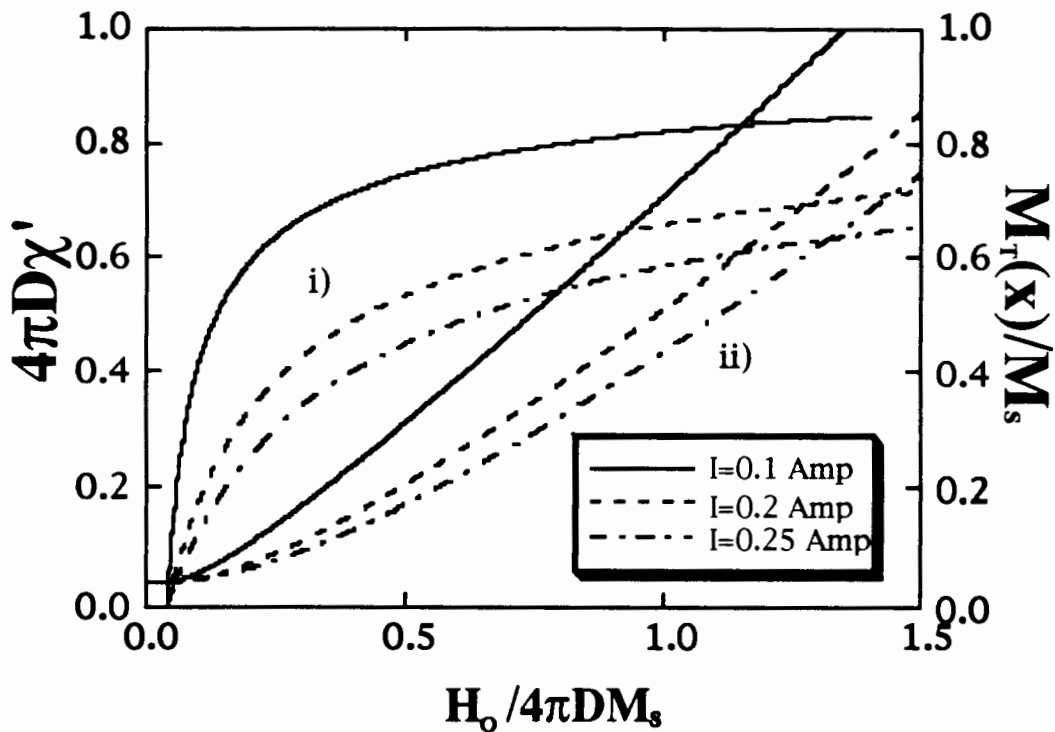


Fig. 26(a). Calculated i) dc susceptibility and ii) magnetization while varying external field. Here we use an unrealistically high value for  $m_o = 0.04$ .

susceptibility increases with applied field. This  $4\pi Dm_o M_r$  can be considered as a contribution to the demagnetizing field from behavior of the magnetization away from the central cross section. Once the applied field is large enough to overcome this unexplained

demagnetizing field effect, the behavior is well explained by the present model.

Another way to match the calculated susceptibility with the experimental data is to change the sign of the wall energy. Fig. 26(b) shows the relationship between external fields and the calculated magnetization with different signs of the wall energies for low fields and the calculated in-phase susceptibility for each case. From the square model, the wall energy coefficient is negative. With the negative coefficient, the susceptibility does not disappear completely due to the wall energy when the field approaches zero field. This behavior is shown in Fig. 26(b). When the wall coefficient is positive, the central domain tries to move in towards the center of a whisker

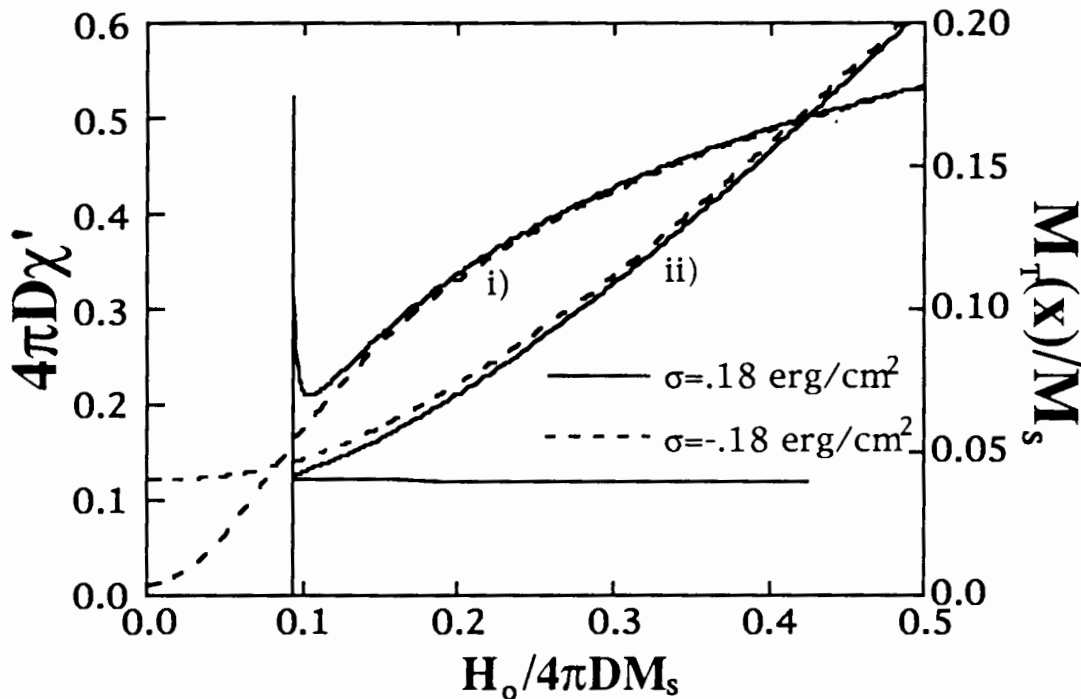


Fig. 26(b). Same as Fig. 26(a) with different signs of wall energies.  
 $I=0.2$  Amp.



and there is an instability shown in Fig. 26(b). There is no reason for the sign for the wall coefficient to be positive. If it were the magnetization would show a first-order transition near zero field and the susceptibility would disappear before the field approaches zero field. This transition is shown in Fig. 26(b).

#### 4.4.2 In-Phase and Out-of-Phase Components of AC Susceptibilities

To calculate the magnetic stiffness we must consider the eddy current field. The effective magnetic field inside a magnetic material can be expressed as

$$\begin{aligned}\vec{H}_{eff} &= \vec{H}_o(t) + \vec{H}_D(t) + \vec{H}_I(t) + \vec{H}_w(t) + \vec{h}_e e^{i\omega t} \\ &= \vec{H}_o + \vec{H}_D + \vec{H}_I + \vec{H}_w + (\vec{h}_o + \vec{h}_D + \vec{h}_I + \vec{h}_w + \vec{h}_e) e^{i\omega t}\end{aligned}\quad \text{Eq. 4.4.9}$$

where  $H_o$  and  $h_o$  are the dc and ac external fields,  $H_D$  and  $h_D$  are the dc and ac demagnetizing fields,  $H_I$  and  $h_I$  are the dc and effective ac fields from current,  $H_w$  and  $h_w$  are the dc and effective ac wall fields, respectively, and  $h_e$  is the eddy current field induced by moving domain walls. All other capital and small letter  $h$ 's in Eq. 4.4.9 are vector magnitudes and all the time dependence is in the exponential term. The internal field satisfies Maxwell's equations:<sup>33</sup>

$$\nabla \times \vec{H}_i = \frac{4\pi}{c} \vec{j} = \frac{4\pi}{c} \sigma_c \vec{E}_e, \quad \text{Eq. 4.4.10a}$$

$$\nabla \times \vec{E}_e = -\frac{1}{c} \frac{\partial}{\partial t} (4\pi M_{y,c}). \quad \text{Eq. 4.4.10b}$$

By integrating Eq. 4.4.10b for the geometry of a cylindrical shape,

$$\int \bar{E}_e \cdot \hat{n} dS = -\frac{4\pi}{c} \frac{\partial}{\partial t} \phi_M = -\frac{4\pi}{c} \frac{\partial}{\partial t} (\pi r^2 M_s) \quad \text{Eq. 4.4.10c}$$

where  $\phi_M$  is the magnetic flux inside a whisker. The last equation for a whisker is written as

$$2\pi\rho E_{e,\theta}(\rho) = -\frac{4\pi}{c} \frac{\partial}{\partial t} \pi r^2 M_s \quad \text{Eq. 4.4.10d}$$

where  $\rho$  is a radius between the radius  $r$  of the wall and the outside cylinder  $R$  as shown in Fig. 25. Using Eqs. 4.4.10a and 4.4.10d, the eddy current equation is written as

$$-\frac{\partial}{\partial \rho} h_e(\rho) e^{i\alpha x} = \frac{4\pi}{c} \sigma_c E_{e,\theta} = -\frac{4\pi}{c} \frac{\sigma_c}{c} \frac{A_s}{2\pi\rho} \frac{\partial}{\partial t} 4\pi(M_{y,c}) \quad \text{Eq. 4.4.11}$$

where  $\sigma_c$  is the electric conductivity of an iron whisker. The contribution to the magnetic flux from the external magnetic field inside the sample has been ignored to simplify the eddy current problem. The eddy current loss is related to the out-of-phase component of the ac susceptibility. The contribution from the magnetization at corners and from walls is not important to calculate the eddy current loss, so the magnetization is approximated as  $M_{y,c} (\approx M_{y,c}(x)) = \frac{M_s r^2}{R^2}$ . After calculating the ac eddy current loss and the magnetic stiffness with  $M_{y,c} = M_s r^2 / R^2$ , the magnetic stiffness,  $\alpha(0)$ , will be substituted with Eq. 4.4.8a.

When an ac driving field,  $h_0 e^{i\alpha x}$ , is applied along the principal axis, the vibrating wall radius and the magnetization are written as

$$r = r_0 + r_1 e^{i\alpha x}, \quad \text{Eq. 4.4.12a}$$

$$M_{y,c} = \frac{M_s r^2}{R^2} \approx \frac{M_s (r_o^2 + 2r_o r_1 e^{i\alpha x})}{R^2} \quad \text{Eq. 4.4.12b}$$

$$= M_{y,c_0} + m e^{i\alpha x}$$

where  $M_{y,c_0} = M_s \frac{r_o^2}{R^2}$ , and  $m = \frac{2r_o r_1}{R^2}$ . The radius of the mean position of the wall is  $r_o$  and the amplitude of the vibrating wall is  $r_1$  as shown in Fig. 25. Eq. 4.4.11 yields

$$h_s(r_o) e^{i\alpha x} = h_s(\rho) e^{i\alpha x} + \left[ \log \frac{r_o}{\rho} \right] \frac{8\pi\sigma_c M_s A_s}{c^2 R^2} \frac{\partial}{\partial t} (r^2) \quad \text{Eq. 4.4.13}$$

and with the boundary condition ( $h_s(\rho)|_{\rho=R} = 0$ ) it becomes

$$h_s(r_o) e^{i\alpha x} = \frac{8\pi^2\sigma_c M_s}{c^2} \frac{\partial}{\partial t} (r^2) \log \frac{r_o}{R} \quad \text{Eq. 4.4.14}$$

$$= \frac{8\pi^2\sigma_c M_s (2r_o \omega r_1 e^{i\alpha x})}{c^2} \log \frac{r_o}{R}.$$

When Eq. 4.4.14 is substituted into Eq. 4.4.8, the magnitude of the magnetic field inside the sample is given as

$$H_{\text{eff}} = H'_{\text{eff}} + (h'_o + i\omega \frac{16\pi^2\sigma_c M_s r_o r_1}{c^2} \log \frac{r_o}{R}) e^{i\alpha x} \quad \text{Eq. 4.4.15}$$

where  $H'_{\text{eff}} = H_o + H_D + H_I + H_w$  and  $h'_o = h_o + h_D + h_I + h_w$ .

Now the terms in  $H'_{\text{eff}}$  and  $h'_o$  must be determined to find the magnetic stiffness. From Fig. 25, the demagnetizing field is written as

$$H_D(t) = -4\pi D \frac{M_s r^2}{R^2} \approx -4\pi D \frac{M_s (r_o^2 + 2r_o r_1 e^{i\alpha x})}{R^2}. \quad \text{Eq. 4.4.16}$$

The field from the applied current is given by

$$H_I(t) = -\frac{Ir}{5R^2} = -\frac{I(r_o + r_1 e^{i\alpha x})}{5R^2}. \quad \text{Eq. 4.4.17}$$

The effective wall field is

$$H_w(t) = \frac{|\sigma_o|}{r M_s} = \frac{|\sigma_o|}{r_o^2 M_s} (r_o - r_1 e^{i\alpha x}). \quad \text{Eq. 4.4.18}$$

Since the effective field at the wall has to be zero, the following relations are obtained

$$H_o = \frac{4\pi DM_s r_o^2}{R^2} + \frac{I r_o}{5R^2} - \frac{|\sigma_o|}{M_s r_o}, \quad \text{Eq. 4.4.19}$$

$$h_o = r_1 \left( \frac{8\pi DM_s r_o}{R^2} + \frac{I}{5R^2} + \frac{|\sigma_o|}{M_s r_o^2} - i\omega \frac{16\pi^2 \sigma_c M_s r_o \log \frac{r_o}{R}}{c^2} \right). \quad \text{Eq. 4.4.20}$$

From Eq. 4.4.20, the amplitude of the vibrating wall is

$$r_1 = \frac{h_o}{\frac{8\pi DM_s r_o}{R^2} + \frac{I}{5R^2} + \frac{|\sigma_o|}{M_s r_o^2} - i\omega \frac{16\pi^2 \sigma_c M_s r_o \log \frac{r_o}{R}}{c^2}} \quad \text{Eq. 4.4.21}$$

and from Eqs. 2.3.9 and 4.4.12b, the amplitude of the change in the magnetization is

$$\begin{aligned} m &\equiv h_o \left( \frac{1}{\alpha'(0) + i\omega\beta'(0)} \right) = \frac{2r_o M_s r_1}{R^2} \\ &= \frac{2r_o M_s h_o}{8\pi DM_s r_o + \frac{I}{5} + \frac{R^2 |\sigma_o|}{M_s r_o^2} - i\omega \frac{16\pi^2 R^2 \sigma_c M_s r_o \log \frac{r_o}{R}}{c^2}} \end{aligned} \quad \text{Eq. 4.4.22}$$

where  $\alpha'(0) = \frac{(8\pi DM_s r_o + \frac{I}{5} + \frac{|\sigma_o| R^2}{M_s r_o^2})}{2r_o M_s}$  and  $\beta'(0) = -\frac{8\pi^2 R^2 \sigma_c \log \frac{r_o}{R}}{c^2}$ . The

magnetic stiffness should be replaced with  $\alpha(0)$  in Eq. 4.4.8a. The ac susceptibility is then given by

$$\frac{1}{\chi_{ax}} = \alpha(0) + i\omega\beta(0) \quad \text{Eq. 4.4.1}$$

where  $\beta(0) = \beta'(0)$ .

These derived magnetic responses are called Stage I. The in-phase and out-of-phase components of the susceptibilities are obtained from Eq. 4.4.1

$$\chi_{ax} = \chi' - i\chi'', \quad \text{Eq. 2.3.10a}$$

where

$$\begin{aligned} \chi' &= \frac{\alpha(0)}{\alpha(0)^2 + \omega^2\beta(0)^2}, \\ \chi'' &= \frac{\omega\beta(0)}{\alpha(0)^2 + \omega^2\beta(0)^2}. \end{aligned} \quad \text{Eq. 2.3.10b}$$

The above eddy current calculation is valid if the magnetization is not too close to saturation. But, experimental data show the magnetic viscosity increases rapidly when the external field becomes larger than point (k) in Fig. 19. It is necessary to reconsider the eddy current for this region, Stage II. From point (k) to the saturation field in Fig. 19, the model remains the same except that the loss term is replaced by

$$\omega\beta(0) = -\omega\beta_{II} \log \frac{R^2}{R^2 - r_o^2} \quad \text{Eq. 4.4.23}$$

where  $\beta_{II}$  depends on the dimensions of the whisker. We have no theory for  $\beta_{II}$  but it is chosen as  $\frac{4\pi^2 R^2 \sigma_c}{c^2}$  in order to have a change from Stage I to Stage II without change in loss, which is what is generally observed. The magnetic process corresponding to Stage II is from points (b) to (c) in Fig. 19 and the corresponding region for positive fields.

Experimental results show that when the external field increases from zero field to the departure field, the magnetic response changes from Stage I to Stage II. To explain these magnetic responses, proper numbers based on the experimental data are chosen as  $M_s = 1715 \text{ emu} / \text{cm}^3$ ,  $A_p = \pi R^2 = (150 \text{ } \mu\text{m})^2$ ,  $\omega = 2\pi f = 1400\pi$ ,  $\frac{\sigma_c}{c^2} = 10^{-4}$ , and  $4\pi D = 0.00577$ .  $s = 1.7 \times 10^{-4}$ ,  $|\sigma_o| = 0.37 \text{ erg} / \text{cm}^2$ , and

$m_o = 3.8 \times 10^{-4}$  based on the square model are used for the calculation. As explained in Sections 4.3.2 and 4.4.1, the wall energy and  $m_o$  are important to determine the magnetic response at low field. But the low field response is not fully understood, yet.

Stage I calculations are shown in Fig. 27(a) for currents of 0.1, 0.2, and 0.5 Amps. Fig. 27(a) shows the calculation of the field dependence of the in-phase and out-of-phase components of the ac susceptibility. Fig. 27(a) shows the in-phase and out-of-phase signals decrease with increasing the applied current. When the external field decreases to zero field, ac susceptibilities decreases rapidly towards zero but the signals do not disappear before the external field approaches zero field. As the external field increases, the in-phase signal approaches  $1/4\pi D$ . These calculated out-of-phase responses are similar to the measured ac susceptibility for Stage I in Fig. 17.

To compare the experimental data, Fig. 20(b), with our calculated response in detail, the ac signals are calculated with  $A_p = \pi R^2 = (150 \mu\text{m})^2$ ,  $\lambda = 4\pi D = 0.00577$ , and  $I=0.1$  Amp and they are shown in Fig. 27(b). As explained previously, the experimental data show the out-of-phase component of ac susceptibility changes from Stage I to Stage II as the external field is increased and the calculated out-of-phase response is similar to that observed experimentally in Fig. 20(b).

The existence of a small central domain with zero field is found by the competition between the wall energy and the demagnetizing energy in Section 4.3.2. The in-phase and out-of-phase components of the ac responses, experimentally observed, are explicable with our models for most of external fields, but not for low field. The relation

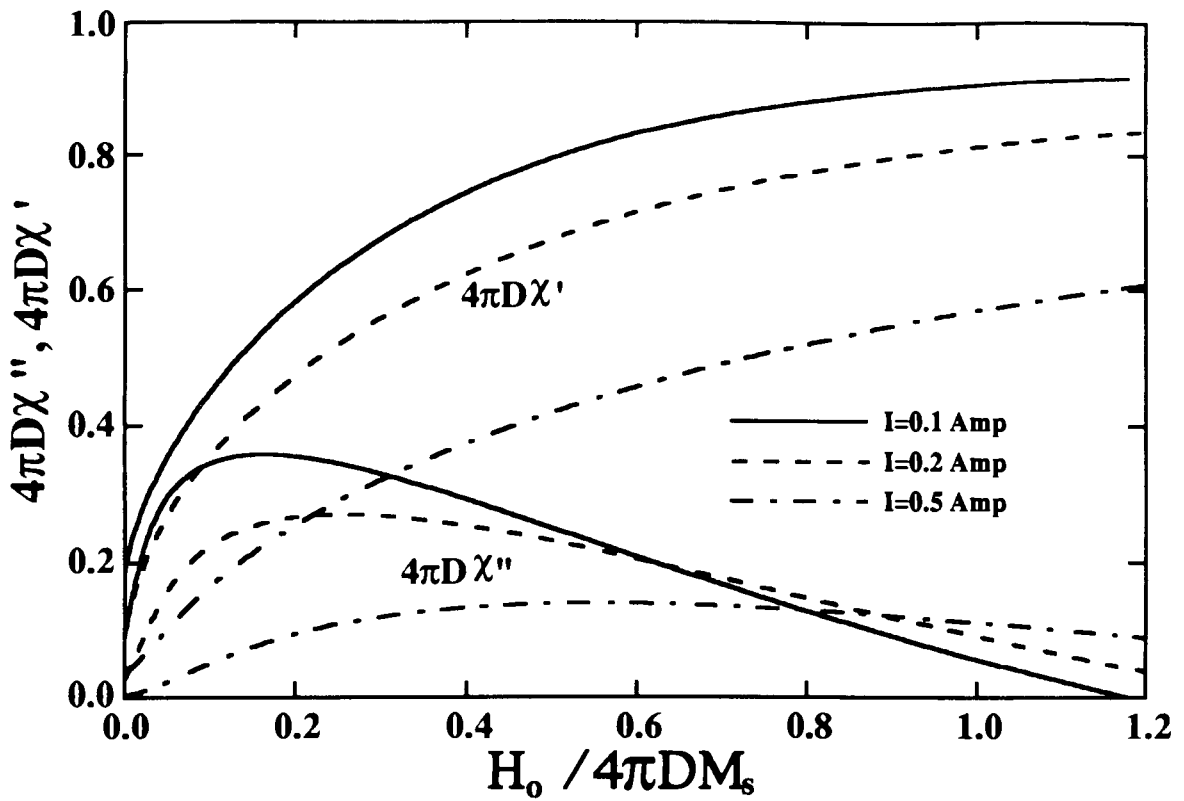


Fig. 27(a). Calculated out-of-phase and in-phase responses.

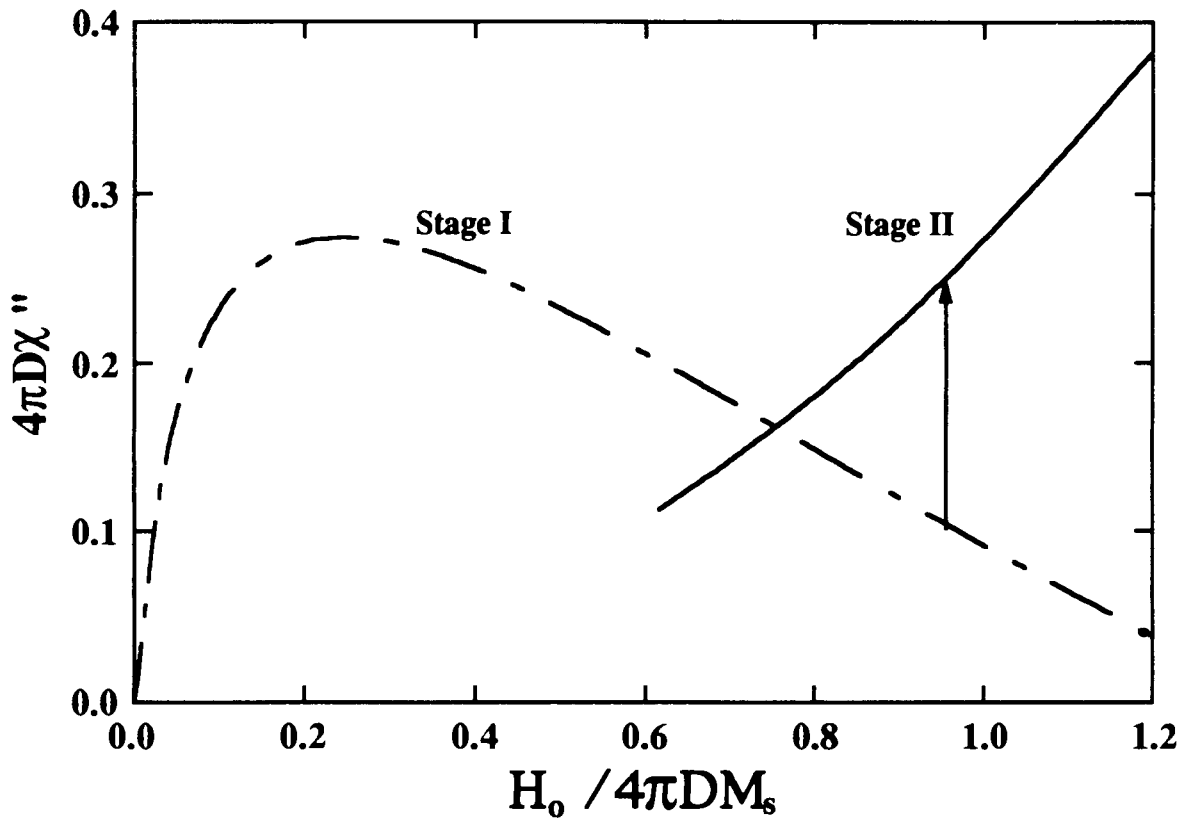


Fig. 27(b). Calculations of the field dependence of  $\chi''$  for Stage I and Stage II.

between saturation fields and applied currents is also explained in Section 4.3.2.

## **4.5 Domain Structures deduced from AC Susceptibility and Resistance Measurements**

### **4.5.1 Structures deduced from AC Susceptibility**

There are five irreversible processes in the out-of-phase response of a <100> whisker when sufficient current is applied. They are discussed here in terms of a proposed set of domain structures.

The first irreversible change occurs when the external field is increased from a high negative field to the nucleation field, as in Fig. 19. The response shows a large discontinuous increase at the nucleation field. This increase is due to the nucleation of domains at the centers of the whisker's side surfaces. Since the field from the applied current, as shown in Fig. 11(b), is largest at these points, the nucleation also should start at these point. The subsequent decreasing out-of-phase signal with increasing field is explained by the growth of domains as the magnitude of the external field is decreased towards point (c) in Fig. 19. The domains grow in response to the decreasing magnitude of the external field and the movement of the larger domain walls produces lower eddy current losses. Fig. 28(a) is deduced from the above observations. The rounded shapes of the domains produce the volume and surface charges as shown in Fig. 29. The rounded shape of the domains is designed to



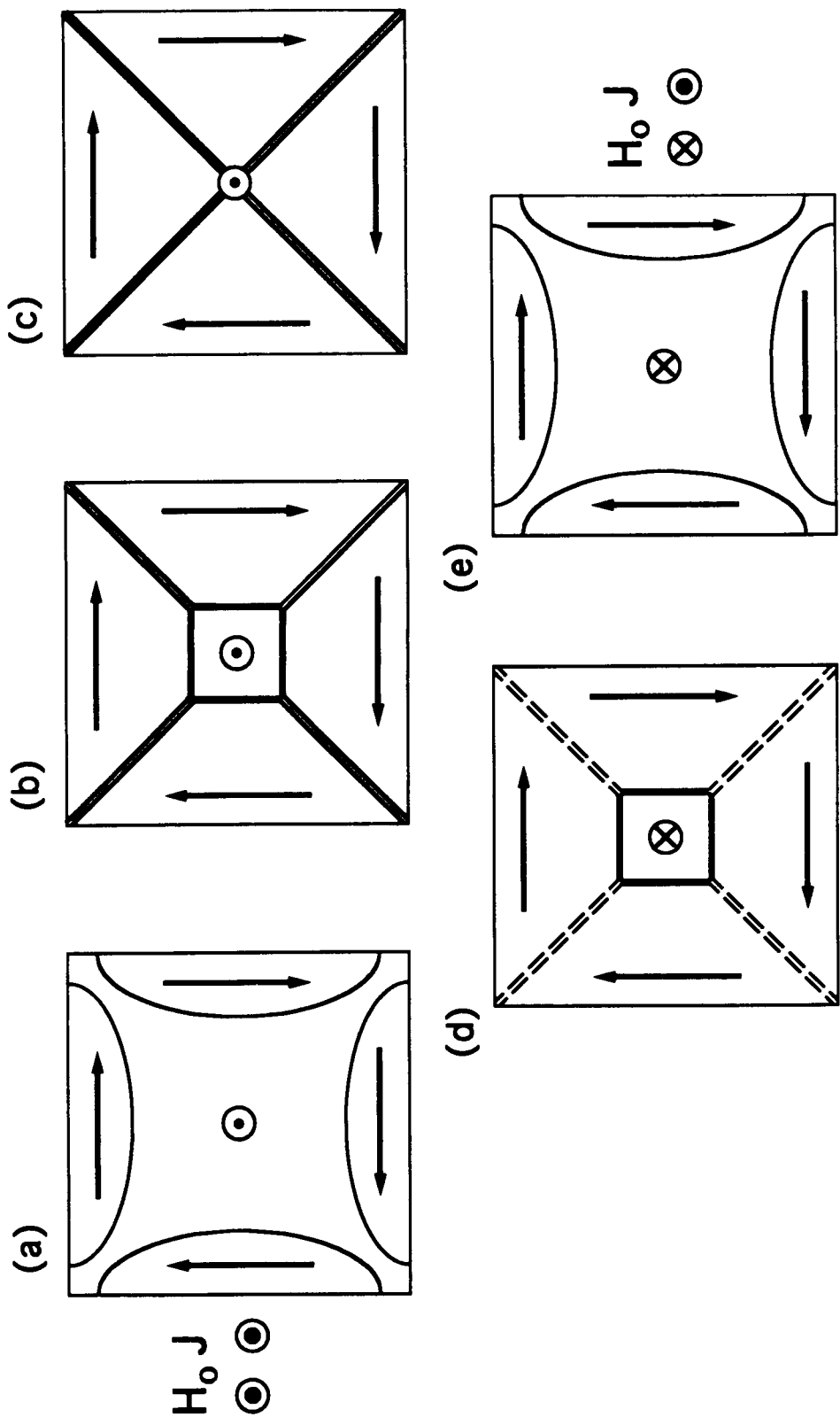


Fig. 28. Domain structures deduced from ac susceptibility measurements, (a) nucleation (b) coalescence, (c) collapse, (d) renucleation, and (e) splitting.

reduce the magnetostatic energy. According to Bloomberg and Arrott,<sup>21</sup> about 2.3 % of the total charges remain inside a whisker when the homogenous external field distorts the Landau structure. The present situation does not fully correspond to theirs, but it is close enough to be suggestive.

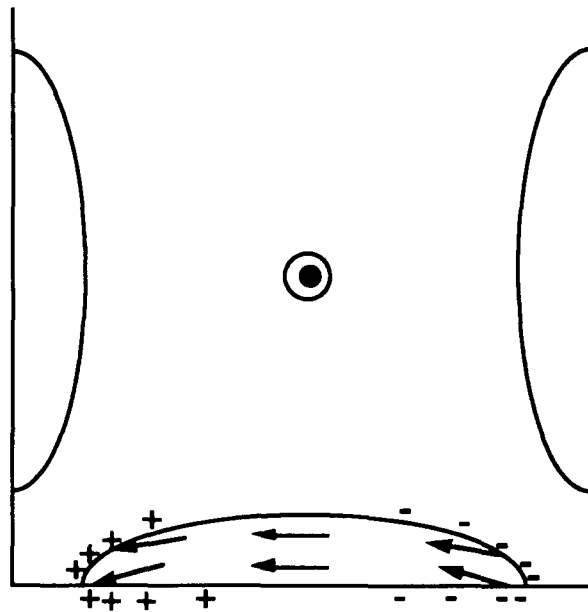


Fig. 29. Diagram for curved domains at nucleation

When the magnitude of the field is decreased further, the magnetic process becomes irreversible at point (c) in Fig. 19. The irreversible process is explained by the coalescence of the four separated domains into four domains separated by (110)  $90^\circ$  walls as in Fig. 28(b). The magnetization inside these domains is directed along the easy axes except in the walls. The domain structure becomes stable and there are no longer any volume charges. When the magnitude of the external field is increased back towards the

departure field, the out-of-phase signal decreases as point (d) in Fig. 19 is approached. This signal decreases because the central core becomes larger with increasing external field in the direction of the core magnetization. Since the eddy current losses are due to the vibration of the walls around the central core, the larger walls result in smaller losses, or small signal.

When the magnitude of the external field decreases through point (d) in Fig. 19, a discontinuous jump is observed. It is explained as a transformation of the domain structure back from that of Fig. 28(b) back to that of Fig. 28(a), i.e., (110) 90° walls are separated and four domains near surfaces are shrinking rapidly.

The decreasing out-of-phase signal as the field approaches the collapse field, (e) to (f) in Fig. 19, indicates that the (100) 90° walls around the central core are contracting toward the center of the whisker. The domain structure becomes that of Fig. 28(c) at the collapse field. Then the out-of-phase signal becomes negligible. The experimental data show that the collapse field is not sensitive to applied current. The size of the inner domain becomes too small to generate any appreciable signal at the collapse field, and the out-of-phase signal becomes unobservable.

The collapsed structure of Fig. 28(c) remains without change until the field increases up to the renucleation field, point (g) in Fig. 19. The renucleation field depends on the applied current, the history of field cycles, and the sizes of whiskers. When the external field passes through the renucleation field, a discontinuous jump is observed. This rapid increase in the out-of-phase signal is interpreted as a sudden irreversible change in the domain structure

of the whisker. Magnetic singularities might be nucleated somewhere near an end of the whisker and they might propagate along the axis of the whisker. As the singularities pass through the central cross section, the magnetization in the central domain reverses, as in Fig. 28(d). With further increase in the external field the renucleated central domain expands. The structure of the (110)  $90^\circ$  walls might not change during the irreversible nucleation of the reversed central domain. This would lead to some sort of singularity in these domain walls. The singularity could propagate from the inner end of the wall, results in a change in the sense of wall rotation.

When the external field increases past point (k) in Fig. 19, the four domains connected by (110)  $90^\circ$  walls separate as shown in Fig. 28(e). When the external field increases beyond the departure field, the magnetization is saturated at the middle of the whisker and the edge domains disappear resulting in a drop in signal to near zero.

The difference between (b) and (d) in Fig. 28 is the direction of the (110)  $90^\circ$  walls. The direction of the magnetization in these  $90^\circ$  walls is along the external field for Fig. 28(b). But for Fig. 28(d) it need not be. The direction is clear when going from Figs. 28(b) to (c). But it is not clear whether the wall might reverse sense by propagation of the singularity that must be there if the sense is not reversed. If the wall does reverse, it is likely to be when the central core reverses. The experiments should be insensitive to this reversal.

The out-of-phase and in-phase ac signals with a low applied current ( $I=150$  mA) is shown in Fig. 20(a). Fig. 20(a) shows clear evidence for a collapse field while the external field approaches zero. It appears that in this case the collapse is discontinuous. The

in-phase signal shows that the intrinsic susceptibility is negative for an external field between the collapse field and that required to break the 90° walls, the transition from Figs. 28(d) to (e). The negative susceptibility indicates that the domain structure inside the whisker would not be stable if it were not for the demagnetizing field. The out-of-phase signal does not indicate the presence of this unstable structure. This instability is not understood in the context of the present model.

#### 4.5.2 Discussions of the Resistance Measurements

When a current larger than critical is applied along the axis of a whisker, its resistance decreases to a minimum in zero field. As explained previously, the lowest resistance is expected when all domains are magnetized perpendicular to the applied current. Fig. 28(c) corresponds to the minimum resistance. For a higher current, the resistance is expected to increase slowly. But this increase is not clearly shown in Fig. 15 because of the large uncertainty in the measurements. The increase in the size of the central domain, where the magnetization is parallel to the current, explains the increase in resistivity with increasing measuring field as observed in Fig. 15.

The changes in resistance can be made quantitative as discussed in Section 4.3 for the domain structure of Fig. 28(b). The magnetization is approximated as  $M_{y,z}(x) \approx M_s x^2$  and from Eq. 2.4.5b the relationship between the resistance change and the magnetization

can be written as  $\Delta R = \Delta R_{\max} \frac{M_s - M_{y,s}(x)}{M_s}$ . The effective wall field in

Eq. 4.3.6 is small enough to be ignored when the central domain becomes large and the effective external field can be written as

$$\begin{aligned} \frac{H_o}{4\pi DM_s} &= x^2 + \frac{dlx}{10\sqrt{\pi}DM_s A_s} = \frac{M_{y,s}(x)}{M_s} + IF \left[ \frac{M_{y,s}(x)}{M_s} \right]^{\frac{1}{2}} \\ &= \frac{\Delta R_{\max} - \Delta R}{\Delta R_{\max}} + IF \left[ \frac{\Delta R_{\max} - \Delta R}{\Delta R_{\max}} \right]^{\frac{1}{2}}. \end{aligned} \quad \text{Eq. 4.5.1}$$

where  $F = \frac{d}{10\sqrt{\pi}DM_s A_s}$  is a constant independent of the current and the

external field and  $\Delta R_{\max}$  is the maximum change in the resistance by the effect of magnetoresistance.  $\Delta R$  is the magnitude of the in resistance from saturation for a partially saturated domain structure, as defined in Section 2.4. The resistance of the whisker increases and the whisker approaches saturation as the external field increases.

The resistance data in Fig. 15(a) are explicable with this relation.

With no external field,  $\Delta R$  is equal to  $\Delta R_{\max}$ . At the saturation field,

$$\frac{H_o}{4\pi DM_s} = 1 + IF.$$

The resistance measurement did not give us enough information to identify all the domain structures deduced from the susceptibility measurement. But, most results of the resistance measurements are consistent with the ac susceptibility measurements. If an applied current less than critical, e.g., about 20 mA, were used for the resistance measurement, the resistivity should not be changed at all with field or current. This experiment was not done because the signal to noise ratio was not favorable.

### 4.5.3 Conclusions

The cause of the domain formation with magnetization in the plane of the central cross section is the field from the current acting on the magnetic moments. The pattern is dominated by the lowering of the energy that is achieved by avoiding the formation of magnetic charge. This keeps the magnetization parallel to the side on each of the four sides. The exchange energy tries to keep the moments parallel to one another. The anisotropy energy keeps the magnetization close to one of the  $\langle 100 \rangle$  directions in each of the domains. These effects are strong enough that the magnetization is uniform everywhere in each domain except in the walls where there is a transition from one domain to another. At the center of the pattern, a singularity in the exchange energy density is avoided by directing the magnetization along the axis of the  $\langle 100 \rangle$  whisker. This small core does not have significant effects on the ac susceptibility or dc resistance measurements.

This domain structure of Fig. 28(c) is not changed until the external field is stronger than the renucleation field if the external field is in the direction opposite to the central domain magnetization. As the field becomes larger than the renucleation field the magnetization in the central core reverses and becomes a square domain surrounded with  $(100)$   $90^\circ$  walls. This domain configuration is very similar to the one shown in Fig. 28(b) or (d). When the applied current becomes stronger, the field necessary to renucleate the central domain increases. As the external field increases to the saturation field, the domain walls move out toward the whisker

surfaces and the 90° walls with {110} planes separate. The field required to separate the walls becomes closer to the departure field as the applied current becomes stronger. The saturation field also increases with increases in the applied current.

The domain structures deduced from the ac susceptibility and the magnetoresistance experiments are not consistent with the one suggested by Shumate *et al.* If their domain structure were valid, the resistance measurement would look like Fig. 14 and the ac susceptibility measurement like Fig. 18. But, these measurements were made with damaged samples. Strain free samples resulted in resistance data like Fig. 15 and ac susceptibility data like Fig. 17, both with features inconsistent with the Shumate domain structure.



# Chapter 5

## A Micromagnetic Calculation using Vector Potentials with Ritz Parameters

The models presented in Chapter 4 explain much of the observed behavior of whiskers except in fields near zero. The ac susceptibility measurements show that the ac response is near zero up to a threshold field. The previous models predict values that are much too small compared to the experimentally measured threshold field. The experimental behavior with applied fields and currents can be fitted by treating the parameters of the model as unconstrained by the physics of the model. For example, one way to get a threshold field would be to change the sign of the net wall energy. Another way is to have a sufficiently large residual magnetization. Neither of these is justified on the basis of the models.

The net wall energy results from a close balance between the energy gained from decreasing the (110) 90° walls and the cost of expanding the (100) 90° walls. Domain theory applied to the walls individually leaves no doubt that the wall energy favors expansion. The possibility that a more complete micromagnetic calculation might change the results of Sections 4.3 and 4.4 is investigated in this chapter. A mathematical description of the domain pattern is developed from a vector potential that guarantees the absence of volume charge. The vector potential has several parameters that generate the domain patterns discussed in Chapter 4. These parameters, called Ritz parameters, are varied to minimize the

micromagnetic energy. The results of the calculations are compared with those of the models in Chapter 4.

## 5.1 Vector Potential for a Domain Structure

In this section a vector potential is introduced which satisfies all boundary conditions and results in a domain structure like that in Fig. 2(b). Although this is not a complete solution of the micromagnetic equations, it is used as a starting point. A full consideration of the magnetostatic energy makes it difficult to calculate the total energy. Assume that the avoidance of magnetic volume charges is an over-riding consideration. This condition is met by invoking the constraint that  $\nabla \cdot \vec{M} = 0$  inside the whisker. The argument is that if any magnetic charges existed inside a whisker, the magnetization would relax and move them to surfaces of the whisker.

Charge free configurations have been studied intensively.<sup>19,25,31</sup> The condition for no volume charge is satisfied by a magnetization of the form

$$\vec{M}(\vec{r}) = M_s \nabla \times \vec{A}(\vec{r}) \quad \text{Eq. 5.1.1}$$

where  $\vec{A}(\vec{r})$  is a vector potential inside a magnetic material. The difficulty is the constraint that the magnetization is a vector of constant magnitude, that is,  $(M_s \nabla \times \vec{A}(\vec{r}))^2 = M_s^2$ . This can be overcome as follows. If  $\vec{A}(\vec{r})$  is independent of one of the coordinates and has only one component in the direction of that independent coordinate, then  $M_s \nabla \times \vec{A}(\vec{r})$  produces a magnetization without the component of that independent coordinate. The missing component will be used to

produce a constant magnitude of the magnetization vector.<sup>25,48</sup> For example,  $\vec{M} = M_s \nabla \times \vec{A}(r, \phi, z) = M_s \nabla \times A_\phi(r, 0, z) \hat{\phi}$  in cylindrical coordinates produces a magnetization that has no  $\phi$ -component and does not depend on  $\phi$ . If now we add a component to the magnetization in the  $\phi$ -direction which does not change with  $\phi$ , it will not have a divergence even though it may change with  $r$  and  $z$ . Such a component can be used to produce a vector of constant magnitude.

For rectangular coordinates, the vector potential is chosen as

$$\vec{A}(x, y, z) = A_y(x, 0, z) \hat{y}. \quad \text{Eq. 5.1.2}$$

Then

$$\begin{aligned} M_x &= -M_s \frac{\partial A_y(x, 0, z)}{\partial z} \\ M_z &= M_s \frac{\partial A_y(x, 0, z)}{\partial x} \\ M_y &= \pm (M_s^2 - M_z^2 - M_x^2)^{\frac{1}{2}}, \end{aligned} \quad \text{Eq. 5.1.3}$$

or

$$\vec{M} = M_s (\nabla \times \vec{A}(x, 0, z) \pm \sqrt{1 - (\nabla \times \vec{A}(x, 0, z))^2} \hat{y}). \quad \text{Eq. 5.1.3a}$$

$\vec{M}$  is then a divergenceless vector of constant magnitude. The  $\pm$  sign is important to distinguish two types of solutions that behave in opposite ways for fields applied along the  $y$ -direction.

The resistance and ac susceptibility experiments were done with the pick-up coil at the central cross section of the whisker, its position is  $y=0$ . By symmetry,  $\vec{M}(x, y, z) = \vec{M}(x, -y, z)$ , so that  $\frac{\partial \vec{M}}{\partial y} = 0$  at the central cross section. Away from the central cross section  $\frac{\partial \vec{M}}{\partial y} \neq 0$ , and the solution for the central cross section may not be directly applicable to the problem of the whole whisker. Following the

argument of Heinrich and Arrott,<sup>9</sup> it is assumed that the energy for the whole whisker is proportional to the energy in the central cross section if we take into account the demagnetizing field. Cross sections away from the center are assumed to have magnetization patterns which are similar to that of the central cross section, but modified so as to produce the surface charge that would occur for a square cross section bar of infinite susceptibility. In the case of  $\chi_i = \infty$ , the surface charges produce a demagnetizing field that precisely cancels the applied field. Here it is assumed only that the surface charges produce a uniform field in the central cross section that is proportional to the net magnetization in the  $y$ -direction in the central cross section. The proportionality factor is called the ballistic demagnetizing factor.

The infinite  $\chi$  argument is applicable as long as the magnetization is free to rotate in the  $xy$  plane. To the degree that the anisotropy and the field from the current restrict that motion, the total charges on one half of the whisker are divided between surface charges,  $\vec{n} \cdot \vec{M}$ , and volume charges,  $\nabla \cdot \vec{M}$ , in the ratio of  $4\pi M_s / (H_K + H_I)$ .<sup>36</sup> For an iron whisker  $4\pi M_s = 22 \text{ kG}$ ;  $H_K = 0.55 \text{ kG}$  and  $H_I = 0.17 \text{ kG}$  (for  $I=0.5 \text{ Amp}$  and its cross section  $10 \text{ }\mu\text{m} \times 10 \text{ }\mu\text{m}$ ). Thus  $\sim 97\%$  of the charges are on the whisker surfaces. Then the demagnetizing field is taken to be proportional to the magnetization in the central cross section of a whisker with the same demagnetizing factor as a bar with infinite susceptibility.

We want to describe the domain configuration corresponding to a current sufficient to produce Fig. 2(b). The vector potential is chosen as

$$A_y(x,0,z)\hat{y} = \hat{y} \frac{a}{\sqrt{2}} \left( \log \left( \cosh \frac{x}{a} \cosh \frac{z}{a} \right) - \log \left( \cosh \frac{x-1}{a} \cosh \frac{z-1}{a} \right) - \log \left( \cosh \frac{x+1}{a} \cosh \frac{z+1}{a} \right) \right)$$

Eq. 5.1.4

where  $a$  is a Ritz parameter related to the thickness of the domain walls,  $x$  and  $z$  are normalized distances from the center of the whisker,  $x'/\sqrt{2}d$  and  $z'/\sqrt{2}d$ , respectively, and  $2d$  is the width of the whisker. The variables  $x$  and  $z$  shown schematically in Fig. 30, are used for calculations throughout this chapter. Inserting Eq. 5.1.4 into Eq. 5.1.3 produces the components of the magnetization

$$\begin{aligned} M_z &= 2^{-1} M_s \left( \tanh \frac{x}{a} - \tanh \frac{x-1}{a} - \tanh \frac{x+1}{a} \right) \\ M_x &= -2^{-1} M_s \left( \tanh \frac{z}{a} - \tanh \frac{z-1}{a} - \tanh \frac{z+1}{a} \right) \\ M_y &= \pm M_s \sqrt{1 - (M_x^2 + M_z^2) / M_s^2}. \end{aligned} \quad \text{Eq. 5.1.5}$$

The  $y$ -component of the magnetization is shown in Fig. 31 for  $a=0.02$ . The magnetization is directed along the principal axis not only at the center but also at the corners. Most of the magnetization inside the domains lies in the cross section and is directed along an easy axis of the whisker.

As indicated before, Brown's equations are non-linear differential equations.<sup>24</sup> Many solutions are possible for any specific geometry. It is believed that Eq. 5.1.5 approximates one of the solutions for a whisker. The domain walls have an even thickness except near magnetic singularities. As explained in Section 4.3, the thickness of the walls is determined by competition among the energy from the applied current, the exchange energy and the anisotropy energy. By plotting, for example,  $M_z$  in Eq. 5.1.5 versus  $x$ ,

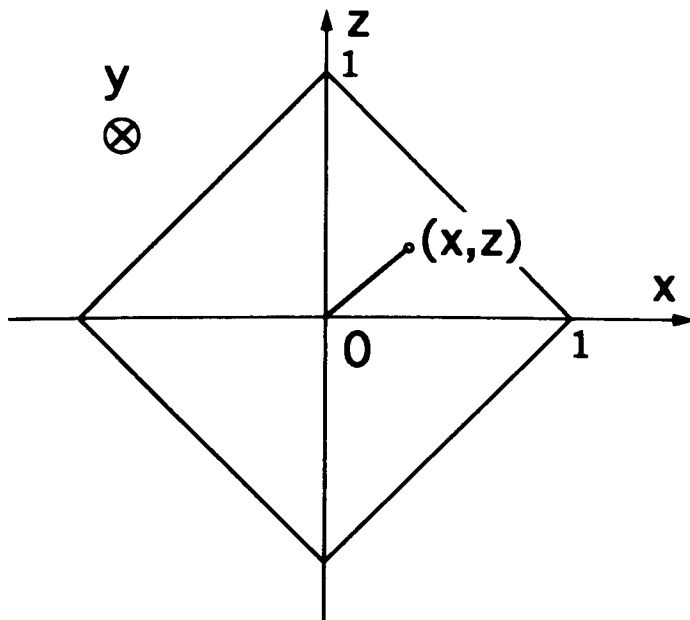


Fig. 30. Schematic diagram for model calculations.  $x$  and  $y$  are normalized distances from the center of a whisker.

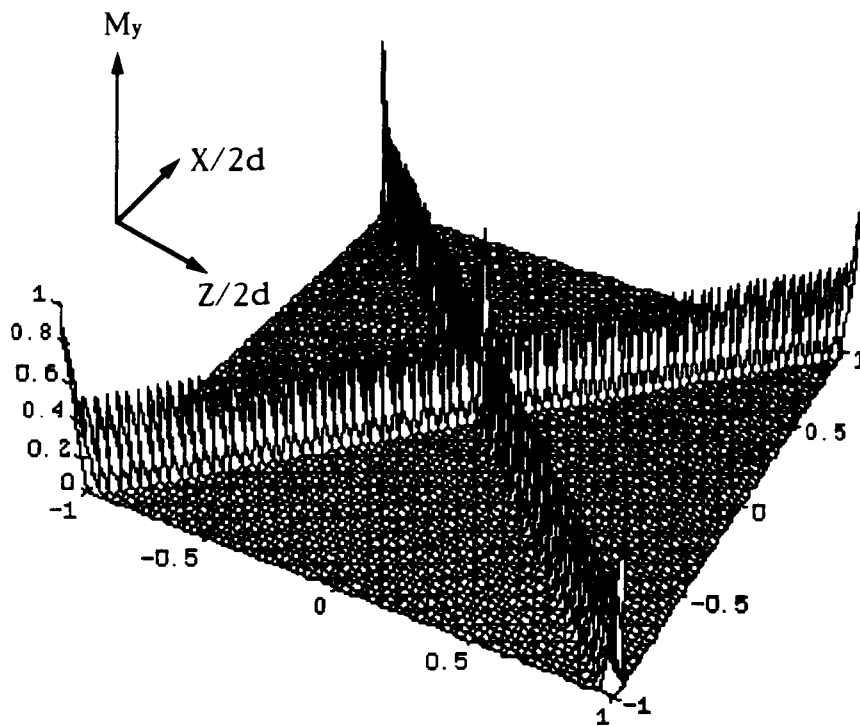


Fig. 31. The calculated  $y$ -component of the magnetization for the cross section of a whisker with  $a=0.02$ .

it is easily shown that the parameter  $a$  is linearly related to the thickness of (110) 90° domain walls.

Minimization of the total energy results in a stable domain structure. The assumed charge free configuration means that the magnetostatic energy can be ignored. The energy from an applied current and the anisotropy energy are defined in Chapter 2.

However, a different form of the exchange energy as suggested by Arrott, Heinrich, and Bloomberg,<sup>49</sup> is

$$E_{ex} = \frac{C}{2M_s^2} \int_V d\tau \{ (\nabla \cdot \vec{M})^2 + (\nabla \times \vec{M})^2 \}, \quad \text{Eq. 5.1.6}$$

where  $C = 2 \times 10^{-6} \text{ erg/cm}$ .  $C$  is equal to  $2A_{ex}$  in Eq. 2.1.2. Since our vector potential is based on the volume charge free configuration ( $\nabla \cdot \vec{M} = 0$ ), the exchange energy is then

$$E_{ex} = \frac{C}{2M_s^2} \int_V (\nabla \times \vec{M})^2 d\tau. \quad \text{Eq. 5.1.6a}$$

The first term of the anisotropy energy, from Chapter 2, is

$$E_K = \int_V K_1 (\alpha^2 \beta^2 + \alpha^2 \gamma^2 + \beta^2 \gamma^2) d\tau \quad \text{Eq. 2.1.8a}$$

where  $K_1 = 4.7 \times 10^5 \text{ erg/cm}^3$ .

The total energy can be expressed as

$$E_{tot} = \int_V d\tau \left\{ \frac{C}{2M_s^2} (\nabla \times \vec{M})^2 + K_1 (\alpha^2 \beta^2 + \alpha^2 \gamma^2 + \beta^2 \gamma^2) - \vec{H}_I \cdot \vec{M} \right\} \quad \text{Eq. 5.1.7}$$

where  $\vec{H}_I$  is the magnetic field from the applied current. Parameters used for the calculation are given in Table 3. The applied current is 100 mA and the width of the whisker is 50  $\mu\text{m}$ . Most of the exchange and anisotropy energies are produced near domain walls. Variable grids are used to calculate Eq. 5.1.7 and make it possible to obtain the

energies near the walls and the magnetic singularities with high precision.

Table 3. Parameters used in the calculations for a <100> iron whisker at room temperature.

Defining Parameter	Symbol	Value
Saturation Magnetization	$M_s$	1715 emu/cm <sup>3</sup>
Anisotropy Energy per unit volume	$K_1$	4.7x10 <sup>5</sup> erg/cm <sup>3</sup>
Exchange Constant	$C(=2A_{ex})$	2x10 <sup>-6</sup> erg/cm

The result of the minimization is shown in Fig. 32; when the parameter  $a$  increases, the anisotropy energy increases linearly but the exchange energy decreases rapidly. The exchange energy is equal to the anisotropy energy at the minimum. The energy from the applied current is not changed very much for the small parameter  $a$ . The total energy per unit length is 0.0168 erg/cm and the corresponding parameter  $a$  is 0.000476 ( $2ad/\sqrt{2} = 168 \text{ \AA}$ ). The wall energy density, which consists of the exchange and the anisotropy energy densities, is 1.19 erg/cm<sup>2</sup> at the energy minimum. The energy density for the (110) 90° wall is similar to the 1.18 erg/cm<sup>2</sup> wall energy, calculated by Aharoni and Jakubovics.<sup>50</sup> The parameter  $a$  is related linearly to the thickness of the (110) 90° domain wall.<sup>51</sup> The y-component of the magnetization increases from 0 to  $1/\sqrt{2} M_s$ , and then decreases back to 0 while crossing the 90° wall. The thickness of the domain wall is defined as  $6ad/\sqrt{2}$  (=505 Å) which is



the distance over which the  $x$ - or  $z$ -components of the magnetization change from  $+0.9M_s/\sqrt{2}$  to  $-0.9M_s/\sqrt{2}$ .

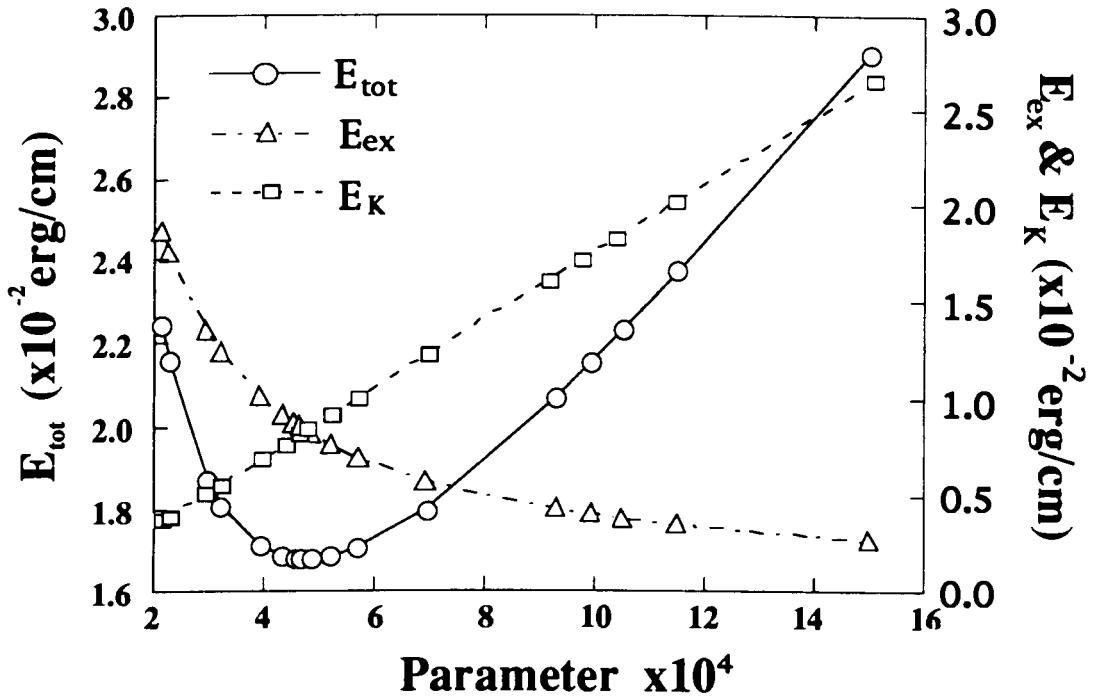


Fig. 32. Minimization of the total energy with  $2d=50 \mu\text{m}$  and  $I=100 \text{ mA}$  at minimum,  $E_{\text{tot}}=1.68 \times 10^{-2} \text{ erg/cm}$  and  $a=4.76 \times 10^4$ .

## 5.2 Modification of the Vector Potential

The vector potential suggested in the previous section satisfies all boundary conditions. But it is not a solution of the micromagnetic equations. It has only a single Ritz parameter which determines both the wall thickness and the extent of the regions of magnetization along the  $y$ -axis in the center and at the four corners. In this section, we modify the vector potential to produce a domain structure in

which the volume of the regions with magnetization along the  $y$ -axis can change independently from the wall parameter  $a$ .

The modified vector potential is based on the characteristics of a  $\text{coth}$ -function. The function  $\text{coth}(\frac{b}{x})$  varies slowly when  $x$  is smaller than  $b$ . After  $x$  becomes larger than  $b$ , the function increases linearly with  $x$ . If the function is changed to  $(\text{coth}(\frac{b}{x})^k)^{\frac{1}{k}}$ , when  $x$  is smaller than  $b$  the function will be more constant as  $x$  approaches to  $b$  for larger  $k$ . When  $x$  is larger than  $b$ , linear increase of the function with respect to  $x$  starts closer to  $b$  for larger  $k$ . The function and its derivative are illustrated with  $k=1, 2$ , and  $5$  in Fig. 33 for  $b=0.2$ .

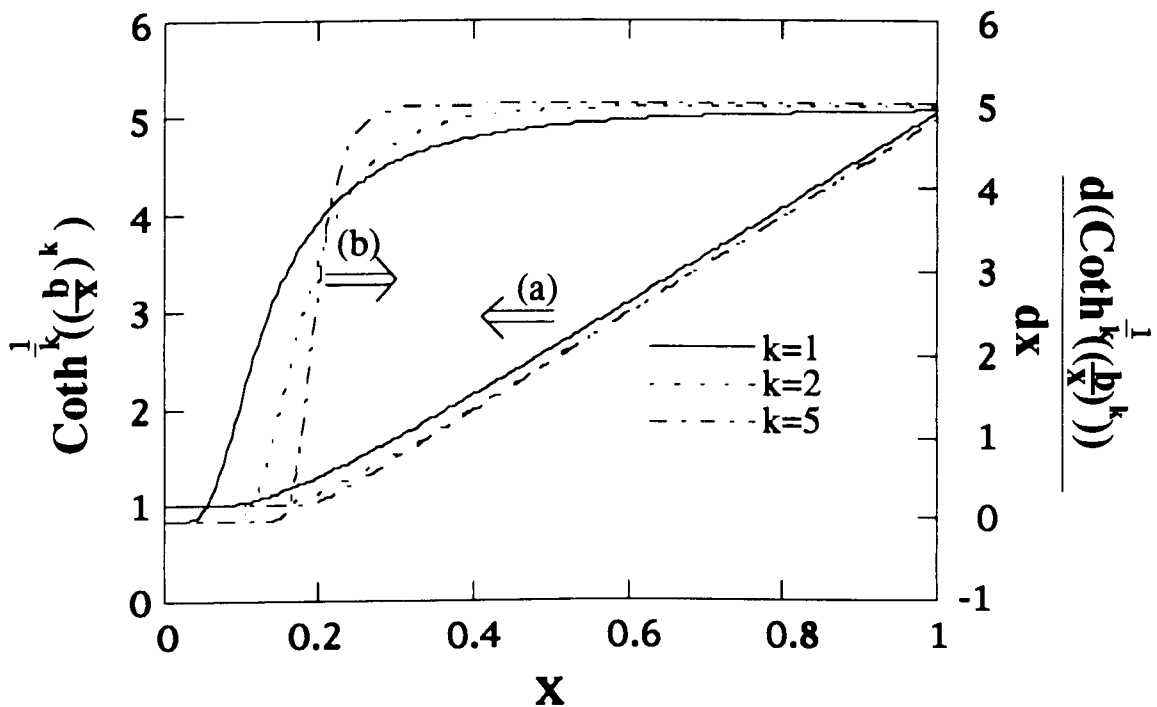


Fig. 33. Characteristic behavior of the  $\text{coth}$ -function for  $b=0.2$ .

The magnetization rapidly changes its direction when passing through the (100)  $90^\circ$  domain wall and the magnetization lies along

the easy axis inside of a domain on the cross section of the whisker. That is, there are no  $x$ - or  $z$ -components of the magnetization in the central domain surrounded by the walls with  $\{100\}$  planes and these components increase rapidly on passing through the wall. The behavior of the derivatives of the  $\coth$ -function is similar to the behaviors of  $x$ - and  $z$ -components of the magnetization. Fig. 33 shows the derivative of the function with  $k=1, 2,$  and  $5$ .

The modified vector potential is

$$\begin{aligned} \bar{A}(x, y, z) = A_y(x, 0, z)\hat{y} = \hat{y} \left\{ h \coth^{\dagger} \left( \frac{2^{\dagger} h}{a \log(\cosh \frac{x}{a} \cosh \frac{z}{a})} \right)^{\dagger} \right. \\ \left. - \frac{a}{\sqrt{2}} \log \left( \cosh \frac{x-1}{a} \cosh \frac{z-1}{a} \right) - \frac{a}{\sqrt{2}} \log \left( \cosh \frac{x+1}{a} \cosh \frac{z+1}{a} \right) \right\} \end{aligned}$$

Eq. 5.2.1

where  $a$ ,  $h$ , and  $k$  are Ritz parameters. The Ritz parameters are varied to minimize the total energy.<sup>16,48</sup> As explained in the previous section, the last two terms are added to avoid surface charges at the corners. The modified vector potential still satisfies  $\nabla \cdot \bar{M} = 0$  inside the whisker. There is a completely negligible surface charge density produced by the exponential tail of the first term. But there are no net surface charges in the midplane.

Before considering minimization of the total energy, the form of the magnetization resulting from the vector potential of Eq. 5.2.1 is shown in Fig. 34. In Figs. 34(a) to (d) the contour plots of the  $y$ -component of the magnetization,  $M_y$ , are shown when the parameters  $a$ ,  $k$ , and  $h$  are set to the values:

Fig. 34	a	k	h
a	0.02	10	0.2
b	0.01	10	0.2
c	0.02	5	0.2
d	0.02	10	0.1

Lines of equal values of  $M_y$  are shown as the edges of strips across which  $M_y$  decreases by 10% of the saturation magnetization. The magnetization is directed along the axis of the whisker at its center and at its corners. In the four domains, the magnetization lies in the cross section of the whisker and parallel to its surface. Fig. 34 shows that the parameter  $a$  determines the thickness of (110)  $90^\circ$  domain walls. The parameters  $k$  and  $h$  are related to the thickness of (100)  $90^\circ$  walls and to the size of the central domain. The central domain becomes larger as the parameter  $h$  increases. The thickness of a (100) domain wall for a given  $h$  is determined by  $k$ . A large  $k$  makes the magnetization change rapidly near the (100)  $90^\circ$  wall. For the inner wall to maintain a constant width with increasing  $h$ , it is necessary to also increase  $k$ .

A simple form for the demagnetizing energy in the midplane will be used here. Away from the central cross section, the whisker can not have a charge-free configuration due to the  $y$ -component of the magnetization. A net  $y$ -component of the magnetization in the midplane gives rise to magnetic charges on surfaces away from the midplane. These charges result in a demagnetizing field. The total energy consists of the exchange energy, the anisotropy energy, the magnetic field energy from the applied current, and the magnetostatic energy. We recall that the energy due to the

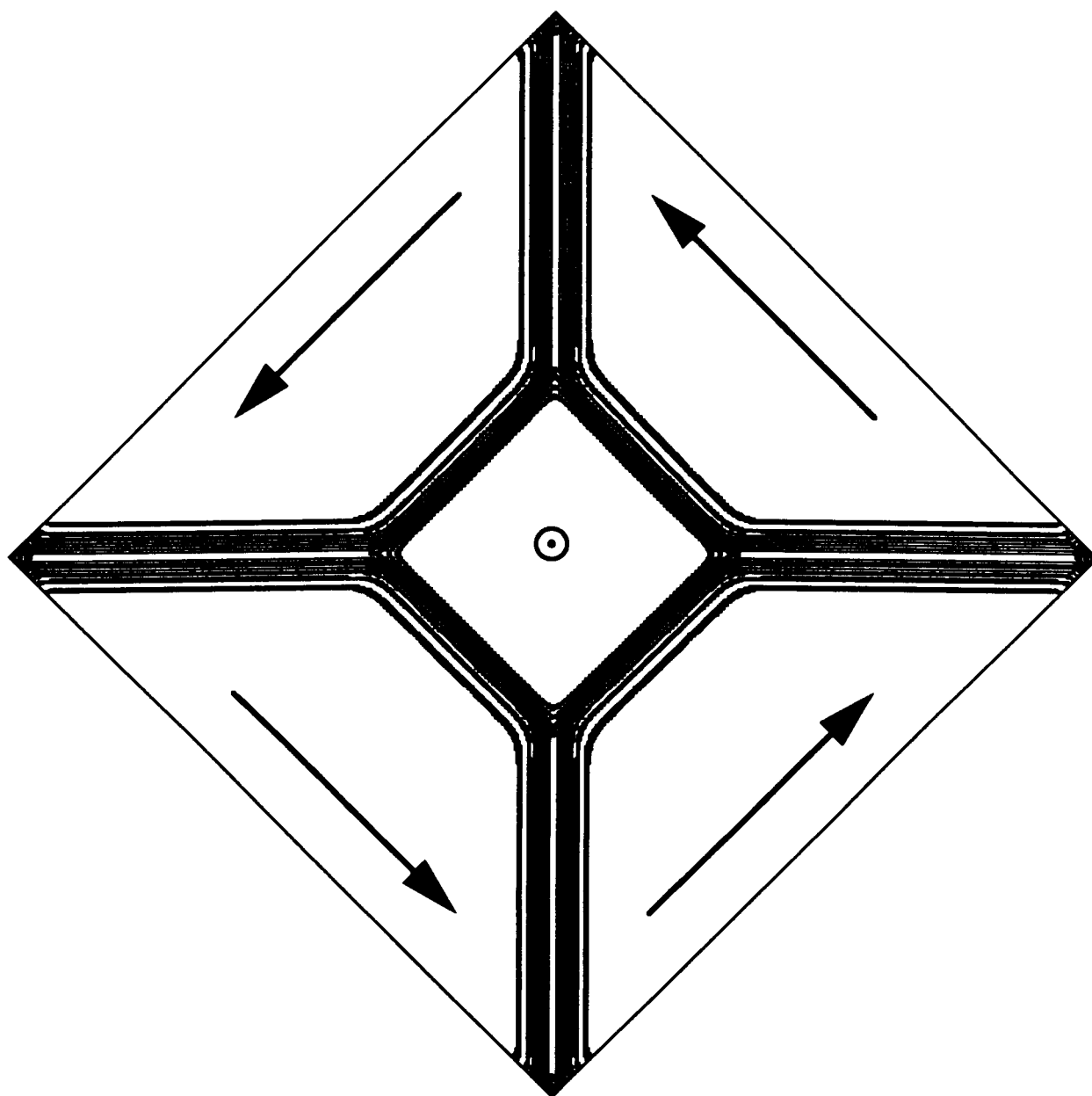


Fig. 34(a). Contour plot of the y-component of the magnetization with  $a=0.02$ ,  $k=10$ , and  $h=0.2$ .

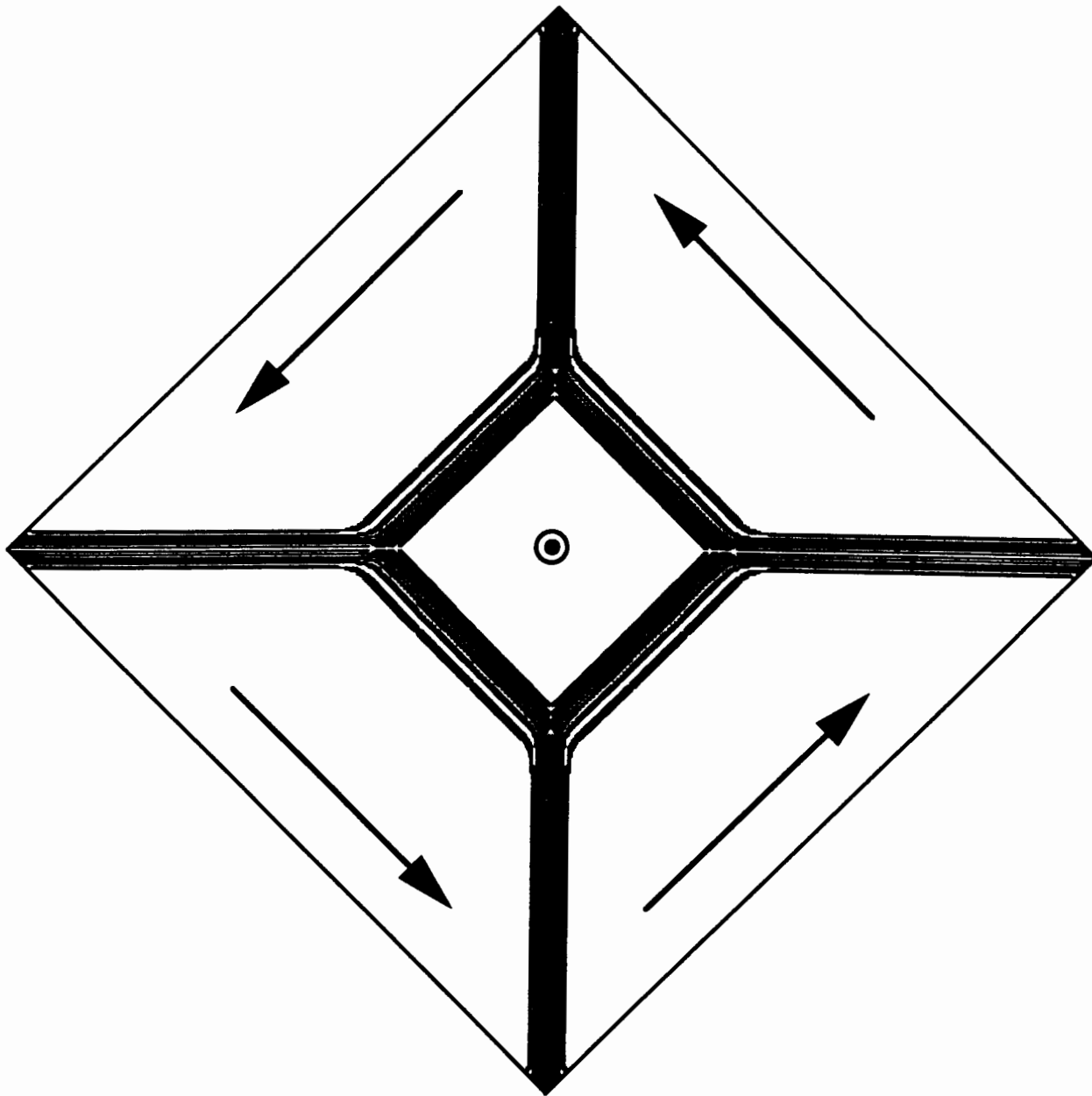


Fig. 34(b). Same as Fig. 34(a) with  $a=0.01$ ,  $k=10$ , and  $h=0.2$ .

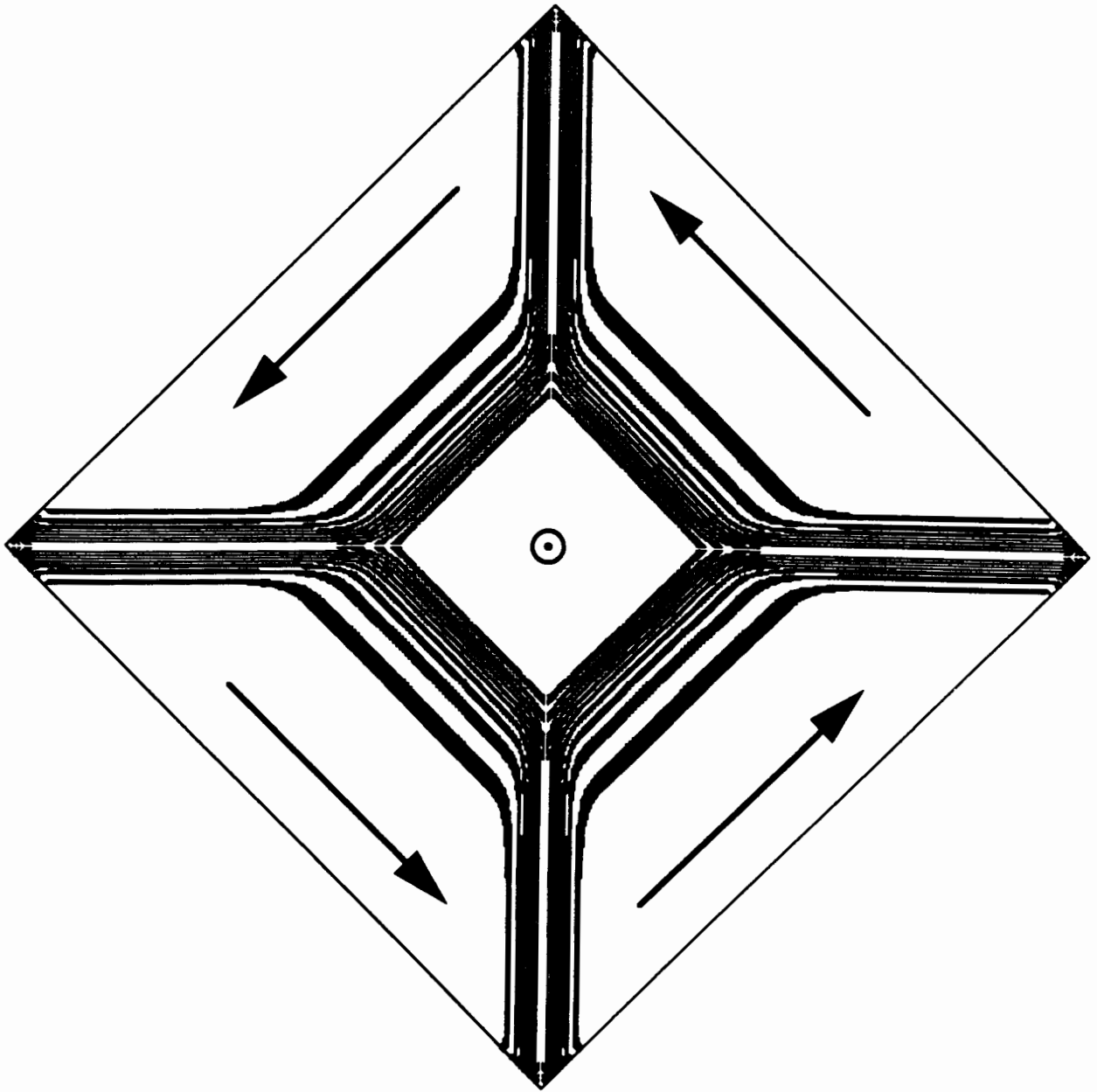


Fig. 34(c). Same as Fig. 34(a) with  $a=0.02$ ,  $k=5$ , and  $h=0.2$ .

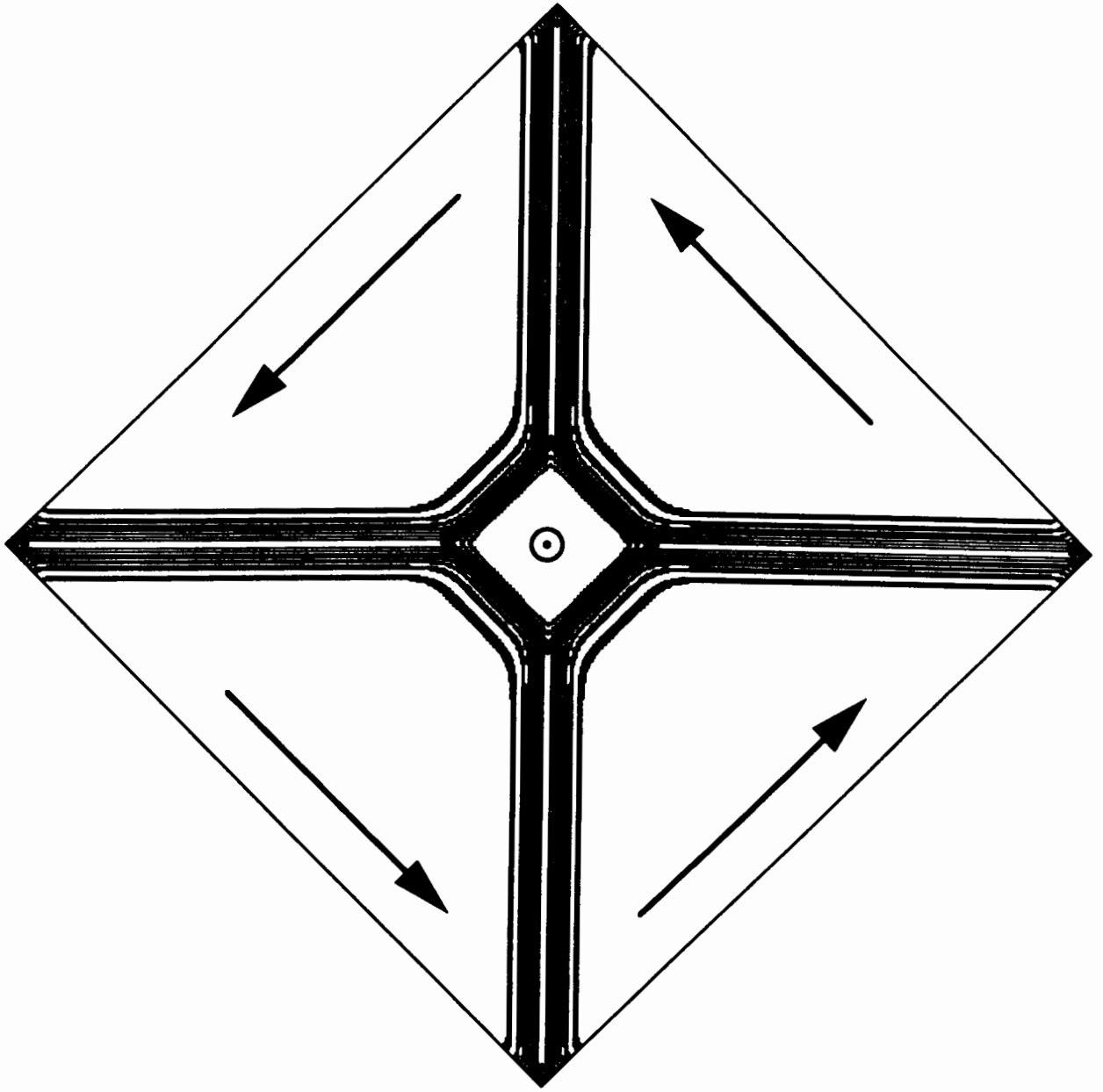


Fig. 34(d). Same as Fig. 34(a) with  $a=0.02$ ,  $k=10$ , and  $h=0.1$ .



demagnetizing field,  $H_D$  in the midplane is approximated as

$$E_D = -\int_V \frac{1}{2} \vec{M} \cdot \vec{H}_D d\tau = 2\pi D \int M_y^2 d\tau = 2\pi D \langle M_y \rangle^2 A_y L \quad \text{Eq. 2.1.7a}$$

where  $D$  is the ballistic demagnetizing factor,  $A_y$  is the cross section of the whisker, and  $L$  is its length. Bloomberg derived a formula for the demagnetizing factor of a rectangular bar as<sup>36</sup>

$$D = \frac{4}{\pi} \left( \frac{2d}{L} \right)^2 \left[ \log \frac{L}{2d} - 1.099 \right] \quad \text{Eq. 2.3.4}$$

where  $2d$  is the thickness of the bar. The whiskers we used in the experiments typically have  $2d/L \approx 0.02$ .

Most of the magnetization is along the easy axes of a  $\langle 100 \rangle$  iron whisker except near domain walls where most of exchange and anisotropy energies are concentrated. A new grid system is suggested in Fig. 35. Details of the grid system and the program used for the calculations are explained in Appendix. The grid is designed to calculate the energies in detail near the walls. The grid covers only one eighth of the cross section. For the square symmetry of the magnetization configuration this is sufficient to obtain the total energy.

Initially, the wall parameter ( $a=0.0078$ ) was fixed to investigate the extent to which changing  $h$  and  $k$  affect the energy. The total energy was minimized with respect to  $h$  and  $k$  both with and without an applied current. Initially the parameter  $k$  was constrained to be an integer. This restriction was relaxed later. The width of the whisker used for the calculation was  $2.5 \mu\text{m}$  in order to reduce the error in the numerical calculations. If the size were larger than this width, it was very hard to integrate properly the *coth*-function.

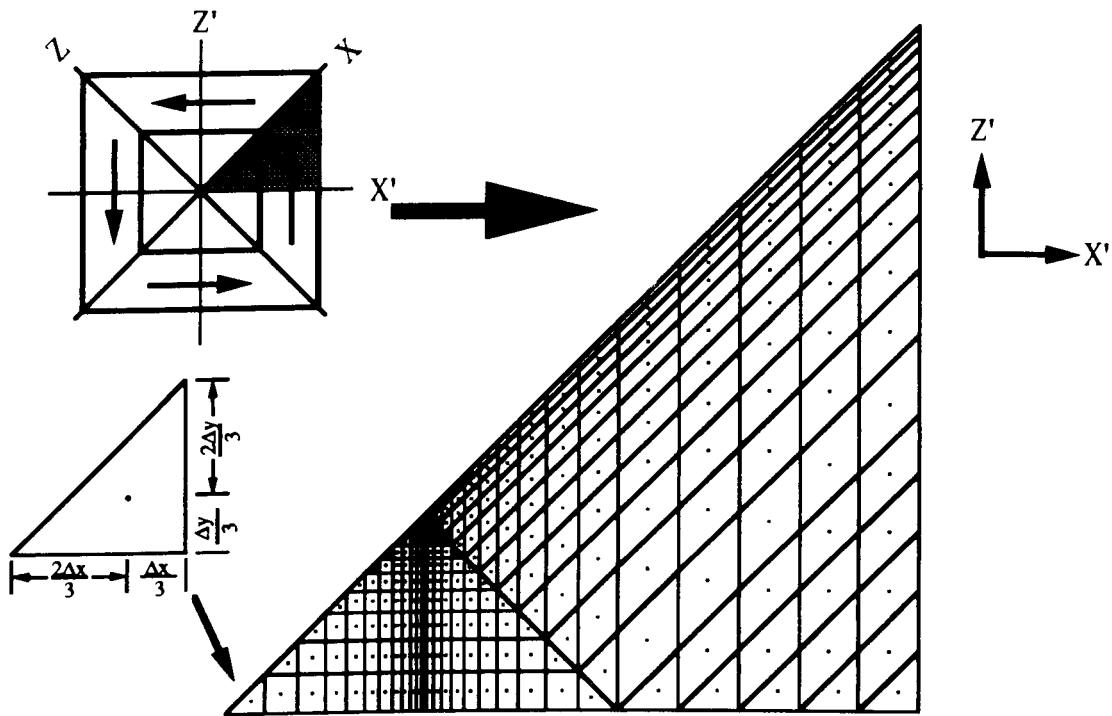


Fig. 35(a). A new grid system for 90° walls with a (100) plane and a (110) plane covering an eighth of the cross section.

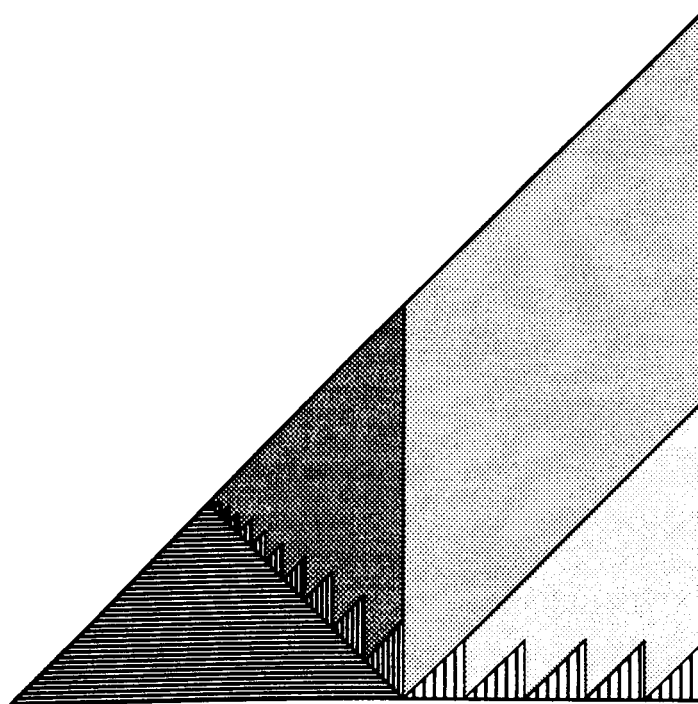


Fig. 35(b). Six different regions are shown for the new integral system.

The result for  $I=0$  mA is shown in Fig. 36(a). Fig. 36(b) is for  $I=250$  mA. Each of the points in Figs. 36(a) and (b) represents a minimum energy for a given  $k$  as  $h$  is varied. The figures show that  $h$  and  $k$  are almost linearly related to each other. Fig. 36(a) shows that the minimum of the total energy occurs when  $h=0.0822$  and  $k=9$ . The central domain does not disappear completely even when the applied current is large, as in Fig. 36(b). The modified vector potential prefers the domain structure shown in Fig. 2(c) even with large applied current. As discussed in Chapter 4, the demagnetizing energy and the energy from the current are balanced by the wall energy. The area of the domain at the center decreases very little for this large current. The minimum of the total energy for  $I=250$  mA has Ritz parameters  $h=0.0627$  and  $k=7$ . The corresponding energy per unit length is  $-2.068 \times 10^{-4}$  erg/cm. The total energy calculated with the modified vector potential is lower than the energy recalculated for the original vector potential, Eq. 5.1.4, using the same size of the whisker and same current. Eq. 5.2.1 goes over to Eq. 5.1.4 in the limit as  $h \rightarrow 0$ .

When the parameter,  $k$ , is allowed to take on non-integer values, the minimum energy configuration does not change much. Then the parameters corresponding to the minimum energy are  $a=0.0078$ ,  $h=0.0629$ , and  $k=7.66$ . The corresponding energy density is  $-2.07 \times 10^{-4}$  erg/cm.

The  $90^\circ$  wall energies lying in a (100) plane and a (110) plane are calculated from the given vector potential. The magnetostatic energy from the wall is assumed to be small so that the exchange and anisotropy energies are dominant.<sup>49</sup> The minimization of the total

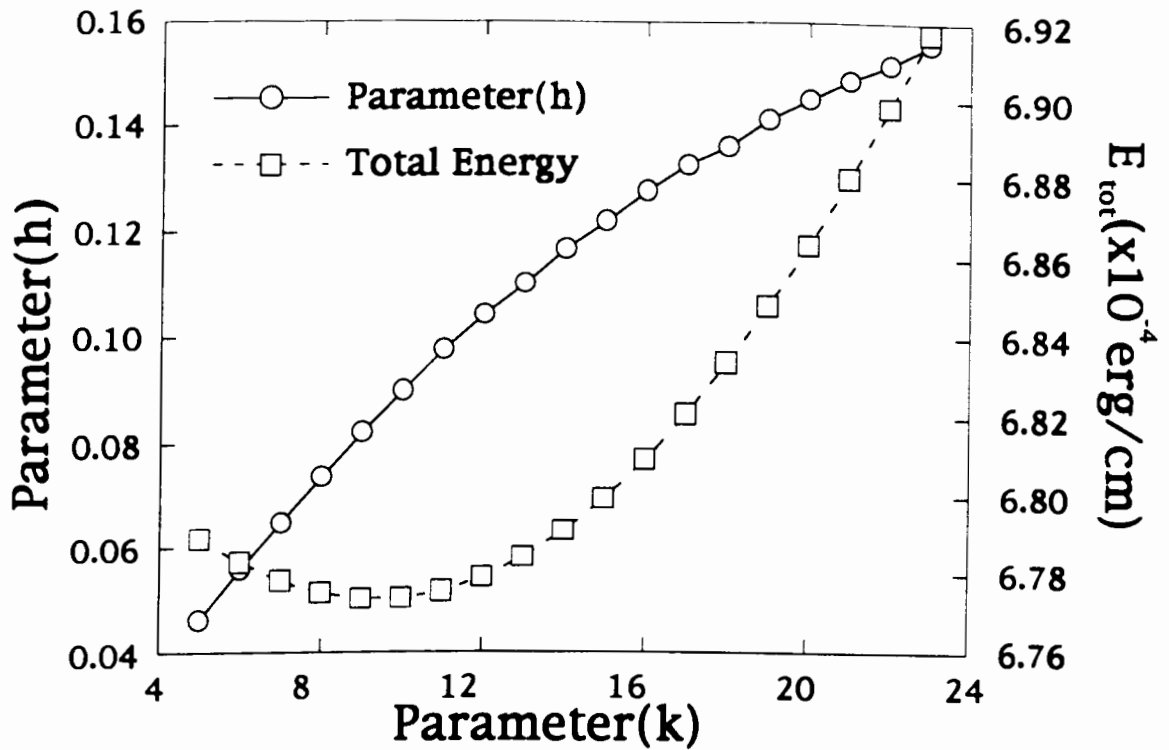


Fig. 36(a) Results of the minimization with  $a=0.078$ ,  $2d=2.5$  nm, and  $I=0$  mA.

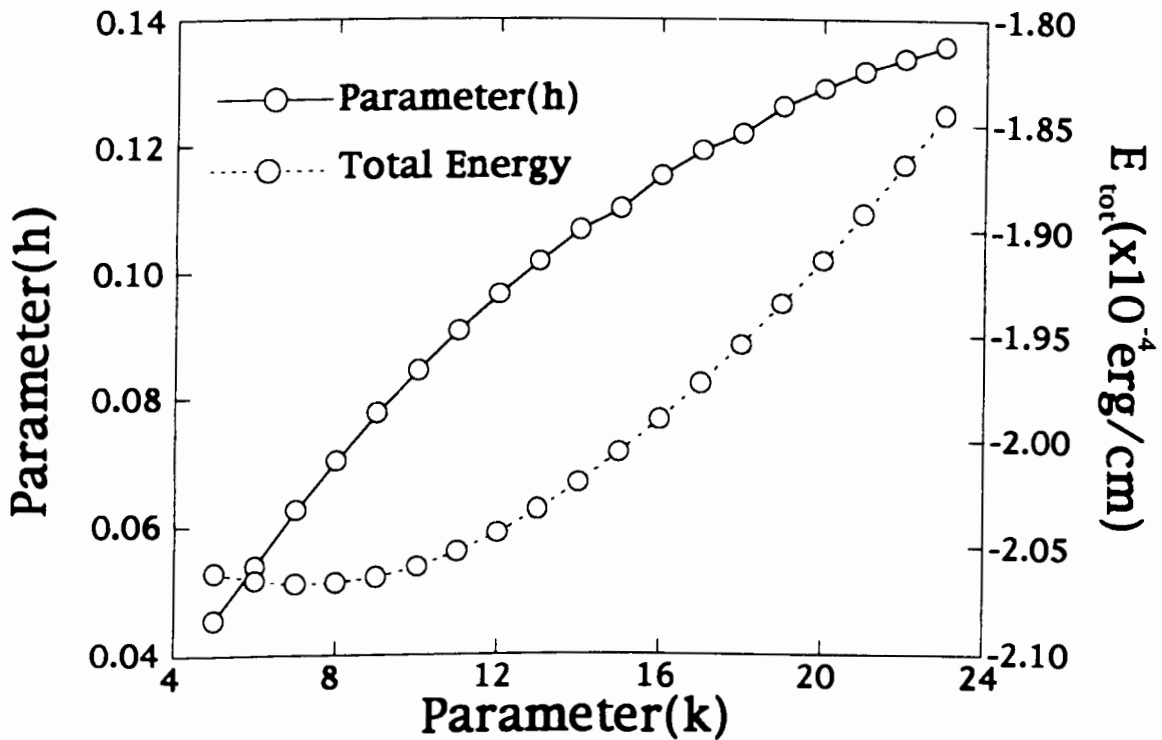


Fig. 36(b) Same as Fig. 36(a) with  $I=250$  mA.

energy for a given  $h$  gives the dependence of  $k$  and  $a$  on  $h$ . The wall energy density is calculated by directly integrating the wall energy across the wall at constant  $z$  or constant  $x$  for a (110) plane and  $x=z$  or  $x=-z$  for a (100) plane. The (110) 90° wall energy is 1.18 erg/cm<sup>2</sup>, and the one for a (100) plane is 0.74 erg/cm<sup>2</sup>. The new model also shows the (110) 90° wall has the same energy density calculated in the previous section. But the energy density of the (100) 90° wall is about 9 % larger than the expected energy density,<sup>18</sup>

$\sigma_{90^\circ} = 0.68 \text{ erg / cm}^2$ . The vector potential does not appear to describe the (100) 90° wall with sufficient accuracy.

Now the above model is compared with that suggested in Section 4.3. The previous model predicts the existence of the small central domain without external field. The refined model also shows that a whisker has a small central domain; i.e., about 8.2% of the width of the small whisker used for the calculation for zero applied field. The size remains about the same for a larger whisker which means that it is a very small effect in the larger whisker. Both models show that the demagnetizing energy prevents the central domain from moving out towards the surfaces of the whisker.

### 5.3 Magnetization Processes

In this section, the magnetization processes under the influence of external fields and applied currents are discussed. The experimental results indicate that, when the external field is applied in the direction of the magnetization, a small field is sufficient to expand the central domain which is surrounded by (100) 90° domain

walls. But, the external field must be larger than the renucleation field to change the central domain when the direction of the field is opposite to the magnetization. We will only explain the magnetization process when the external field is in the same direction as the magnetization. Because the field from the current is smallest at the central core it is easy to expand the core by applying the field along the axis in the preferred direction. As the central domain becomes larger surface charges are generated.

The competition among energies results in nucleation of a central domain when the external magnetic field is stronger than the collapse field. When the total energy is minimized to find a stable structure for a given external field, it is not necessary to consider line singularities at the corners which are not involved in the competition. The growth of the corner singularities is suppressed by the field from the current. To model magnetization processes, the vector potential is modified to

$$\bar{A}(x, y, z) = A_y(x, 0, z)\hat{y} = \hat{y}h \coth^{\frac{1}{2}} \left( \frac{2^{\frac{1}{2}}h}{a \log(\cosh \frac{x}{a} \cosh \frac{z}{a})} \right)^{\frac{1}{2}}.$$

The vector potential behaves like the one defined in the previous section except for the corners. The external field changes the width of the domain at the center and the thickness of the (100) 90° domain wall. The relation between the central domain width and the wall thickness while applying an external field is found by minimizing the total energy.

The vector potential has three unknown Ritz parameters. The parameter  $a$  is fixed at  $a= 0.0078$ , the value at the minimum energy

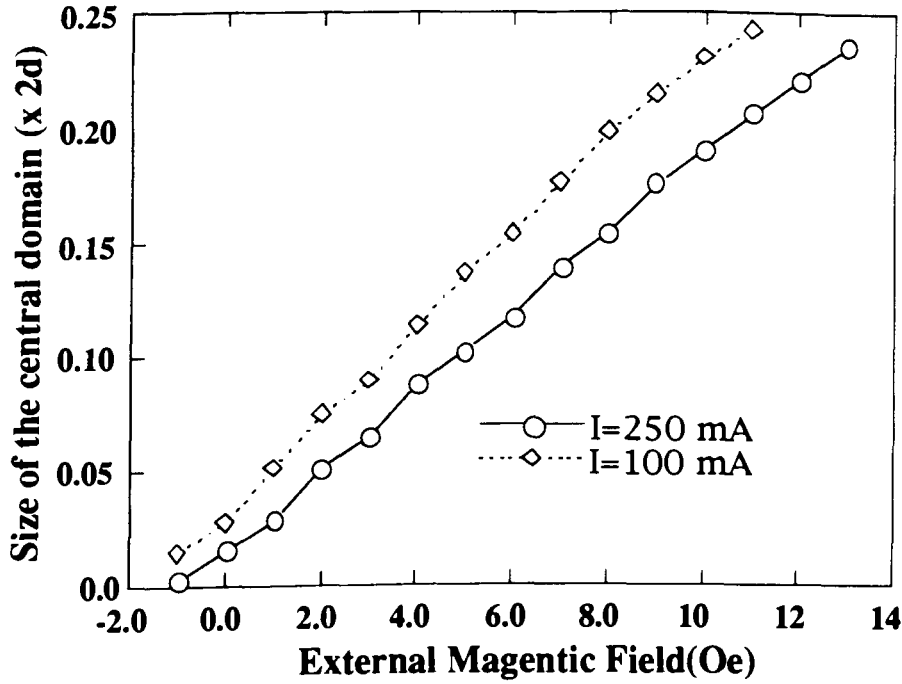


Fig. 37. Relation between external field and the size of the central domain while applying currents  $I=100$  and  $250$  mA.

found in Sections 5.1 and 5.2. As indicated in the previous section, the parameter  $a$  is only related to the thickness of the (110)  $90^\circ$  wall. This parameter is not involved in magnetization processes near the central domain. Another choice of  $a$  would not affect the magnetization behavior of the central domain. The energy from the external field is added to give the total energy, as defined in Chapter 2. The energy from the external field is approximated by the energy at the central cross section and is written as

$$E_H = -\int_V \vec{H}_o \cdot \vec{M} d\tau = -\langle M_y \rangle H_o A_p L, \quad \text{Eq.2.1.9a}$$

where  $\langle M_y \rangle$  is the  $y$ -component of the magnetization averaged over the cross section, and  $A_p$  is the cross section of a whisker. The external magnetic field,  $\vec{H}_o = H_o \hat{y}$ , is parallel to the longitudinal

direction of the sample and it is assumed to be uniform inside the whisker.

The assumed whisker dimensions are  $2d/L = 0.02$  and  $2d = 2.5 \mu\text{m}$ . The fundamental constants used in the calculation are shown in Table 3. For applied currents of 100 mA and 250 mA, the results of the minimization are shown in Fig. 37. Increasing external magnetic field results in an increasing parameter  $h$ , which is linearly related to the size of the magnetic domain surrounded with  $\{100\}$  planes. Fig. 37 indicates that a stronger magnetic field is required to obtain a given magnetization or central domain size while applying a larger current. From Fig. 37, the departure field for  $I = 250$  mA is expected to be larger than the field for  $I = 100$  mA.

When a magnetic field is applied, the width of the domain increases. The contour plot of the  $y$ -component of the magnetization while applying the current (100 mA) and the external field (8 Oe) is shown in Fig. 38. This domain structure is similar to the deduced structure in Chapter 4.

The behavior from points (f) to (g) in Fig. 19 can not be explained using either the previous models in Chapter 4 nor the refined calculation in this chapter. The large  $m_0$  invoked in Chapter 4 to explain the small  $\chi$  in small fields can not be justified by the refined calculation. The renucleation process at point (g) in Fig. 19 can not be understood within the context of either model. It is most likely the result of nucleation processes away from the central cross section. Similarly, the explanation of the apparent value of  $m_0$  may be due to processes away from the central cross section.



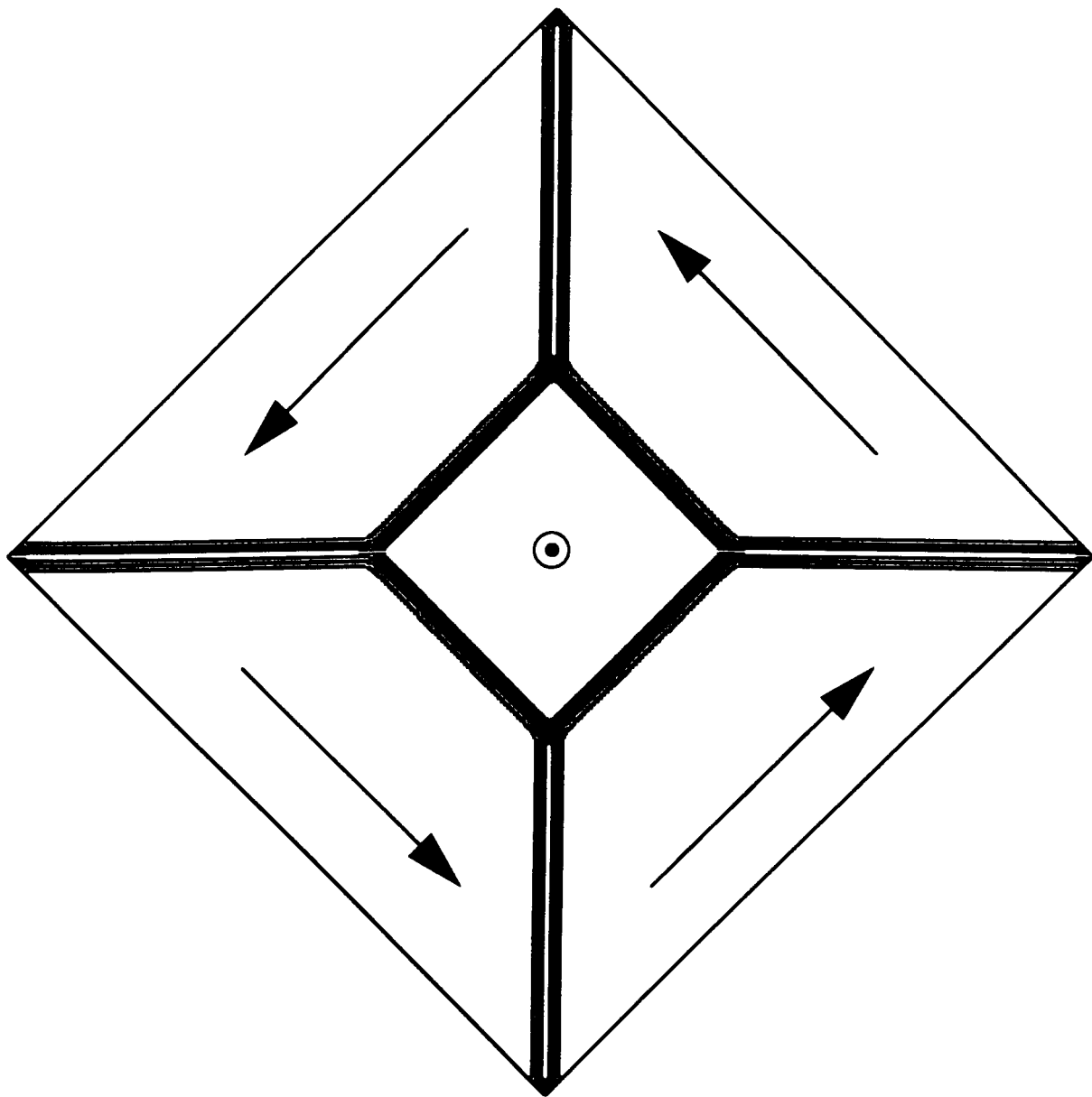


Fig. 38. Contour plot of the  $y$ -component of the magnetization while applying current  $I=100$  mA and external field  $H=8$  Oe.

The assumption underlying the models in Chapters 4 and 5 is that the behavior in the whole whisker can be modeled by considering only the central cross section. The demagnetizing field is assumed to depend only on the magnetization of the central cross section and the geometry of the whisker. This seems to work well for all but the low field region. To go beyond this basic assumption brings into play the full integro-differential equation aspects of micromagnetics. As mentioned earlier, there are no complete solutions to complicated problems such as the low field behavior.

## Chapter 6

### Conclusion

The effect of current and/or external field on a <100> iron whisker has been studied. Our resistance and ac susceptibility experimental results do not support the domain structure suggested by Shumate *et al.* which in the presence of sufficient current has a central domain containing a 180° domain wall. We conclude from our measurements that there is no such central 180° domain wall. There is a central domain which is very small in the presence of a sufficient current. This domain is too small to affect the resistance and ac susceptibility measurements unless sufficient field is applied in the proper direction. The experimental results indicate the following features;

- a) the Landau domain structure at zero field is not changed with the applied current less than critical,
- b) the domain structure collapses with a small central domain when the applied current is larger than critical,
- c) the growth of that domain depends on the direction of the external field relative to the direction of the magnetization of that domain,
- d) that small central domain grows easily when a field is applied along the direction of its magnetization ,
- e) with the reversed external field that domain remains unchanged until the external field becomes larger than a renucleation field, and

f) the saturation field for the central cross section of the whisker increases with the increase of the applied currents.

The experimental data are explained with a sequence of deduced domain structures. The suggested models in Sections 4.3 and 4.4 account for changes in the in-phase and out-of-phase ac signals with changes in field and current. The calculated magnetic responses for most of the external fields agree very well with the experimental data. The experimental data show the magnetic responses disappear before the field reaches zero field. But the calculated ac magnetic response for low field does not disappear until negative fields are applied. The ac magnetic response for low field is not fully understood with our models. A positive wall energy or a large residual magnetization might have explained this discrepancy. Detailed micromagnetic calculation was carried out to investigate these possibilities. These did not give us an explanation of the low field behavior. The stability of the deduced domain structure is verified with the micromagnetic calculation and the sign of the wall energy is definitely not positive. While most of the experimental results are explicable using the calculation based on the micromagnetics and Maxwell's equations, the low field behavior remains to be explained.

## Appendix Grid System

The micromagnetic energies are largest near walls. A new grid system is designed to reduce the numerical calculation errors by calculating the energies in detail near the walls. The (110) 90° wall is along the hypotenuse in Fig. 35(a) and the (100) 90° wall is inside the right angled triangle and perpendicular to a (100) plane. The position of the wall lying in a (001) plane is found by the magnitude of the  $y$ -component of the magnetization is valued between  $0.69M_s$  and  $0.72M_s$ .

The grid for the integral is shown in Fig. 35(a) and it covers one eighth of the cross section of the whisker. The dot inside each cell indicates the position where the energy density is calculated. The energy for each cell is calculated as the product of the energy density and the area of the cell. The total energy is the sum of the individual cell energies

The grid system has six different regions as illustrated in Fig. 35(b). The first region, having a triangle shape, is for calculating energies near the (100) 90° wall which is located at the center of the region. The energy densities are calculated at the center of each rectangle inside this triangle. Inside the small triangles, the energy density is calculated at the position demonstrated in the insert in Fig. 35(b). In the second region the energy density is calculated at the situation as in the first region. The third, fourth, and fifth

regions are parallel to the wall lying in the (101) plane and the energy density is calculated at the center of each parallelogram. The cell size is made large as the calculation points move away from the wall. The energy density in the last region is as above.

The program "MINUIT" from CERN libraries uses FORTRAN to minimize the total energy with a Ritz method. FCN, the user-written subroutine, calculates the value of the function to be minimized. The subroutine is as follows

```

C      main program for calling MINUIT
C      external parameters are read from the file 'RITZPAR'
C..    output is defined when the program starts.
      EXTERNAL FCN
      OPEN(5,FILE='RITZPAR',STATUS = 'OLD')
      CALL MINUIT(FCN,0)
      STOP
      END

C..    program for calculating the total energy
C..    only calculating one eighth of the cross section
      SUBROUTINE FCN(NPAR, G, FF, FX, IFLAG)
      IMPLICIT REAL*8(A - H,O - Z)
      REAL*8 MAGX
      COMMON /MN7EXT/ U2(30)
      LOGICAL*1 NAM
      LOGICAL LFCN / .FALSE. / , BATCH
      LFCN = IFLAG .EQ. 3

C..    reading the initial parameter ( IFLAG =1)
      IF (IFLAG .NE. 1) GO TO 20
      DELKA = 1D0
      LUNW1 = 6
      LUNW2 =7
      LUNR1 = 5
      NPARM = NPAR

C      parameter for a <100> iron whisker
C..    satma :saturation magnetization: exco;exchange coefficient
C..    anis; anisotropy constant
      SATMA = 1.7D3
      WIDTH =.25D-3/DSQRT(2D0)
      EXCO = 2D-6/WIDTH**2
      ANIS = 4.7D5

C..    CORPAR;finding the position of the 90° domain wall with a (100) plane
20 CALL CORPAR(H)

C.. appcur: applied current
      APPCUR =U2(4)
      AMAG1=SATMA*APPCUR/WIDTH
      IERR = 0
      A0=.25D-2
      N0=10
      JPAR =0

```

```

ANERG2 =0D0
NA=20
ROT2 = DSQRT(2D0)
ROT2H = ROT2*H
SIDE = 1D0/ROT2
P(1) = .0D0
A = A0/DBLE(NA)
NPTS = 0
DO 15 I = 2,100
S(I) = A*DEXP(DBLE(I-1)/DBLE(N0))
I1 = I -1
P(I) = P(I1) +S(I)
IF (P(I) .LE. H) GOTO 15
JPAR =JPAR +1
IF (JPAR .EQ. 1) NMAX = I-1
15 CONTINUE
PMAX = P(NMAX)
RESCALE = H/PMAX
DO 25 J= 2,NMAX
  P(J) = H-P(J)*RESCALE
  S(J) = S(J)*RESCALE
25 CONTINUE
P(1) =H
DELX =S(2)
DELZ = S(2)
C region 1
DO 35 I=1, NMAX - 1
  NPTS = NPTS+1
  X(NPTS) = (P(I) - S(I+1)/3D0)
  Y(NPTS) = (P(I) -2D0*S(I+1)/3D0)
  AREA(NPTS) = S(I+1)*S(I+1)/2D0
C..   calculating the total energy
  CALL DOIT(ENERG,X(NPTS),Y(NPTS),AREA(NPTS))
  ANERG2 =ANERG2 + ENERG
  TYCOM=TYCOM+YCOM
  NPTS = NPTS+1
C..   the postion calculating the energy density for a small triangle
  X(NPTS) = (2D0*H - P(I)+S(I+1)/3D0)
  Y(NPTS) = (P(I) -2D0*S(I+1)/3D0)
  AREA(NPTS) = S(I+1)*S(I+1)/2D0
  CALL DOIT(ENERG,X(NPTS),Y(NPTS),AREA(NPTS))
  ANERG2 =ANERG2 + ENERG
  TYCOM=TYCOM+YCOM
  DO 35 J=1,I -1
    NPTS = NPTS+1
C..   for a retangular
  X(NPTS) = ( P(J)-S(J+1)/2D0)
  Y(NPTS) = (P(I) -S(I+1)/2D0)
  AREA(NPTS) = S(I+1)*S(J+1)
  CALL DOIT(ENERG,X(NPTS),Y(NPTS),AREA(NPTS))
  ANERG2 =ANERG2 + ENERG
  TYCOM=TYCOM+YCOM
  NPTS = NPTS +1
C..   for a small trangle
  X(NPTS) = (2D0*H - P(J)+S(J+1)/2D0)
  Y(NPTS) = (P(I) -S(I+1)/2D0)
  AREA(NPTS) = S(I+1)*S(J+1)
  CALL DOIT(ENERG,X(NPTS),Y(NPTS),AREA(NPTS))

```

```

    ANERG2 =ANERG2 + ENERG
    TYCOM=TYCOM+YCOM
35 CONTINUE
C region 2
  DO 45 I=1, NMAX -1
    NPTS = NPTS+1
    X(NPTS) = (2D0*H - P(I) +2D0*S(I+1)/3D0)
    Y(NPTS) = P(I)
    AREA(NPTS) = S(I+1)*S(I+1)
    CALL DOIT(ENERG,X(NPTS),Y(NPTS),AREA(NPTS))
    ANERG2 =ANERG2 + ENERG
    TYCOM=TYCOM+YCOM
45 CONTINUE
C region 3
  DO 55 I = 1,NMAX -1
    CENI = (P(I) +P(I+1))
    DO 55 J= I+1,NMAX -1
      CENJ = (P(J)+P(J+1))/2D0
      NPTS = NPTS +1
      X(NPTS) = (2D0*H -CENJ)
      Y(NPTS) = CENI - CENJ
      AREA (NPTS) = S(I+1)*S(J+1)*2D0
      CALL DOIT(ENERG,X(NPTS),Y(NPTS),AREA(NPTS))
      ANERG2 =ANERG2 + ENERG
      TYCOM=TYCOM+YCOM
55 CONTINUE
C region 4
  PMID = (P(NMAX)+P(NMAX-1))/2D0
  PX = 2D0*H - PMID
  DELI = P(NMAX -1)/2D0
  DELSTEP =(SIDE -2D0*H)/DBLE(N0)
  DELSTEP2 = DELSTEP*DELSTEP
  DO 75 I = 1, NMAX -1
    PY = P(I) +P(I+1) -PMID
    DO 75 N = 1,N0
      DELN = DELI +DELSTEP *(DBLE(N) -.5D0)
      NPTS=NPTS +1
      X(NPTS) =(PX+DELN)
      Y(NPTS) =PY+DELN
      AREA(NPTS) = S(I+1)*DELSTEP*2D0
      CALL DOIT(ENERG,X(NPTS),Y(NPTS),AREA(NPTS))
      ANERG2 =ANERG2 + ENERG
      TYCOM=TYCOM+YCOM
75 CONTINUE
C region 5
  DO 65 N=1,N0
    PX = 2D0*H + DELSTEP*(DBLE(N)-.5D0)
    DO 65 K = 2,N
      PY = DELSTEP*DBLE(K-1)
      NPTS =NPTS+1
      X(NPTS) =PX
      Y(NPTS) = PY
      AREA(NPTS) = DELSTEP2
      CALL DOIT(ENERG,X(NPTS),Y(NPTS),AREA(NPTS))
      ANERG2 =ANERG2 + ENERG
      TYCOM=TYCOM+YCOM
65 CONTINUE
C region 6

```



```

DO 85 N=1,N0
PX = 2D0*H + DELSTEP*(DBLE(N)-1D0/3D0)
PY = DELSTEP/3D0
NPTS = NPTS + 1
X(NPTS)= PX
Y(NPTS) = PY
AREA(NPTS)= DELSTEP2/2D0
CALL DOIT(ENERG,X(NPTS),Y(NPTS),AREA(NPTS))
ANERG2 =ANERG2 + ENERG
TYCOM=TYCOM+YCOM
85 CONTINUE
C..    FF is the total energy density for a cross section. The last two terms are
C..    demagnetizing and external energies
FF=( ANERG2+(TYCOM/5D1*SATMA)**2*0.8D1*(DLOG
/ (5D1)-1.099D0)-TYCOM*U2(5)*SATMA)*WIDTH**2
83 CALL FLUSH(6)
IF (IERR .NE. 0) FF = ENY * 1.0D1
IF (LFCN) GO TO 60
RETURN
60 DO 70 I = 1, NPARM
WRITE (LUNW1,80) (NAM(J,I),J=1,8), FX(I)
WRITE (LUNW2,80) (NAM(J,I),J=1,8), FX(I)
70 CONTINUE
80 FORMAT (2X, 8A1, 3X, F9.4)
CALL FLUSH(8)
LFCN = .FALSE.
RETURN
END
SUBROUTINE DOIT(ENERG,XXO,ZZO,AREA)
C The subroutine 'DOIT' is for calculating the magnetization. The exchange and
C the anisotropy energies and the one from the applied current.
IMPLICIT REAL*8(A - H,O - Z)
COMMON /MN7EXT/ U2(30)
REAL*8 LPZ, LMX, LPZ2, LMX2, MX7, MZ7, MY7, MX8, MZ8, MY8, MX6,
/ MZ6, MY6, MX11, MZ11, MY11, MX3, MZ3, MY3,MZ17,MX17,MY17
DIMENSION XA(20), ZA(20), FZ1(13),FX1(13)
DELKA= 1D0
DIV = 1D1
DELX10 = DELX / DIV
DELX2 = DELX10 * 2D0
DELZ10 = DELZ/ DIV
DELZ2 = DELZ10*2D0
XDS = XXO
C calculate magnetization for each grid point.
Z = ZZO
DO 10 K = 1, 3
M = K + 1
XA(M) = XDS+ DELX10*DBLE(K - 2)
ZA(M) = Z - DELZ10
C..    calculating Mx and My for 11 points for
C..    the differential
C FX1(M) =Mx(m),FZ1 =Mz
CALL POTENT( FZ1(M),XA(M), ZA(M))
CALL POTENT( FX1(M) -ZA(M),XA(M))
10 CONTINUE
DO 20 K = 1, 5
M = K + 4
XA(M) = XDS+ DELX10 * DBLE(K - 3)

```

```

ZA(M) = Z
CALL POTENT( FZ1(M), XA(M), ZA(M))
CALL POTENT( FX1(M) -ZA(M),XA(M))
20 CONTINUE
DO 30 K = 1, 3
M = K + 9
XA(M) = XDS+ DELX10 * DBLE(K - 2)
ZA(M) = Z + DELZ10
CALL POTENT( FZ1(M), XA(M), ZA(M))
CALL POTENT( FX1(M) -ZA(M),XA(M))
30 CONTINUE
MZ7 = FZ1(7)
MX7 = -FX1(7)
COM7 = MX7 ** 2 + MZ7 ** 2
IF (COM7 .GT. 1.0D0) COM7 = 1D0
MY7 = DSQRT(1.0D0-COM7)
MZ8 = FZ1(8)
MX8 = -FX1(8)
COM8 = MZ8 ** 2 + MX8 ** 2
IF (COM8 .GT. 1.0D0) COM8 = 1D0
MY8 = DSQRT(1.0D0-COM8)
MZ6 = FZ1(6)
MX6 = -FX1(6)
COM6 = MZ6 ** 2 + MX6 ** 2
IF (COM6 .GT. 1.0D0) COM6 = 1.0D0
MY6 = DSQRT(1.0D0-COM6)
DMYX = (MY8 -MY6)/DELX2
MZ11 = FZ1(11)
MX11 = -FX1(11)
COM11 = MX11 ** 2 + MZ11 ** 2
IF (COM11 .GT. 1.0D0) COM11 = 1D0
MY11 = DSQRT(1.0D0-COM11)
MZ3 = FZ1(3)
MX3 = -FX1(3)
COM3 = MX3 ** 2 + MZ3 ** 2
IF (COM3 .GT. 1.0D0) COM3 = 1D0
MY3 = DSQRT(1.0D0-COM3)
C.. dmyz;  $\partial My/\partial z$  dx2;  $\partial Mz/\partial x$  dx2;  $-\partial Mx/\partial z$ 
DMYZ = (MY11 - MY3) / DELZ2
DXX2 = (FZ1(8) - FZ1(6)) / DELX2
DXZ2 = (FX1(11) - FX1(3)) / DELZ2
E1 = DMYZ ** 2
E2 = ( DXX2 +DXZ2) ** 2
E3 = DMYX ** 2
C.. max1,amz; components of the field from current
CALL APCUR(AMX1,AMZ,XDS,Z)
ENERAP=MX7*AMX1+MZ7*AMZ
C ENERG is the total energy. ENERG1 is the exchange energy. ENERG2 is the energy
C from applied current. ENERG3 is the anisotropy energy.
ENERG2=-AMAG1*ENERAP/1D1
ENERG3= ANIS*((MX7*MZ7)**2+(MX7*MY7)**2+(MY7*MZ7)**2)
ENERG1 = EXCO*(E1 + E2 + E3)*.5D0
ENERG = (ENERG1+ENERG3+ENERG2)*AREA*8D0
YCOM = MY7*AREA*8D0
80 RETURN
END
SUBROUTINE CORPAR(HCOR)
C The subroutine to find the position of a 90° wall with <100> plane.

```

```

C Calculation is done along the z-axis
IMPLICIT REAL*8 (A - H,O - Z)
COMMON /MN7EXT/ U2(30)
DELKA=1D0/DSQRT(2D0)
MPTS = 1000
AMPT = DBLE(MPTS)
BMAX= .0D0
DO 20 I2=1,MPTS
  ADEL =DELKA/AMPT/1D2
  NGRID4 =I2-1
  XXO1 =DELKA * DBLE(NGRID4)/AMPT
  Z5 = 0D0
  X5 = XXO1+ADEL/2D0
  CALL POTENT (Q2,X5,Z5)
  CALL POTENT (Q4,-Z5,X5)
  QX1=Q2
  QZ1=-Q4
C GH1 =My
  GH1=DSQRT(QX1**2 +QZ1**2)
  IF (BMAX .NE. 0D0) GOTO 20
  IF (GH1 .GT. .69D0 .AND. GH1 .LT. .72D0) BMAX=X5
20 CONTINUE
  HCOR =BMAX
  RETURN
  END
SUBROUTINE POTENT(FX0,X01,Z01)
C.. The magnetization from the magnetization
C.. from Eq. 5.2.1
C.. U2(1) =a,U2(2)=h,U2(3)=k,U2(4)=external field.
IMPLICIT REAL*8(A-H,O-Z)
COMMON /MN7EXT/ U2(30)
KPAR= INT(U2(3))
X0=(X01 -Z01)/DSQRT(2D0)
Z0=(X01+Z01)/DSQRT(2D0)
XOP = -2D0*X0/U2(1)
ZOP = -2D0*Z0/U2(1)
EX1=DEXP(XOP)
EZ1=DEXP(ZOP)
IF (DABS(XOP) .LE. 1D-2) EX1 = 1D0+XOP+XOP**2/2D0
/ +XOP**3/6D0 +XOP**4/2.4D1+XOP**5/1.2D2
IF (DABS(ZOP) .LE. 1D-2) EZ1 = 1D0+ZOP+ZOP**2/2D0
/ +ZOP**3/6D0 +ZOP**4/2.4D1+ZOP**5/1.2D2
EXZ1=EX1+EZ1+EX1*EZ1
EXZ2 =DLOG((1D0+EXZ1)/4D0)
IF (DABS(EXZ1) .LE. 1D-4) EXZ2 = EXZ1 -EXZ1**2/2D0
/ +EXZ1**3/3D0 - EXZ1**4/4D0-DLOG(4D0)
C FXz is 2h/(alog(cosh(x/a))*cosh(z/a))
FXZ = 1D0/(X0 + Z0 +U2(1) *EXZ2)*U2(2)*DSQRT(2D0)
UXZ = -2D0*FXZ**KPAR
UXZ1 = DEXP(UXZ)
UXZ2 = 1D0 -UXZ1
IF (DABS(UXZ2) .LE. 1D-5) UXZ2 = -UXZ -UXZ**2/2D0-UXZ**3/6D0
C Fx0 is the x-component of the magnetization(final form).
EUXZ = UXZ2/(1D0+UXZ1)
FX0 =FXZ**(KPAR +1)* EUXZ**(1D0-1D0/DBLE(KPAR))
/ *2D0**1.5D0/UXZ2**2*UXZ1*(1D0 - EX1)/(1D0 + EX1)
RETURN
END

```

```

SUBROUTINE APCUR(AMAGX,AMAGY,XO,ZO)
C the magnetic field from an applied current.
C Eq. 2.5.4 is calculated in this subroutine
IMPLICIT REAL*8(A-H,O-Z)
X1=XO+1D0
X2=XO-1D0
XQ1=X1**2
XQ2=X2**2
Z1=ZO+1D0
Z2=ZO-1D0
ZQ1=Z1**2
ZQ2=Z2**2
PI=3.14159265D0
AMAG=-1D0/8D0/PI*(.5D0*X1*DLOG((ZQ1+XQ1)/(ZQ2+XQ1))-.5D0*
/ X2*DLOG((ZQ1+XQ2)/(ZQ2+XQ2))+Z1*(DATAN(X1/Z1)-
/ DATAN(X2/Z1))-Z2*(DATAN(X1/Z2)-DATAN(X2/Z2)))
AMAG1=1D0/8D0/PI*(.5D0*Z1*DLOG((XQ1+ZQ1)/(XQ2+ZQ1))-.5D0*
/ Z2*DLOG((XQ1+ZQ2)/(XQ2+ZQ2))+X1*(DATAN(Z1/X1)-
/ DATAN(Z2/X1))-X2*(DATAN(Z1/X2)-DATAN(Z2/X2)))
AMAGX=(AMAG -AMAG1)/DSQRT(2D0)
AMAGY=(AMAG + AMAG1)/DSQRT(2D0)
RETURN
END

```

## References

1. R.V. Coleman and G.G. Scott, Phys. Rev. **107**, 1276(1957).
2. R.V. Coleman and G.G. Scott, J. Appl. Phys. **29**, 326(1958).
3. D.W. Shumate, Jr., R.V. Coleman, and R.C. Fivaz, Phys. Rev. B **1**, 394(1970).
4. R. Berthe, A. Birkner, and U. Hartmann, phys. stat. sol.(a) **103**, 557(1987).
5. G.G. Hembree, J. Unguris, R.J. Ceotta, and D.T. Pierce, Scanning Microsc. Suppl. **1**, 241(1987).
6. E. Tatsumoto, Phys. Rev. **109**, 658(1958).
7. J. Smit, Physica **16**, 612(1951).
8. B.A. Lilley, Phil. Mag. **41**, 792(1950).
9. B. Heinrich and A.S. Arrott, Can. J. Phys. **50**, 710(1971).
10. W.F. Brown, Jr., *Magnetostatic Principles in Ferromagnetism*, Interscience, New York, 1962.
11. W.F. Brown, Jr., *Micromagnetics*, Interscience, New York, 1963.
12. W.F. Brown, Jr., Phy. Rev. **58**, 736(1940).
13. A. Aharoni, Rev. Mod. Phys. **34**, 227(1962).
14. A. Aharoni, phys. stat. sol. **16**, 2(1966).
15. W.F. Brown, Jr., *Recent Advances in Engineering Science*, vol. 5, Gordon and Breach Science Pub. Inc., London, 1970.
16. A. Aharoni, CRC Critical Reviews in Sol. Stat. Sci. **2**, 121(1971).
17. M.E. Shabes, J. Magn. Magn. Mat. **95**, 249(1991).
18. A.E. Labonte, J. Appl. Phys. **40**, 2450(1969).

19. A.S. Arrott, B. Heinrich, and A. Aharoni, IEEE Trans. Magn. **15**, 1228(1979).
20. A.S. Arrott, B. Heinrich, and D.S. Bloomberg, AIP Conf. Proc. **5**, 897(1971).
21. D.S. Bloomberg and A.S. Arrott, Can. J. Phys. **53**, 1454(1974).
22. A.S. Arrott and B. Heinrich, J. Appl. Phys. **49**, 2028(1978).
23. S. Chikazumi, *Physics of Magnetism*, John Wiley and Sons, New York, 1964, p. 421.
24. S. Shtrikman and D. Treves, *Magnetism*, vol. 3, ed. G. Rado and H. Suhl, Academic Press, New York, 1963.
25. H.A.M. van der Berg, IBM J. Res. Develop. **33**, 540(1989).
26. H. Kronmüller, *Science and Technology of Nanostructured Magnetic Materials*, ed. G.C. Hadjpanayis and G.A. Prinz, Plenum Press, New York, 1991, pp. 657-673.
27. J.L. Blue and M.R. Scheinfein, J. Appl. Phys. **68**, 6504(1990).
28. C. Kittel, Rev. Mod. Phys. **21**, 541(1949).
29. R.W. DeBlois and C.D. Graham, Jr., J. Appl. Phys. **29**, 528(1958).
- 30 R. Schäfer, A. Hubert, and G. Herzer, J. Appl. Phys. **69**, 5325(1991).
31. A. Hubert, J. de Phys. **49**, 1859(1988).
32. M.R. Scheinfein, J. Unguris, R.J. Celotta, and D.C. Pierce, Phys. Rev. Lett. **63**, 668(1989).
33. H.J. Williams, W. Shockley, and C. Kittel, Phys. Rev. **80**, 1089(1950).
34. P.D. Agarwal and L. Rabiun, J. Appl. Phys. **31**, 246S(1960).
35. U. Hartmann, phys. stat. sol.(a) **110**, 247(1988).
36. D.S. Bloomberg, Ph.D. Thesis, Simon Fraser Univ.(1973).

37. S.D. Hanham, B. Heinrich, and A.S. Arrott, J. Appl. Phys. **50**, 2146(1979).
38. A.S. Arrott, B. Heinrich, and T.L. Templeton, IEEE Trans. Magn. **25**, 4364(1989).
39. A.S. Arrott and B. Heinrich, J. Appl. Phys. **49**, 2028(1978).
40. Chikazumi, *ibid.*, pp. 321-326.
41. A. Isin and R.V. Coleman, Phys. Rev. **137**, A1609(1965).
42. A. Isin and R.V. Coleman, Phys. Rev. **142**, 142(1966).
43. Chikazumi, *ibid.*, pp. 421-422.
44. Küpfmüller, *Einführung in die theoretische Elektrotechnik*, vol. 8. Aufl., Springer-Verlag, 1965, p. 242.
45. S.S. Brenner, *The art and science of growing crystals*, John Wiley and Sones, New York, 1963, p. 30.
46. S.D. Hanham, Ph.D. Thesis, Simon Fraser Univ.(1980).
47. R.C. Weast, *CRC Handbook of Chemistry and Physics*, 64th ed. CRC Press, Boca Raton, 1984, p. E-78.
48. A. Hubert, phys. stat. sol. **32**, 519(1969).
49. A.S. Arrott, B. Heinrich, and D.S. Bloomberg, IEEE Trans. Magn. vol. **MAG-10**, 950(1974).
50. A. Aharoni and J.P. Jakubovics, J. Appl. Phys. **69**, 4587(1991).
51. J.P. Jakubovics, Phil. Mag. B **38**, 401(1978).